Charles University in Prague

Faculty of Mathematics and Physics

DOCTORAL THESIS

Ilya Tkach

Superconductivity and electronic properties of γ-U alloys and their hydrides.

Department of Condensed Matter Physics

Supervisor of the doctoral thesis: Doc. RNDr. Ladislav Havela, CSc.

Study programme: Physics
Specialization: Physics of Condensed Matter and Materials

Prague 2015

Acknowledgements

During my post-graduate study at the Charles University I have been working with many people, some of them highly contributed to the following work. First of all, I would like to express my deepest gratitude to my supervisor Doc. RNDr. Ladislav Havela, CSc. who guide me for many years during Ph.D. course. Thanks to his huge patience, excellent sense of humour, great scientific experience and helpful explanations and discussions. All that allowed me to grow my scientific skills and achieve interesting results.

I also highly appreciate the contribution made by Dr. Hab. Nhu-Tarnawska Hoa Kim-Ngan, Ph.D. from Institute of Physics of Pedagogical University in Krakow. Thanks for her support, discussions and help in planning of this work, for pushing me forward and assistance in experiments.

My special thanks to colleagues RNDr. Silvie Mašková, Ph.D. and Mgr. Mykhaylo Paukov for their invaluable help and assistance in experiments. I would like to express my gratitude to our colleagues from the Department of Condensed Matter, Mgr. Zdeněk Matěj, Ph.D. for XRD refinements and analysis, to RNDr. Jiří Prchal, Ph.D. for his support in resistivity measurements, to RNDr. Jiří Pospíšil, Ph.D. for fast and helpful problem-solving in the technical lab.

My thanks to the staff of the Joint Laboratory for Magnetic Studies, Ing. Josef Šebek, CSc., Ing. Eva Šantavá, CSc., Ing. Martin Žáček and RNDr. Jan Prokleška, Ph.D. for help and assistance during measurements on laboratory equipment.

I also highly appreciate the contribution of our colleagues from the Department of Physics of Materials Mgr. Daria Drozdenko, RNDr. Peter Minárik, Ph.D., Doc. RNDr. Miroslav Cieslar, CSc. for their contribution to microstructure analysis of our samples by SEM and TEM.

I wish to thank my friends and family for their support, love and belief in me, which gives me forces through the years of post-graduate study. Special thanks to the great people Steve Jobs and Elon Musk, who gives me inspiration in physics and technologies.

I declare that I carried out this doctoral thesis independently, and only with the cited sources, literature and other professional sources.

I understand that my work relates to the rights and obligations under the Act No. 121/2000 Coll., the Copyright Act, as amended, in particular the fact that the Charles University in Prague has the right to conclude a license agreement on the use of this work as a school work pursuant to Section 60 paragraph 1 of the Copyright Act.

In…..... date..... signature

Název práce: Supravodivost a magnetické vlastnosti slitin γ-U a jejich hydridů.
Autor: Ilya Tkach

Katedra / Ústav: Katedra fyziky kondenzovaných látek

Vedoucí doktorské práce: Doc. RNDr. Ladislav Havela, CSc.

Abstrakt: Byly prostudovány nízkoteplotní elektronové vlastnosti splatů U-Mo a U-Zr, ve kterých byla zachována struktura *bcc* (γ-U), stabilní za vysokých teplot. Magnetická studia pro U-Mo slitin prokázala Pauliho paramagnetické chování. U-Mo a U-Zr splaty přecházejí do supravodivého stavu pod teplotou T_c, která může dosáhnout až 2.1 K a vykazují kriticiká pole až 5-6 T. Supravodivost u γ-U může být považována za objemový efekt a je posána teorií BCS, zatímco supravodivost u α-U skutečný objemový efekt není.
Bcc slitiny U-Mo and U-Zr alloys absorbují vodík jen za výšených tlaků ($p \geq 4.5$ bar) a vytvářejí hydridy se stechiometrií analogickou k UH_3. Tyto hydridy s Mo vykazují amorfní strkturu, založenou na struktuře typy β-UH_3, zatímco hydridy s Zr mají krystalickou struktury typu α-UH_3 type. Hydridy $(UH_3)_{1-x}Mo_x$ jsou feromagnetické s hodnotami Curievy teploty T_C a magnetických momentů zvýšenými (přes 200 K a do okolí 1.1 μ_B/U) ve srovnání s čitým β-UH_3 (165 - 175 K; 0.9 μ_B/U). Jsou to patrně první amorfní feromagnetika na bázi uranu s tak vysokými T_C. Hodnoty koercitivního pole u $(UH_3)_{1-x}Mo_x$ a $(UH_3)_{1-x}Zr_x$ dosahují za nízkých teplot až 6 T. Vlastnosti těchto hydridů (typy α-UH_3, β-UH_3, amorfní) jsou pozoruhodně skoro identické navdory různé krystalové struktuře a rozdílným minimálním vzdálenostem mezi atomy uranu.

Klíčová slova: Uran; supravodivost; feromagntismus; hydridy

Title: Superconductivity and electronic properties of γ-U alloys and their hydrides.

Author: Ilya Tkach

Department / Institute: Department of Condensed Matter Physics, Faculty of Mathematics and Physics, Charles University

Supervisor of the doctoral thesis: Doc. RNDr. Ladislav Havela, CSc., Department of Condensed Matter Physics, Faculty of Mathematics and Physics, Charles University, Prague, The Czech Republic

Abstract: Low-temperature electronic properties for U-Mo and U-Zr splats stabilized in γ-U were investigated. Magnetic measurements revealed Pauli paramagnetic behavior with temperature independent susceptibility for U-Mo alloys. U-Mo and U-Zr splats become superconducting at low temperatures with T_c up to 2.1 K and critical field 5-6 T. The superconductivity of γ-U can be considered as a bulk effect and can be described by the BCS theory, while α-U superconductivity is not a real bulk effect.

U-Mo and U-Zr alloys absorb hydrogen at high pressures ($p \geq 4.5$ bar) and form hydrides with stoichiometry analogous to UH_3. The hydrides with Mo have an amorphous structure based on β-UH_3 phase, while hydrides with Zr have a crystalline structure of the α-UH_3 type. $(UH_3)_{1-x}Mo_x$ hydrides are ferromagnetic with enhanced T_C up to 202 K and magnetic moments 1.1 μ_B/U in comparison with pure β-UH_3 (175 K; 0.87 μ_B/U). This is probably the first U-based ferromagnet with such a high T_C. The coercive field of $(UH_3)_{1-x}Mo_x$ and $(UH_3)_{1-x}Zr_x$ hydrides reaches values up to 4-6 T at low temperatures. Abrupt jumps are observed during the demagnetization process. Despite different crystal structure and inter-U spacing, the electronic properties of α-UH_3 phase are very similar to β-UH_3.

Keywords: Uranium; superconductivity; ferromagnetism; hydrides

Contents

Introduction

Uranium can appear in 3 possible allotropic phases. Variation of lattice parameters and inter-uranium distances in different crystal structures can play an important role in electronic properties, in analogy with various U-based compounds.

Electronic properties are well known only for α-U, which is stable at room temperature (below 942 K) and crystallizes in an orthorhombic structure. α-U uranium exhibit anomalies at low temperatures (23 K, 37 K, 43 K) observed in magnetic susceptibility, electrical resistivity and specific heat data, which can be attributed to charge density waves. α-U was reported to become superconducting below T_c = 0.78 K, although recently it was suggested that the developed charge-density-wave state prohibits the superconductivity [1].

β-phase having a tetragonal structure with large unit cell is stable in the range 942-1049 K. As γ-U phase with a cubic *bcc* structure is stable at even higher temperatures (1049-1408 K), the low temperature properties remain unknown for γ-U. On the other hand, *bcc* U can be retained to low temperatures in the form of highly alloyed (Mo, Zr) U for metals fuels, at which the *bcc* structure provides better mechanical properties and higher resistance to irradiation effects [2]. As their studies were for half century, in the field of metallurgists, nobody used this route to learn anything about *bcc* uranium itself and its fundamental properties. We decided to use the doping by Mo or Zr in conjunction with the splat-cooling technique, which could help to stabilize γ-U phase to room temperature with minimal amount of dopants in the alloys. In this work we present results of investigations of γ-U phase alloys, electronic properties, as well as superconductivity (with T_c up to 2.1 K), in comparison with the α-U phase.

In addition, we have studied interaction of these alloys with hydrogen gas, which leads to the formation of hydrides. Hydrogenation can be considered as a "negative" pressure effect, which expands the lattice and therefore also change the inter-uranium distances. As a result, observed hydrides have a ferromagnetic ground state with relatively high (for 5*f* magnetism) Curie temperature (exceeding 200 K) and extreme coercive forces. Surprisingly for us, the obtained hydrides form diverse structures, so we were able to survey materials analogous to UH_3 as affected by

structure and alloying modifications. This brought more light onto the notorious UH_3, the eldest known purely 5*f* ferromagnet. It exists in two different cubic modifications. Besides the common β-UH_3 there is a metastable form α-UH_3, which could be never prepared without β-UH_3. That is why its magnetic and other electronic properties were remaining unclear.

The short theoretical introduction will be given at the beginning. Chapter 1 is devoted to theoretical aspects of electronic structure for localized and delocalized electron systems. Uranium compounds are considered vaguely as intermediate between localization and delocalization, which means they can significantly vary electronic properties due to changes in the degree of localization. We introduce main features typical for uranium compounds, like high magnetocrystalline anisotropy and the significance of the U-U spacing, expressed by the Hill limit, separating superconducting and magnetically ordered ground states.

As part of our samples is superconducting, we describe in Chapter 2 the basics of superconductivity phenomena and a simple BCS theory which can be applied for conventional superconductors. Some important cases of uranium-based superconductors are also considered (Subchapter 2.2).

In Chapters 3 and 4 we review literature data on crystal structure, electronic and magnetic properties of γ-U phase and uranium hydrides (α-UH_3, β-UH_3). Further in Chapter 5 we discuss sample preparation methods, measurement equipment and experimental techniques which were used in this work.

Chapter 6 is fully devoted to results of our investigation and their discussion. It consists of two main parts. In the first part U-Mo and U-Zr splat samples properties are discussed. In the second part, the hydrides, which were prepared from U-Mo and U-Zr alloys, are discussed. The conclusions of this work and future outlook are presented at the end.

1. Electronic and magnetic properties of actinides

Electronic properties of actinides are primarily determined by the open 5*f* electronic shell. The outer partly occupied shells are of the 6*d* and 7*s* type. The situation is to some extent analogous to rare earth elements, where the unfilled 4*f* shell is deeply embedded within the core of atoms and shielded by 6*s* and 5*d* outer states. It preserves the 4*f* electron localization even in solid state, and as a consequence magnetic moments of ions cannot interact directly between each other. Exchange interaction in this case is in metals mediated by the RKKY mechanism, which is indirect interaction via conduction electrons surrounding atoms in the metal.

The main difference between the 5*f* and 4*f* elements is a larger spatial extent of the 5*f* wave functions, leading to an overlap between neighbors and formation of a narrow 5*f* band in light actinide elements. In particular for Uranium, the 5*f* electrons can be mostly considered as itinerant, i.e. similar to e.g. *d* electrons in transition metals. An important difference between 5*f* elements and 3*d* elements is a narrower band and much stronger spin-orbit interaction in the 5*f*-electron systems.

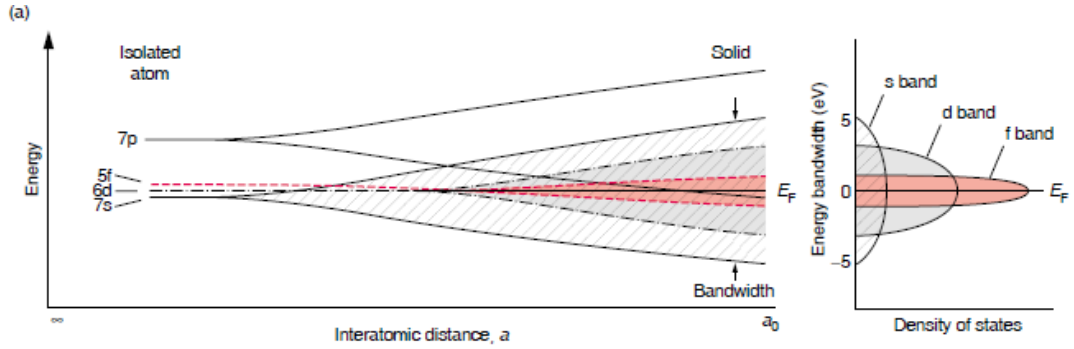

Figure 1.1. Multiband formation in light actinides [3]. The 5*f* band becomes narrower and the density of states increases with increase of interatomic distance.

As delocalization is depending on the overlap between 5*f* wave functions, it is primarily related to the shortest interatomic distances between actinide atoms. The overlap decreases with increasing interatomic distances. The 5*f* band becomes narrower and the density of states increases. As the band is crossed by the Fermi level, also the density of states (DOS) at the Fermi level, $N(E_F)$, is likely to increase. It affects e.g. the Sommerfeld coefficient of low temperature electronic specific heat

and transport properties. Finally, at some spacing between actinide atoms, the 5*f* electronic states undergo the Mott transition, i.e. they localize.

Such Mott transition is observed in actinides row. As seen e.g. in the cohesion properties, light actinide elements (Th, Pa, U, Np, Pu) have the 5*f* states participating in bonding, i.e. delocalized, whereas heavy actinides (Ac, Am, Cm, Bk, Cf.) with larger but weakly varying metallic radius have the localized 5*f* states analogous to the 4*f* states in lanthanides. The displacement of the 5*f* states out from the Fermi level affects $N(E_F)$ and various related properties.

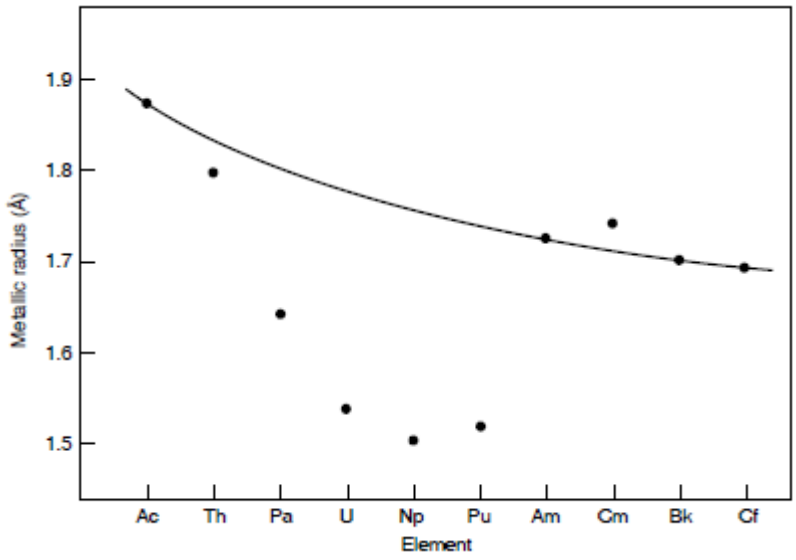

Figure 1.2. The Metallic Radii of the Actinide Elements in the Ground State [3]. The metallic radius is half the average distance between the atoms in the solid. The line follows the smoothly varying metallic radii of the simple trivalent actinide metals, whose *f* electrons are localized and therefore nonbonding. The metallic radii of the light actinides - thorium through plutonium - fall on a parabolic curve below the trivalent line, showing the contribution of the *f* electrons in the bonding, that is, in pulling the atoms closer together.

1.1. Localized electron systems

Rare earth elements (lanthanides) can be considered as example of localized electron systems. The unfilled 4*f* shell is deeply embedded in the core of atom and has a small extent. The 4*f* shell is shielded by outer 6*s* and 5*d* shells. Therefore the 4*f* shell can be in the first approximation considered as atomic shell of free ion. The Hamiltonian of localized electrons in the 4*f* states can be written as (if the spin-orbit interaction is neglected):

$$H_{4f} = \sum_{i=1}^{N} -\frac{\hbar^2}{2m_e}\nabla_i^2 + \sum_{i=1}^{N} -\frac{\tilde{Z}e^2}{r_i} + \sum \frac{e^2}{r_{ij}} \qquad (1.1.1.).$$

This expression includes contributions from the kinetic energy, interaction of 4*f* electrons with other filled shells, and interaction of 4*f* electrons within the 4*f* shell. To simplify calculations of the Schrödinger equation, the Hartree-Fock approximation (one-electron approximation) is often used. In this case the Hamiltonian is rewritten as:

$$H_{4f} = \sum_{i=1}^{N} -\frac{\hbar^2}{2m_e}\nabla_i^2 + \sum_{i=1}^{N} -\frac{\tilde{Z}e^2}{r_i} + \sum_{i\neq j} V_i(r), \qquad (1.1.2.)$$

where the last term is substituted by $V_i(r)$, which is self-consistent Hartree-Fock potential of the 4*f* shell electrons.

1.1.1. Magnetic moment of localized electron system

As an unfilled shell of localized electron system can be considered as a shell of isolated atom, we can use calculations of atomic magnetic moment. The ground state of multi-electron atom is characterized by quantum numbers of total angular momentum *J*, total spin angular momentum *S* and total orbital angular momentum *L*. The Hund's rules can be used to determine how an electron shell is occupied by electrons in the ground state. Each electron has its own orbital angular momentum ***l*** and spin angular momentum ***s***. Total spin *S* and orbital *L* momenta are calculated as a sum of momenta of individual electrons in the shell. If the total energy should be minimized, electrons fill the shell by the Hund's rules in such order:

1. The total spin angular momentum *S* should be maximized.
2. For a given *S*, the total orbital angular momentum *L* is also maximized.
3. For a given *L* and *S*, if shell is half-filled or less, then total angular momentum calculates $J = L - S$. If shell is more than half-filled, then $J = L + S$.

Atomic magnetic moments are characterized by total angular momentum *J* and can be calculated by:

$$\mu = g\mu_B J \tag{1.1.3.}$$

where μ_B is the Bohr magneton and *g* is the Landé factor, which is given by:

$$g = 1 + \frac{J(J+1) + S(S+1) - L(L+1)}{2J(J+1)}. \tag{1.1.4.}$$

1.1.2. RKKY interaction

Due to a negligible 4*f*-4*f* overlap, direct exchange interactions in localized electron systems are very weak. So an indirect interaction can play a significant role in such systems. Magnetic moments of ions with electrons in localized states can be magnetically ordered through the indirect interaction mediated by conduction electrons. Those are polarized by exchange interaction close to an ion. Two 4*f* neighbors share the polarized cloud that creates a long-range correlation between orientations of magnetic moments of ions. This correlation of orientations gives rise to magnetic ordering in localized electron systems. Such indirect interaction through the conduction electrons is called RKKY (after the names of scientists: Ruderman, Kittel, Kasuya, and Yoshida).

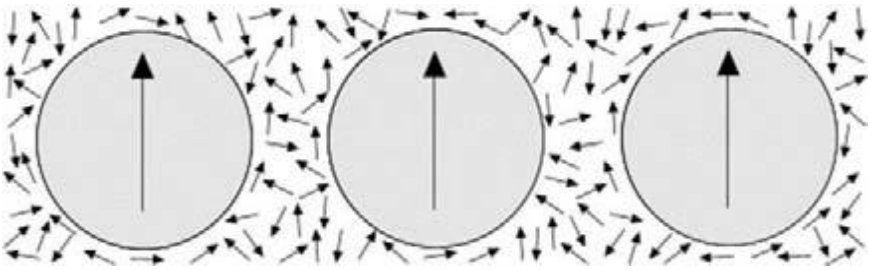

Figure 1.3. Schematic drawing of the RKKY interaction.

The Hamiltonian of the RKKY interaction is given by:

$$\hat{H}_{RKKY} = -\frac{1}{2}\sum_{i,j} J(R_{ij})\hat{J}_i\hat{J}_j \quad , \tag{1.1.5.}$$

where J is exchange parameter responsible for interactions between pair of ions and their magnetic moments. This modulated exchange interaction parameter can be expressed in such approximation:

$$J \propto \frac{\cos(2k_F r)}{r^3}, \tag{1.1.6.}$$

where k_F is a wave vector of Fermi surface, r is a distance from atom.

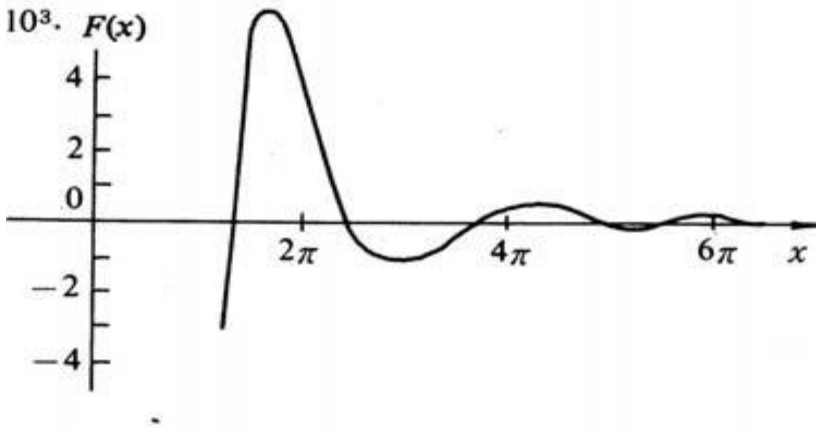

Figure 1.4. Oscillating character of the RKKY interaction which depends on the distance from the atom.

As seen from Fig.1.4, such interaction has oscillatory sign. The envelope follows $1/r^3$, that means it is a long-range interaction. As a result, it gives a large diversity of magnetic structures.

1.2. Itinerant electron systems

In itinerant electron systems electrons responsible for magnetic moments are no longer localized on certain atoms as in localized systems. Energy levels are broadened and form narrow bands. 3*d* elements can be used as a good example of itinerant electron systems, where the 3*d* electrons are responsible for magnetism.

1.2.1. Hubbard model

The Hubbard model is used for description of magnetism in itinerant electron systems. The Hubbard Hamiltonian is including contributions from the electron hopping between sites and the in-site Coulomb interaction. The Pauli principle is also included in the Hubbard model consideration.

The Hubbard Hamiltonian is given by:

$$H = \sum_{ij\sigma} t_{ij} c_{i\sigma}^{+} c_{j\sigma} + U \sum_{i} n_{i\uparrow} n_{i\downarrow} \quad , \qquad (1.2.1.)$$

where t_{ij} is coefficient of electron hopping between i and j sites and U is represents on-site Coulomb repulsion due to electron charge. $c_{i\sigma}^{+}$ and $c_{j\sigma}$ are represent creation and annihilation operators for electrons with spin σ and site i. $n_{i\uparrow}$ is the ladder operator which gives occupation number on site i with spin σ orientation up. Hopping between electrons with the same orientation of spins is forbidden by the Pauli Exclusion Principle. So for ferromagnetic ordered systems the Hubbard model needs to be modified by applying the Hartree-Fock approximation.

1.2.2. Stoner theory of ferromagnetism

The Stoner theory is a simplest theory describing ferromagnetic ordering in itinerant band systems. It can be derived from the Hubbard model by applying the Hartree-Fock and mean-field approximation. The Stoner theory is based on the paramagnetic density of states. Electrons are occupying states with lowest possible energies. By the Pauli Exclusion Principle fermions are not allowed to occupy the same quantum state with the same orientation of spin. Electrons occupy energy states by pairs with opposite oriented spins and fill all allowed states up to the Fermi energy. So the total density of states can be split into two bands with electrons spin-up and spin-down orientation, respectively. When an external magnetic field is applied, the density of states for these bands is shifted to higher energies for spins-down (antiparallel to field) and to lower energies for spins-up oriented along field. Finally, electron occupancy of spin-up becomes higher than for spin-down and magnetic moment appears. Similarly spontaneous splitting can be caused by

exchange interactions, preferring parallel orientation of spins. Ferromagnetic ordering observed when the increase in kinetic energy is smaller than a decrease in interaction energy, so the total energy ΔE is smaller than 0:

$$\Delta E = \Delta E_{kin.} + \Delta E_{\text{int.}} = N(E_F)(\delta E)^2(1 - U * N(E_F)), \qquad (1.2.2.)$$

where $N(E_F)$ is density of states at the Fermi level, δE is an arbitrary small energy shift, U is the intra-atomic Coulomb repulsion integral for electrons with opposite spins. Spontaneous splitting of bands with opposite oriented spins appears when $UN(E_F)>1$. This condition is called Stoner criterion, which describes appearance of ferromagnetism in itinerant electron systems.

1.3. Electronic properties of uranium compounds

1.3.1. Hill limit

As mentioned above, properties of actinides can be rather diverse. For the heavy actinides, at least at ambient pressure, one can apply the localized electron approach in analogy to lanthanides. It has been definitely established that at least pure elemental light actinides can be considered as delocalized electron systems, analogous to 3*d* elements. The main difference between the 5*f* delocalized and the 3*d* electron systems is the stronger spin-orbital interaction for 5*f* electrons in comparison with the 3*d* electrons. The 5*f* electrons form a 5*f* band as a consequence of a large spatial extent of the 5*f* wave functions, which can vary in compounds. Besides the direct 5*f*-5*f* overlap, depending on inter-actinide spacing, 5*f* electrons are affected also by the hybridization with valence states of ligand atoms. Affecting the width of the 5*f* band, the degree of localization is very important for electronic and magnetic properties of actinides.

Uranium belongs to light actinide elements. The shortest inter-uranium spacing for uranium compounds is also the most important factor which determines electronic and magnetic properties. $N(E_F)$ tends to increase with increasing U-U spacing, $d_{U\text{-}U}$, and narrowing of the 5*f* band, if the 5*f*-ligand hybridization is not too strong. At some level of $d_{U\text{-}U}$, $N(E_F)$ starts to fulfill the Stoner criterion and magnetic ordering appears. It was found long time ago that ground state of uranium systems

are often superconducting (non-magnetic) if the shortest inter-uranium spacing $d_{U\text{-}U}$ is smaller than some critical value, and ground state is magnetic if $d_{U\text{-}U}$ is larger than critical value [4].

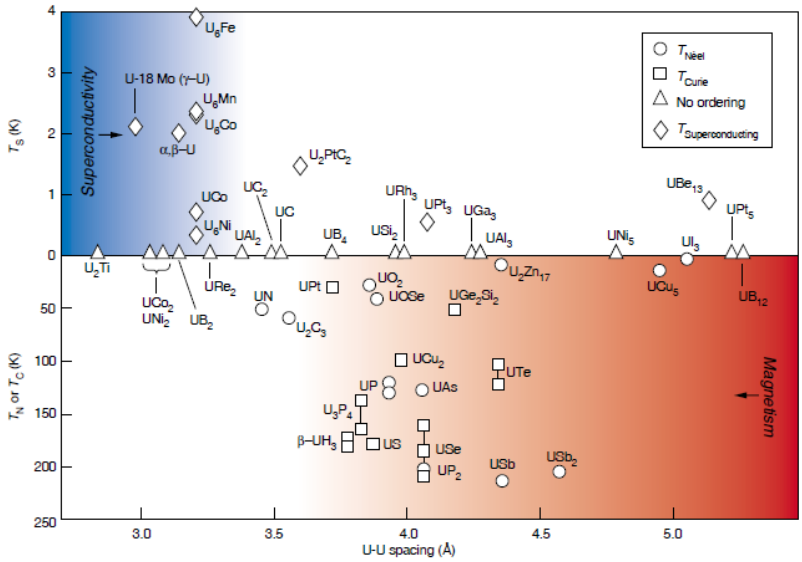

Figure 1.5. The Hill plot shows the superconducting or magnetic transition temperatures vs interatomic spacing separating the *f* electron atoms [3].

This critical parameter is called the Hill limit and considered to be between 3.40 – 3.60 Å. For $d_{U\text{-}U}$ values which are slightly above the Hill limit the ordering is typically ferromagnetic (fig. 1.5). With further increase of $d_{U\text{-}U}$ up to ≈ 4.0 Å antiferromagnetic ordering can be observed. For $d_{U\text{-}U}$ higher than that the only type of ordering observed is antiferromagnetic. This simple rule does not take into account individual details of density of states, which is also affected by the hybridization to ligand states. That is why the Hill limit already has many known exceptions, for example UNi_2 [5], which is magnetic with $d_{U\text{-}U} < 3.10$ Å.

1.3.2. Magnetocrystalline anisotropy

Magnetocrystalline anisotropy of 5*f* intermetallic compounds is much stronger than in 4*f* compounds. The reason for such difference is in different mechanism of magnetocrystalline anisotropy. In lanthanides, where 4*f* electrons are well localized, the single-ion crystalline electric field interaction is responsible for anisotropy. It is based on difference in energy on orientation of non-spherical 4*f* electron density if a

distribution of electrical field (coming both from ligands and electrons of own atom) is present. In the case of light actinide intermetallics, two-ion interaction (5*f*-5*f*) is responsible for anisotropy. The pre-requisites are the bonding character of the 5*f* states (while the bonding can be directional and seeks preferably the direction(s) to the nearest U atoms), and the strong spin-orbit interaction (given by high atomic number *Z*), which couples the spin moments to orbital moments. Orbital moments (which are almost absent in *d*-magnetics - notice that no orbital moments were mentioned in the Stoner model description) are in actinides induced inevitably whenever a spin polarization appears. This is true not only in the case of magnetic ordering, but the anisotropy extends far into the paramagnetic state, if effective moments are present.

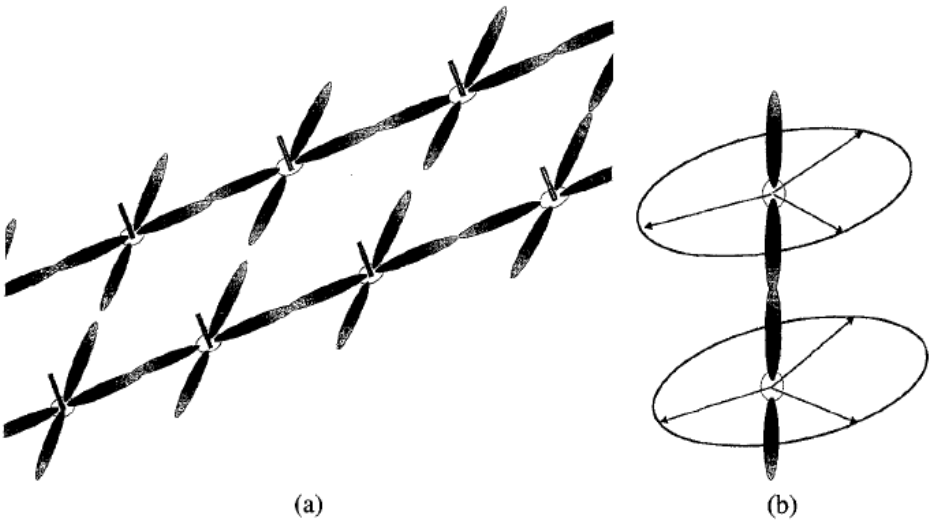

Figure 1.6. Schematic illustration of the planar bonding geometry [6], which forces the magnetic moments represented by the bars perpendicular to the plane (a), which contrasts with the columnar bonding leading essentially to an easy-plane anisotropy type (b).

Such two-ion anisotropy is determined by the geometry of inter-uranium bonds in U compounds. The bonding leads to the preferential occupancy of those states pointing towards the nearest U neighbors, i.e. of states having orbital moments perpendicular to such bond directions. As a result, easy-magnetization directions are oriented also perpendicularly to the shortest U-U spacing (see fig.1.6). If a uranium compound has a uniaxial crystal structure (hexagonal or tetragonal), the easy

magnetization direction is usually parallel or perpendicular to the *c*-axis [6]. If uranium atoms with U-U shortest links form a plane then magnetic moments will be oriented perpendicularly and lead to the easy-axis anisotropy. On the other side, in crystal structures, where U-U shortest links are form linear chains, then easy-plane anisotropy is observed. As the energy difference between different bonding situations are at least on the scale of 0.1 eV (energy of 1 μ_B moment in field of 1 T is 3 orders of magnitude smaller), we can expect such huge magnetocrystalline energies, too. In another words, it means that U moments cannot be simply rotated in field, as they are related to particular structure type.

2. Superconductivity

Superconductivity is a quantum phenomenon observed at low temperatures in some metals and alloys. It can be observed as an abrupt decrease of electrical resistivity to zero or as expulsion of magnetic field from the sample at critical temperature T_c (the Meissner effect). Below the critical temperature sample is in superconducting state. Transition to superconducting state is usually accompanied by the drop of electrical resistivity and magnetic permeability or by an anomaly in specific heat.

Superconductivity is suppressed by applied magnetic field. Critical temperature of superconductivity decreases with increase of applied magnetic field. Finally, at some values superconductivity is totally suppressed and sample is in the normal state. Magnetic field at which superconductivity is lost is called critical field (H_c) and it depends on temperature. Critical field is equal to zero at critical temperature.

Conventional superconductors are divided in two basic types. Type I superconductors have one critical field, above which superconductivity is lost. Type II superconductors have two critical fields (H_{c1}, H_{c2}), between which sample exists in the intermediate state, where part of the sample is in the superconducting state and part is in the normal state.

2.1. BCS theory

The first microscopic theory which describes conventional superconductivity was derived by Bardeen, Cooper, and Schrieffer (hence the name BCS theory). By the BCS theory, at sufficiently low temperatures electrons near the Fermi surface can attract each other and form Cooper pairs (formed of electrons with spins +1/2 and -1/2). These electron pairs behave like a bosonic particle (with integer spin $\boldsymbol{s} = 0$) and therefore no more obey to the Pauli Exclusion Principle. Cooper pairs can occupy the same quantum state and form condensate at low energy level.

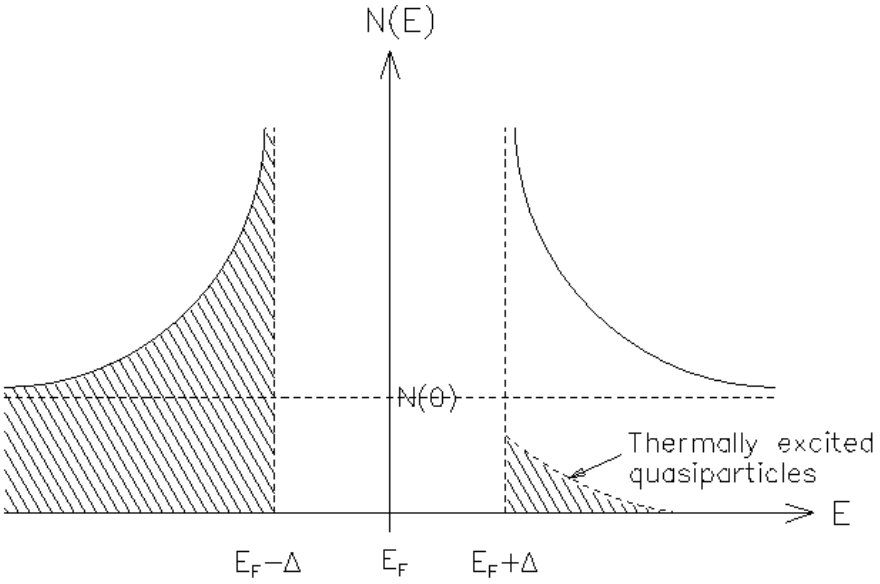

Figure 2.1. The Density of States for BCS superconductor at $0 < T < T_c$. Electrons below $E_F - \Delta$ are in superconducting state, electrons which can overcome the energy gap 2Δ and have energy above $E_F + \Delta$ are in normal state. The energy gap is 2Δ.

Attractive interaction is necessary requirement for the pairing of electrons because they need to overcome the Coulomb repulsion. In different superconductors the origin of attraction force can be different. The conventional superconductivity is based on electron-phonon interaction. As electron is negatively charged particle, when it moves in the crystal lattice it attracts positively charged ions. That causes a small deformation with positively charged regions in the lattice. Other electron with opposite spin and opposite wave vector feels and moves to the region with higher concentration of positive charge. The two electrons finally become correlated. Cooper pairs have a binding energy Δ which determines properties of the superconducting state. The density of states (DOS) of superconductor at temperatures below T_c is schematically shown on fig. 2.1. Opposite to the normal metal state ($T > T_c$) where electrons can consequently occupy states with higher energies, DOS of superconductor has a band gap at the Fermi level which is equal to 2Δ. All electrons below the gap are in paired state. Electrons are needed to overcome this energy gap to increase the energy and break the Cooper pairs, which is necessary for scattering. Some of electrons are thermally excited and located above the energy gap in normal state. At $T = 0$ K all electrons will be in superconducting state.

The BCS theory yields some useful theoretical predictions for low-temperature superconductors with weak attraction between the electrons (also called as weak-coupling regime). BCS theory can predict the value of energy gap which can be calculated from the superconducting transition temperature using following relation: $2\Delta\,(T = 0) = 3.52 \cdot T_c$. The energy gap value can be also obtained from approximation of specific heat temperature dependence by the exponential term $\exp(-\Delta/k_B T)$ after subtraction of the phonon contribution C_{ph}.

The specific heat of superconductor decreases fast at low temperatures due to the energy gap, but it is much higher than the specific heat in normal state at T_c. It can be seen from measurements as a jump of specific heat near $T_{c.}$ The difference of the specific heat for normal and superconducting state can be calculated by formula $\Delta C = C_s - C_n = 1.43 \cdot \gamma_e \cdot T_c$ in the weak coupling regime.

According to theoretical approach in Ref. 7 on the basis of Abrikosov's extension of the Ginzburg-Landau theory and BCS Gorkov equations near Tc it is possible to evaluate the critical field slope $-(dH_{c2}/dT)_{Tc}$:

$$-(dH_{c2}/dT)_{Tc} = [9.55 \cdot 10^{18} \gamma_e^{\,2} T_c (n^{2/3} S/S_F)^{-2} + 5.26 \cdot 10^5 \gamma_e \rho] \cdot R(\lambda)^{-1}, \qquad (2.1.1)$$

where n is the density of conduction electrons in [m^{-3}], γ_e in [$J/m^3 \cdot K^2$] is the Sommerfeld coefficient of electronic specific heat, S/S_F is the ratio of the Fermi surface to the Fermi surface of the free electron gas, ρ is the resistivity in the normal state at low temperature in [Ωm], $R(\lambda)$ is the so called Gorkov function. Simplification of this equation gives prediction that the critical field slope value $-dH_{c2}/dT$ depend on normal-state parameters and on T_c in a way $-dH_{c2}/dT \sim T_c \cdot \gamma_e^2$, where γ_e is the Sommerfeld coefficient of electronic specific heat in the normal state.

The upper critical field of classical superconductors with weak electron-phonon coupling can be derived from the Werthamer-Helfand-Hohenberg (WHH) theory [8], which predicts a universal function H_c vs. T, which is quadratic in T. It provides the $T \rightarrow 0$ limit value $H_{c2}\,(0) \approx 0.7 \cdot T_c \cdot (-dH_{c2}/dT)$.

2.2. Uranium-based superconductors

In this subchapter we will consider only important cases of uranium-based superconductors. Uranium-based superconductors basically can be divided on two groups: conventional BCS superconductors (low U-U spacing) and heavy-fermion unconventional superconductors, which cannot be described by the BCS theory.

U_6X compounds can be considered as example of rather conventional superconductors. Uranium form compounds of the stoichiometry U_6X (X = Fe, Mn, Co, Ni) with a body-centered tetragonal structure (space group I4/mcm) [9]. All U_6X compounds exhibit temperature independent susceptibility and become superconducting at low temperatures (with T_c below 4 K). Correlation between T_c and the average number of valence electrons was observed for the U_6X compounds [10]. Among the U_6X compounds, U_6Fe has the highest T_c = 3.8 K and was studied in detail. U_6Fe has high values of the upper critical field $\mu_0 H_{c2} \approx 10$ T ($T \rightarrow 0$) and critical slope $-d\mu_0 H_{c2}/dT = 3.42$ T/K ($T = T_c$) [11]. The value of electronic specific heat coefficient γ_e = 150 mJ/K^2·mol or 25 mJ/K^2·mol U [12] is much lower comparing to heavy-fermion compounds.

From the compounds with lower U concentration one can mention UCo and URu_3 as conventional superconductors. They become superconducting below T_c = 1.22 and 0.15 K, respectively [13]. The upper critical field slope is rather small 1.5 T/K for UCo and <0.1 T/K for URu_3. The γ_e values 7.8 mJ/K^2·mol and 13.5 mJ/K^2·mol, respectively, are pointing to broad-band systems (i.e. not heavy-fermions) [13].

Pure uranium metal (α-U phase) is also reported superconducting below T_c ranging 0.1-2 K (depending on literature sources), which has been understood as related to variable sample purity. Recent measurements on high-purity U single crystal does not reveal any sign of superconductivity suggesting that the developed charge-density-wave state (CDW) prohibits the superconductivity. The logic behind is that CDW develops fully only in very pure (both chemically and crystallographically) samples. The value of electronic specific coefficient γ_e is in the range 9-12 mJ/K^2·mol [14].

The second group of uranium superconductors is heavy-fermion superconductors, which form an island at very high U-U spacing. The fact that by the

Hill limit rules the compounds should be magnetic, but the magnetism is almost or completely suppressed, indicates that magnetic fluctuation are actually the coupling mechanism instead of electron-phonon coupling. Strong electron-electron correlations lead to a high effective mass of electrons (quasiparticles) participating in superconducting pairing. One of the prominent properties of heavy-fermion superconductors is high values of electronic specific heat at T_c, i.e. high density of electron (quasiparticle) states at the Fermi level. The enormous value of $\Delta C = C_s - C_n$, which should be $1.43 \cdot \gamma_e \cdot T_c$ (in non-BCS superconductors the pre-factor can be somewhat modified) made evident that superconductivity takes place in the system with high γ_e.

In heavy-fermion compounds magnetism and superconductivity can show interplay or even coexist at low temperatures. Such heavy-fermion superconductors cannot be described by the BCS theory, and they display a large variety of unexpected properties.

UBe_{13} was the first uranium heavy-fermion superconducting compound discovered by Bucher et al. in 1975 [15]. UBe_{13} exhibit superconductivity with low T_c = 0.86 K. The effective masses of electrons are more than hundred times higher than for free electrons. The Sommerfeld coefficient is extremely large and equal γ_e = 1.1 J/mol·K^2. Even more unusual are values of $H_{c2} \approx 10$ T ($T \rightarrow 0$) and record-high initial slope of the upper critical field $-d\mu_0 H_{c2}/dT = 42$ T/K ($T = T_c$) [16].

UPt_3 was described as antiferromagnetic below T_N = 5 K with tiny U magnetic moments (μ = 0.02 μ_B). It shows a coupling between the superconducting and magnetic order parameters. UPt_3 has a multiple superconducting phases, which can be observed as a peaks at $C(T)$ below the T_c = 0.5 K [17].The value of electronic specific heat coefficient γ_e = 0.4 J/K^2·mol U is extremely high.

Other example of coexisting superconductivity and some kind of magnetic order can be ternary uranium compounds URu_2Si_2, UPd_2Al_3, UNi_2Al_3. The Néel temperature and magnetic moment are respectively T_N = 17.5 K; 14 K; 5 K, μ = 0.03 μ_B/U (not really intrinsic); 0.85 μ_B/U; 0.24 μ_B/U for URu_2Si_2, UPd_2Al_3 and UNi_2Al_3 [18]. The values of T_c for these compounds are respectively 0.8 K; 2 K; 1 K.

In URhGe, itinerant 5*f* ferromagnetism with T_C = 9.5 K and μ = 0.3 μ_B/f.u. coexists with superconductivity, which appears below T_c = 0.26 K [6,19]. URhGe

exhibits huge magnetocrystalline anisotropy. Specific heat studies have revealed a high value of the γ_e coefficient (160 mJ/mol K^2) [20].

Coexistence of magnetic order and superconductivity can be also induced by pressure. UGe_2 is a ferromagnetic below T_C = 53 K at ambient pressure [21]. Depending on temperature UGe_2 contain two ferromagnetic phases. UGe_2 becomes superconducting at pressures 10-15 kbar and temperatures below 0.8 K.

3. γ – uranium phase

Uranium metal can exist in 3 allotropic phases (fig. 3.1): α-phase with an orthorhombic structure (space group *Cmcm*), β-phase with a tetragonal structure (space group $P4_2/mmm$), and γ-phase with a body centered cubic A2-type structure ($Im\bar{3}m$).

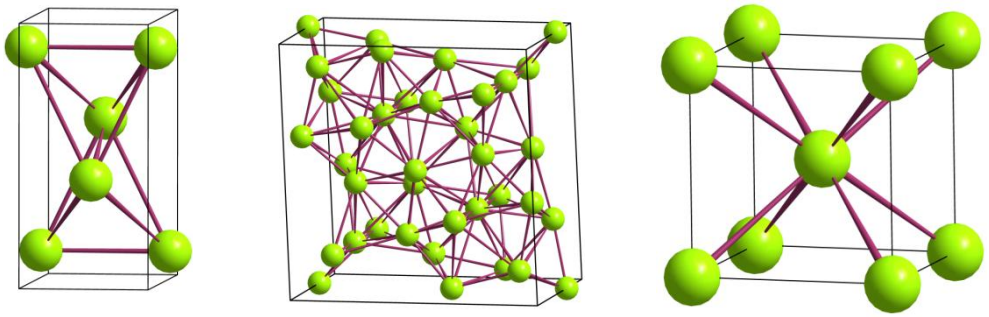

Figure 3.1. Crystal structures of uranium allotropic phases: α-U (left), β-U (centre) and γ-U (right).

α-uranium phase is stable at room temperature (below 942 K) while β-phase and γ-phase are stable at higher temperatures, 942-1049 K and 1049-1408 K [22], respectively. That is the reason why the γ-U phase has not been so far thoroughly investigated. Electronic properties are well known only for α-U which is stable at room temperature. It exhibits anomalies at low temperatures (23 K, 37 K, 43 K) observed in the temperature dependence of magnetic susceptibility, electrical resistivity, and specific heat [23]. These anomalies are attributed to charge density waves. Superconductivity with T_c = 0.78 K was reported for α-U, although recently it was suggested that the developed charge-density-wave state prohibits the superconductivity [1,23,24]. α-U is weakly paramagnetic with almost temperature-independent susceptibility of $4.9 \cdot 10^{-12}$ m^3/mol ($390 \cdot 10^{-9}$ emu/mol) [22].

α-U and γ-U phases may have different electronic properties, as their density is lower (18.06 g/cm^3 for γ-U comparing to 19.04 g/cm^3 for α-U). The γ-U unit cell parameter (extrapolated to room temperature) is a = 3.472 Å [25].

In the A2 arrangement, each atom is surrounded by eight equidistant neighbours in a cubic coordination polyhedron. The shortest inter-uranium distance

is enhanced from 2.837 Å for α phase to 3.01 Å in γ phase (extrapolated to room temperature). So it could be a convenient way to study effect of small changes of localization within one element in different crystal structures. Such increase in inter-uranium distances can affect electronic properties, as 5*f* band become narrower and density of states at the Fermi level is increased.

Similar comparison of different phases of the same element was performed for the low-volume monoclinic α-Pu and *fcc* δ-Pu (stabilized by few percent doping of Al, Ga, Am or Ce) with volume more than 20% higher, which has γ_e dramatically enhanced from 17 mJ/mol K^2 to about ≈ 40 mJ/mol K^2 (for δ-Pu), pointing to importance of strong electron-electron correlations in δ-Pu [26]. From other Pu phases, there exists only partial information on β-Pu prepared by quenching to very low temperatures [27].

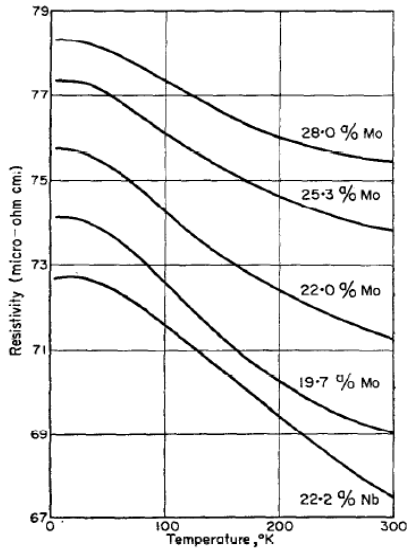

Figure 3.2. The resistivity temperature dependence for γ-U stabilized U-Mo and U-Nb alloys [28].

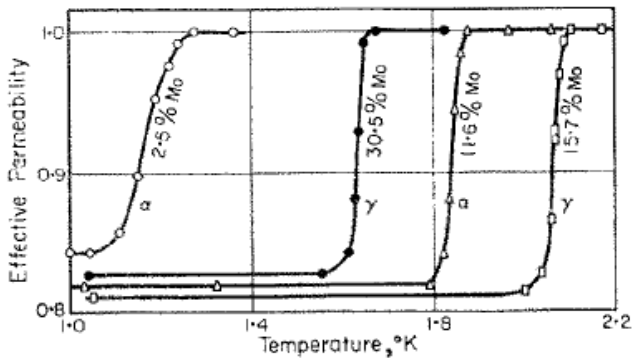

Figure 3.3. The effective permeability temperature dependence for γ-U and α-U alloys with Mo doping (measuring field 5×10^{-4} T) showing transition to superconducting state [28].

As mentioned above, the γ-U phase is stable only at high temperatures (1048-1408 K). Nevertheless, γ-phase can be retained to the room temperature by doping of some stabilizing elements (Ti, Zr, V, Nb, Cr, Mo, Re, Pt, Pd and Ru [2,36]) with fast cooling techniques (water quenching, melt spinning, splat cooling). Some works from 1960's can be found in which properties of γ-U phase stabilized by Mo doping are described [28,29,30].

It is known from the work of Chandrasekhar [28], that the U-Mo alloys, which were annealed at 900°C (1173 K) and subsequently rapid water-quenched, have the *bcc* phase retained and exhibit interesting electronic properties. In particular, the γ-U phase was retained for Mo concentrations above 15 at.%. These samples were considered as γ-U, but actually contain still some α-U phase. The residual resistivity values for γ-U samples are very high in comparison with α-U samples and reache the values of about 100 μΩcm. The temperature dependence of electrical resistivity (fig. 3.2) for γ-U samples is quite flat and even has a small negative temperature coefficient, which is a deviation from the Matthiessen's rule. Its reason can be seen in weak localization [31], which appears under conditions of strong disorder, and which is partly suppressed by electron-phonon scattering at elevated temperatures. It is nowadays believed to give explanation for the Mooij criterion, relating the appearance of the negative slope to enhanced residual resistivity ρ_0 [32].

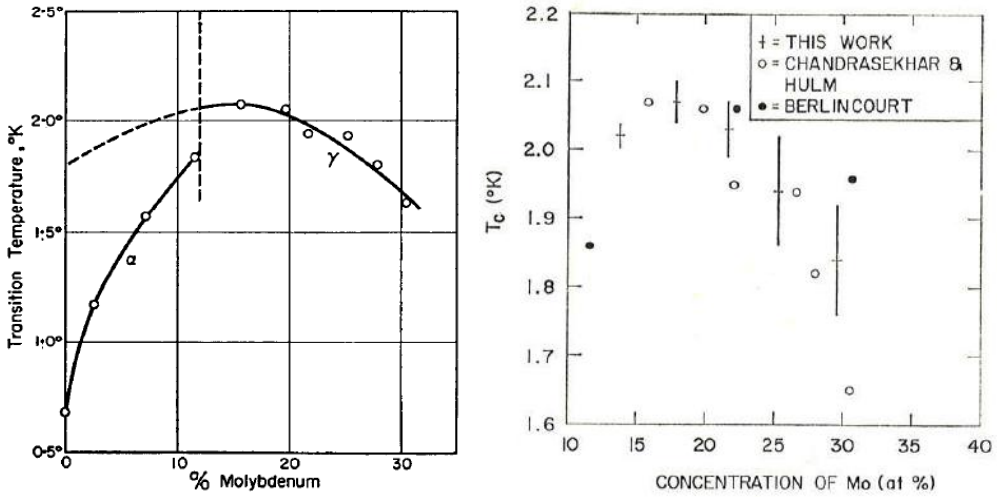

Figure 3.4. Superconducting transition temperature vs. concentration of Mo (left [28], right [33]).

The samples were tested for superconductivity by measuring temperature dependence of effective permeability down to 1 K (fig. 3.3). All U-Mo samples (both α-U and γ-U) become superconducting with a sharp transition and the highest critical temperature equal 2.1 K for the sample with 15 at.% Mo (fig. 3.4) [28]. Similar results were described in the work of Berlincourt [30] for U-Mo alloys. Measurements of low-temperature specific heat between 1 K and 4 K also confirmed superconductivity of γ-U alloys with Mo. The Sommerfeld coefficient is enhanced from values about 9-11 mJ/mol K^2 [23] for pure α-U up to 15-17 mJ/mol K^2 for γ-U

alloys [33] signifying increase in DOS at the Fermi level. Also the Debye temperature is decreasing from 206 K for α-U to 127.5 K for γ-U alloys which can be ascribed to the softening of the lattice.

For the U-Zr alloys there exists much less literature data about electronic properties. A higher concentrations of dopant is needed for the stabilization of U-Zr alloys in γ-U phase than in the case of Mo. Huber [34] described stabilization of single phase γ-U for concentrations from 25 at.% Zr to 80 at.% Zr by rapid cooling. Samples were found to be superconducting with sharp transitions. Superconducting transition temperature is increased with Zr concentration (fig. 3.5) and reaching approximately 1.3 K for sample with 80 at.% Zr. The temperature dependence of electrical resistivity was measured by Barnard [35] in the temperature range 90-1200 K for U-70 at.% Zr sample which was attributed to be metastable γ-U phase. As for others γ-U alloys, U-70 at.% Zr also exhibits a decrease of electrical resistivity with increasing temperature.

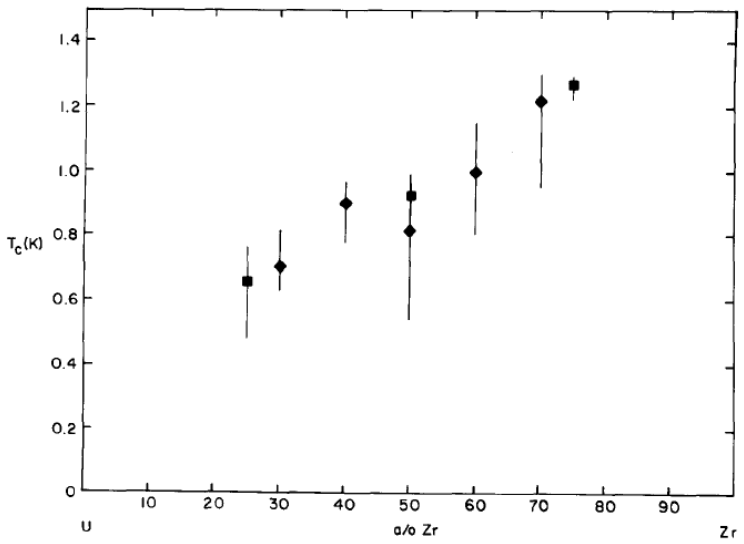

Figure 3.5. Superconducting transition temperature vs. concentration of Zr [34].

Majority of research of U-Mo alloys has been motivated by practical interests. Massive research programs in USA were launched in the late 70's to convert nuclear research reactors from the use of highly enriched uranium (HEU) to low enriched uranium (LEU; < 20% ^{235}U) fuels. In order to develop LEU fuels, many different uranium alloys were tested. The main goal was to develop a high-uranium density fuel that remains stable in the *bcc* structure of γ-U phase during fabrication and irradiation [36]. The U-Mo alloys turned out to be the most promising candidates,

since they fulfil the requirements to use the LEU in reactors while also preserving the γ-U phase with a high U density and stability under irradiation [2,37], e.g. they are more resistant to swelling than α-uranium based fuels [38]. U-Mo alloys were also found to be the top performers among many U-based fuel alloys in the screening-tests. More recently U-10wt.% Mo was selected for the U.S. reactors, while many European reactors continue to use the U-7wt.% Mo. Burke et al. and Brewer et al. [39,40] reviewed the physical and metallurgical behavior of U-Mo alloys up to the year 1980, while the phase diagram of this system up to the year 1967 has been reviewed by Hawkins and Hultgren [41,42].

Similar to U-Mo alloys, also U-Zr alloys were considered as a candidate for uranium fuel. In monolithic form these alloys can be used for fast reactors and in dispersion form in thermal reactors. U-Zr alloys have an excellent thermal conductivity [43] and high solidus temperature. Many works concentrated on irradiation properties and metallurgical aspects [44,45,46,47]. Phase transformation under quenching is described by Hills [48]. Microstructure investigation and thermal properties were studied by Bagchi [49].

Many other metals were tested with variable results to yield the γ-U phase retained at room temperature together with quenching (Ti, Zr, V, Nb, Cr, Mo, Re, Pt, Pd and Ru) [2,36]. Some of these dopants do not have sufficient solubility range with uranium to retain the γ-U phase and start to form stable compounds with uranium (Pt, Pd). Other dopants have complete solid solution with uranium but need a very high concentrations in order to get single-phase γ-U samples (Zr, Nb) [2]. As we are primarily interested by the "intrinsic" characteristics of γ-U phase, we have to work with as little dopant concentration as possible, and we therefore focused mainly on the Mo doping, which is recognized to be the most efficient among the stabilizing dopants [2,36,50].

In this work we used for comparison the Zr and Mo doping. Zr has a large solubility range in U but takes higher concentrations to stabilize the pure γ-U phase than with the Mo doping. Different dopants help us better understand changes in electronic properties of the samples. Zr, U and Mo have atomic radius equal to 1.60 Å, 1.56 Å and 1.40 Å, respectively. We can observe both effects related to expansion/compression of the lattice due to different atomic radius of the dopants.

By modification of lattice parameters we change also the shortest inter-uranium distance, which has a high influence on electronic properties of U-systems.

It should be noted, that by “stabilization” we actually mean “retention”, because these alloys are metastable from the thermodynamical point of view. Let's look now at the respective phase diagrams.

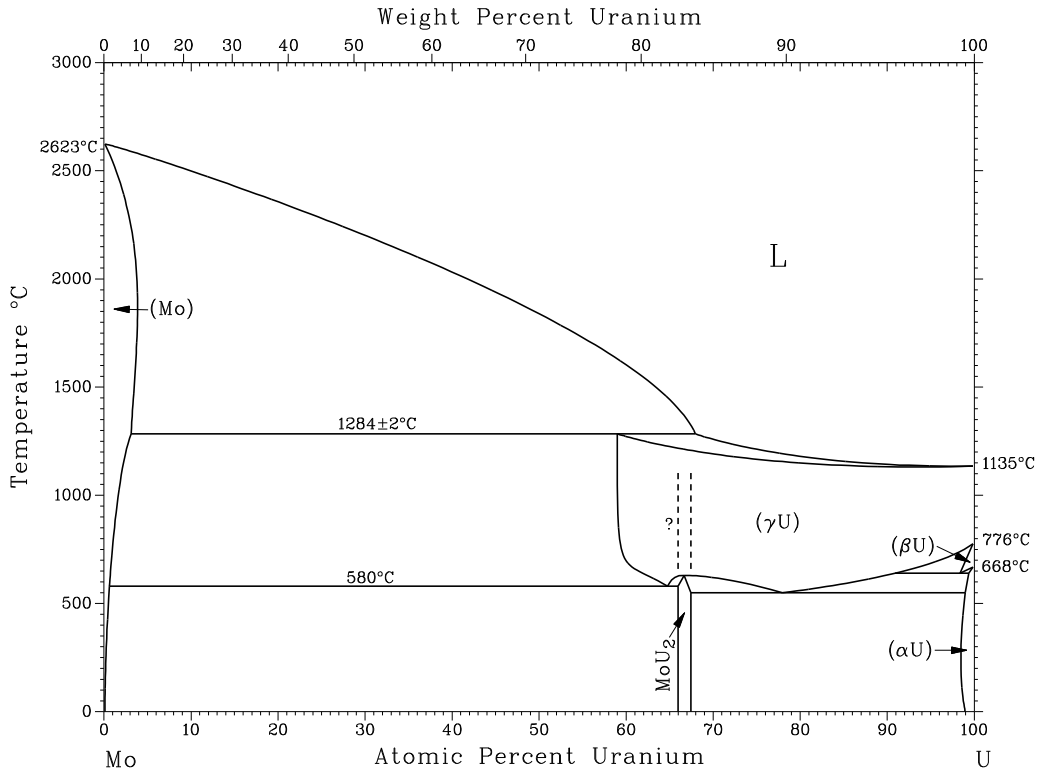

Figure 3.6. Binary phase diagram of the U-Mo system [51].

At high temperatures, the U-Mo system in equilibrium has a cubic structure (γ-phase) for a solid solution in the range of 0 - 41 at.% Mo (fig. 3.6). Depending on the solute content and the quenching rate when U-Mo alloys are quenched from regions of γ-phase stability, combinations of α–U, β-U and γ-U and γ-like phases can occur after partial decomposition of the γ-phase. For instance, cooled below 833 K, the metastable cubic γ-phase undergoes eutectoid decomposition to form the (equilibrium) orthorhombic α-phase and body centred tetragonal γ'-phase (U_2Mo intermetallics) [2]. U_2Mo (space group *I4/mmm*) is an ordered phase in the U-Mo system, which is a variant of γ phase with the atoms slightly displaced from their ideal *bcc* positions in the (001) directions (the tetragonal *c*-axis) which arrange themselves in a closer spacing than the γ-phase [52]. The unit cell parameters of

U_2Mo are: a = 3.427 Å, c = 9.834 Å; c/a = 2.86). The so-called γ^o-phase [52,53,54] can be also formed in quenched U-Mo alloys. Such a phase was considered as a normal tetragonal structure with a small contraction of the original *c*-axis of the *bcc* cell, i.e. with lattice parameters $a(\gamma^o) = a(\gamma)$ and $c(\gamma^o)$ slightly less than $c(\gamma)$ and the ratio c/a being very close to 1.0 [31]. However, other authors considered the tetragonal γ^o phase to be related to the *bcc* cell by doubling *a* and contracting the original *c*-parameter, i.e. $a(\gamma^o) \approx 2 \cdot a(\gamma)$ and $c(\gamma^o)$ slightly less than $c(\gamma)$, so the ratio c/a is very close to 0.5 (i.e. 2x2x1 *bcc* cell) [52,54]. The important issue is that by choosing a proper combination of Mo content and cooling rate (from the high-temperature solid solution to room temperature), the metastable γ-phase can be retained at room temperature.

The minimum required molybdenum concentration to ensure a single-phase γ-alloy under normal furnace cooling conditions (as-cast) has been reported to be 16.5 at.% Mo (8 wt.% Mo) [2]. Using centrifugal atomization method, the atomized powder of a single-phase γ-U alloy was reported for U-4 at.% Mo alloy (2 wt.% Mo) [55]. The single-phase γ-alloy has also been obtained with 13 at.% Mo using an additional sample treatment (e.g. hardening and annealing [56] or annealing at around 1300 K for 24 h [57]). A sharpening of the XRD peaks after annealing certainly indicated an enhancement of the γ-phase concentration by improving the molybdenum homogeneity due to diffusion [57]. Alloys containing more than 11 at.% Mo, when water quenched, are often termed as ‘‘gamma phase’’ alloys as the extant structures are related to the bcc structure [54]. Indeed, a body centred tetragonal structure, designated γ°-phase, is obtained in water quenched alloys containing 11.39 at.% Mo and/or 12.73 at.% Mo in air cool [54]. However, alloys containing 12 at.% Mo quenched into cold media (e.g. water or flowing cold helium from 1073 K) exhibited a mixed α_b" monoclinic phase (major) with some co-existing γ-like phase [58], while alloy with 11.6 at.% Mo after annealing at 1223 K for 2 h with subsequent water-quenching exhibited only the cubic γ-phase in its makeup [30].

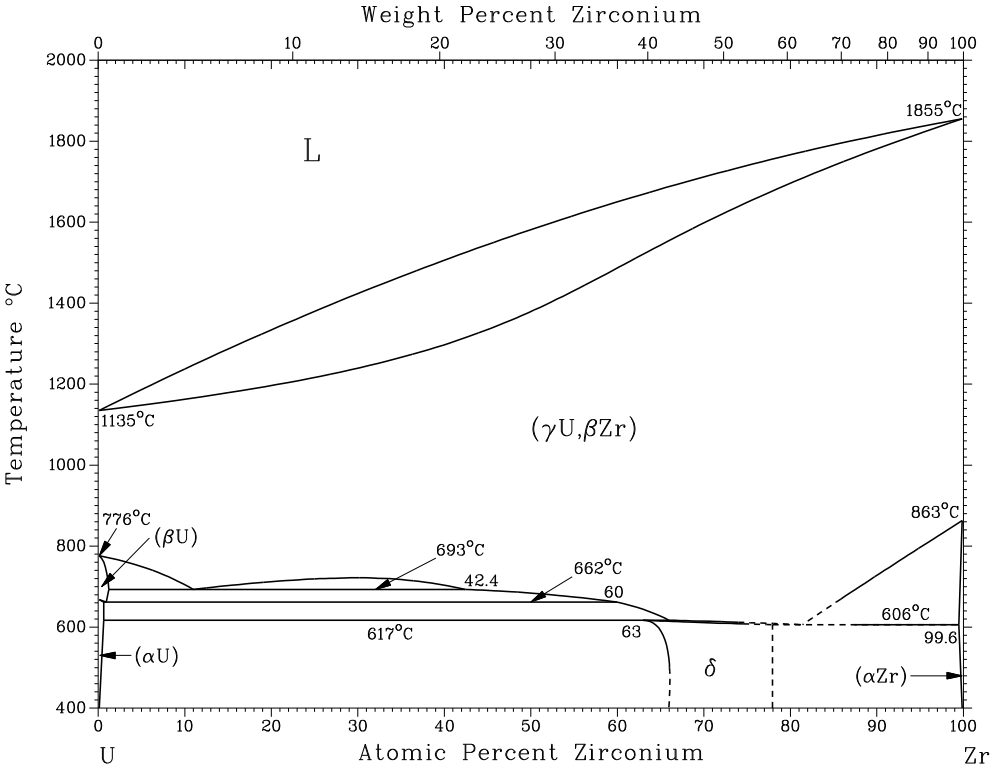

Figure 3.7. Binary phase diagram of U-Zr system [51].

The U-Zr system phase diagram is presented on fig. 3.7. In U-Zr system γ-phase of uranium with *bcc* structure has a full solid solubility range with β-Zr. Only one intermetallic compound of UZr_2 (also called as δ-phase) can be found which is formed at Zr concentrations approximately 22-34 at.%. The δ-phase has a hexagonal structure (with a space group *P*6/*mmm*), in which the corner positions (0,0,0) are occupied by Zr atoms and the sites (1/3,2/3,1/2) and (2/3,1/3,1/2) are randomly shared by U and Zr atoms [49]. γ^o phase, which was mentioned above for U-Mo system, was also observed in U-Zr system [59]. According to phase diagram at 606°C (879 K), γ-U phase decomposes into α-Zr and δ(UZr_2) phases. Depending on Zr concentration and a cooling rate combinations of different amount of γ-U can be retained to room temperature. The minimal concentration of Zr needed for metastabilization (retention) of single-phase γ-U sample by fast cooling was reported to be 25 at.% Zr [34]. XRD investigation revealed increase in lattice parameters with addition of Zr (from a = 3.55 Å for U-25 at.% Zr to a = 3.57 Å for U-80 at.% Zr).

4. Hydrides

As already mentioned in previous chapters, *f*-electron systems are sensitive to variations of interatomic distance and can dramatically change electronic properties due to external variables or changes in composition. For that reason investigation of compounds under pressures is quite important because it can lead to better understanding of electronic structure.

Hydrogenation is used as an effective way to study the behavior of compounds at volume expansion of crystal lattice. Hydrogen atoms are small and usually occupy interstitial lattice sites of a metal, while expanding the lattice. In uranium, increase of lattice parameters and inter-uranium distances lead to changes in electronic and magnetic properties. Such expansion due to additional hydrogen atoms in interstices can be considered as a "negative" pressure. Experiments with hydrides can give more information in addition to standard experiments under hydrostatic pressure with parent compounds.

Crystal structure of a hydride depends on structure of its parent compound and conditions (temperature, pressure), at which hydrogenation process takes place. Hydrogen atoms occupy some preferred interstices. For simple crystal structures there exist only two types interstitial sites, namely octahedral and tetrahedral, which are occupied by hydrogen (fig.4.1).

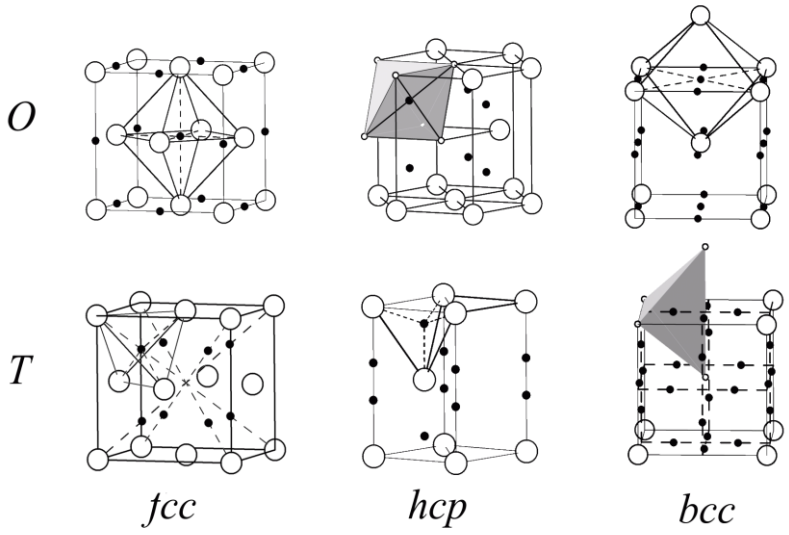

Figure 4.1. Interstitial sites (octahedral (*O*) and tetrahedral (*T*)) in face-centered cubic (*fcc*), hexagonal closed-packed (*hcp*) and body-centered cubic (*bcc*) structures. The interstitials are shown as black dots [60].

Compounds can form a hydride if they fulfill certain conditions: geometrical factors, crystal structure, surface properties, electronic factors, diffusive kinetics, etc.. Prediction of possible hydride formation can be made in a simple way by using geometrical criteria. The Westlake's criterion describes that in parental metal should be available interstitial sites with a spherical volume with radius ≥ 0.4 Å [61,62,63]. The minimum H-H distance should be 2.1 Å. By the Shoemaker's exclusion rule two tetrahedra of one face cannot be occupied at the same time [64]. All these criteria are used just for prediction and have numerous exceptions.

4.1. Uranium hydride

Uranium metal can form a hydride in two modifications, both having same content of hydrogen (3 H atoms per 1 U atom).

α-UH_3 is formed during a slow reaction at low temperatures. α-UH_3 forms as a metastable phase in the early stage of hydrogenation and transforms fast at elevated temperatures into β-UH_3 [65]. Usually α-UH_3 is prepared in mixture with large portion of β-UH_3 phase. α-UH_3 has a cubic crystal structure (space group *Pm3n*) (fig. 4.2) and lattice parameter a = 4.160 Å [66]. Two uranium atoms occupy (0,0,0) and (1/2,1/2,1/2) sites, and six hydrogen atoms ±(1/4,0,1/2), ±(1/2,1/4,0), and ±(0,1/2,1/4) sites which form an isocahedron [22,66]. The shortest inter-uranium distance in α-UH_3 is close to 3.6 Å, which is larger than the Hill criterion value.

The fact that α-UH_3 was never studied in a pure form but always in a mixture with β-UH_3 is reflected in uncertainty in its type of ground state. Earlier works, reviewed in Ref. 67, deduced magnetic ordering in α-UH_3 with T_C practically coinciding (178 K) with that of β-UH_3. In a later neutron diffraction of α-UD_3 (sample is mixture 1:1 of α and β phases) it was identified as non-magnetic [68]. That would seriously contradict to the concept of the U magnetism depending on the 5*f*-5*f* overlap. The density of α-UH_3 (11.12 g/cm^3) is slightly higher than for β-UH_3 (10.92 g/cm^3), but the shortest U-U spacing 3.6 Å is considerably larger than 3.3 Å for β-UH_3.

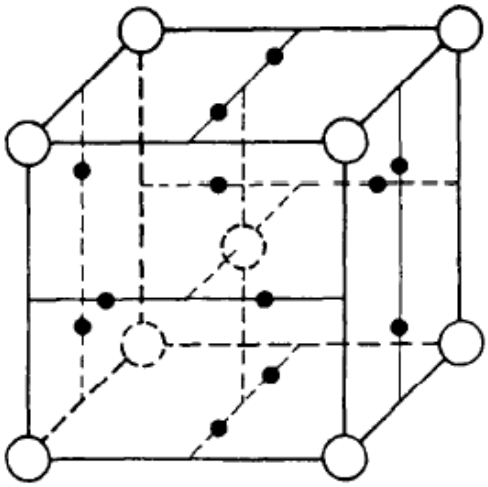

Figure 4.2. Crystal structure of α-UH_3 [69], where large open circles are U atoms and small solid circles shown hydrogen atoms.

β-UH_3 phase is formed under normal conditions. β-UH_3 has also cubic structure, Cr_3Si structure type (*Pm3n* space group) and unit cell $a \approx$ 6.644 Å (fig.4.3). The shortest U-U spacing in β-UH_3 is 3.31 Å, which is below the Hill criterion value. Uranium in this structure can occupy 2 different positions: 2 atoms U_1 in (0,0,0) and (1/2,1/2,1/2); and 6 atoms U_2 in ±(1/4,0,1/2) and their equivalent positions [22]. The reaction is observed already at low H pressures and it is one of major concerns considering ageing/degradation of U metal products. The very fine β-UH_3 powder easily ignites at room temperature in air. Besides the high reactivity it is also have relatively low equilibrium H pressure (heating to almost 450 ^{o}C (723 K) is necessary to reach the equilibrium pressure of 1 bar) [22], which prevents to consider the relatively inexpensive U metal as a hydrogen storage medium.

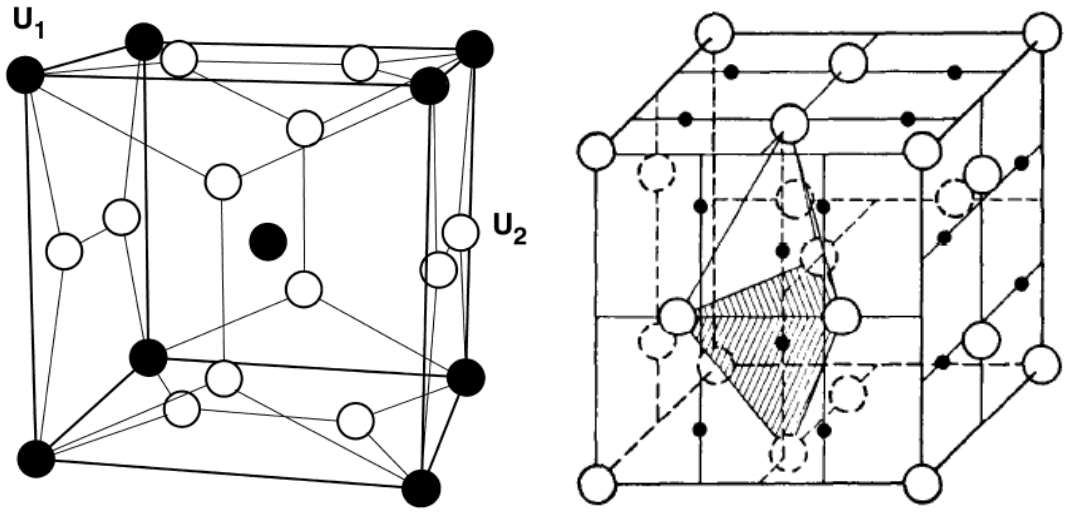

Figure 4.3. Crystal structure of β-UH_3, (left) where shown only uranium atoms in two possible types of U sites [70]. On the right panel by large open rounds shown U atoms and small solid rounds shown hydrogen atoms (not all hydrogen atoms are represented) [69].

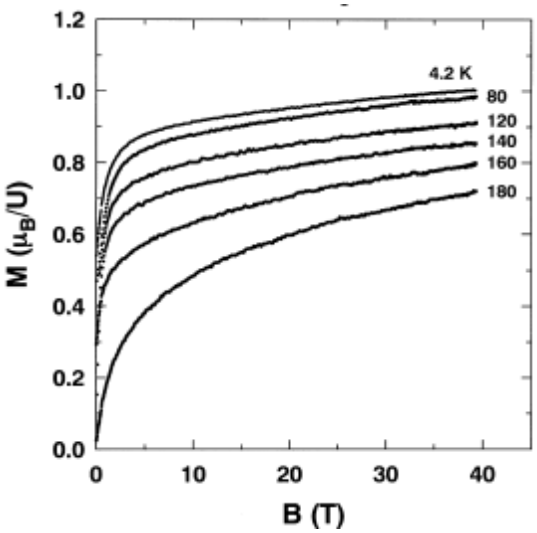

Figure 4.4. The high-field magnetization of β-UH_3 at various temperatures. [70]

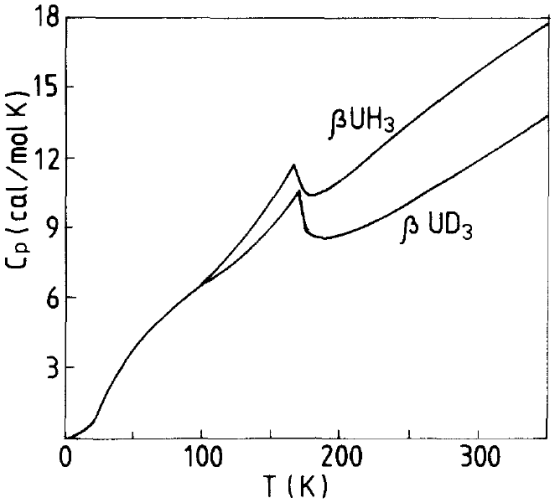

Figure 4.5. Temperature dependence of heat capacity for β-UH_3 and β-UD_3. [71,72,73]

An important aspect of β-UH_3 is its magnetic order reported already in 1952 [74]. The crystal structure expanded by H (the shortest U-U spacing in β-UH_3 is 3.31 Å, in uranium metal α-U it is merely 2.76 Å) leads to the formation of U magnetic moments of about 0.9-1.18 μ_B/U [22,70,75], possibly the same for each of two

different U positions. The effective paramagnetic uranium moment is in the range 2.24-2.79 μ_B/U [22], which is much smaller than expected for localized moments of free ions U^{+3} (3.62 μ_B) and U^{+4} (3.58 μ_B). Electronic structure calculations [69] revealed that both α-UH_3 and β-UH_3 structures favors *f* electron bonding with the hydrogen-derived states, β-UH_3 more so than α-UH_3. Magnetic moments are ordered ferromagnetically with the Curie temperature ranging between 168 and 181 K [22,70], which is in striking contrast to weak Pauli paramagnetism of uranium metal (α-U). Clear cusp can be observed on the temperature dependence of heat capacity (fig. 4.5) corresponding to the transition to magnetically ordered state.

The main reason for magnetic order is probably a reduction of the overlap of the 5*f* wave functions between nearest U neighbors, reducing the 5*f* bandwidth and increasing the density of states at the Fermi level, $N(E_F)$. The Sommerfeld coefficient of the electronic specific heat γ_e indeed increases by more than a factor of 3 from α-U (γ_e = 10.12 mJ/mol K^2; γ_e = 9.13 mJ/mol K^2 reported for a single crystal) [76,23] to β-UD_3 (γ_e = 33.9 mJ/mol K^2) [77] and to β-UH_3 (γ_e = 29 mJ/mol K^2; γ_e = 28.5 mJ/mol K^2 for thin film) [78,79]. The dramatic modification of the 5*f* states is actually demonstrated by high-resolution photoelectron spectroscopy [80]. Similar tendency to strengthen magnetic properties due to H-induced lattice expansion has been observed in numerous U-based intermetallic compounds [81].

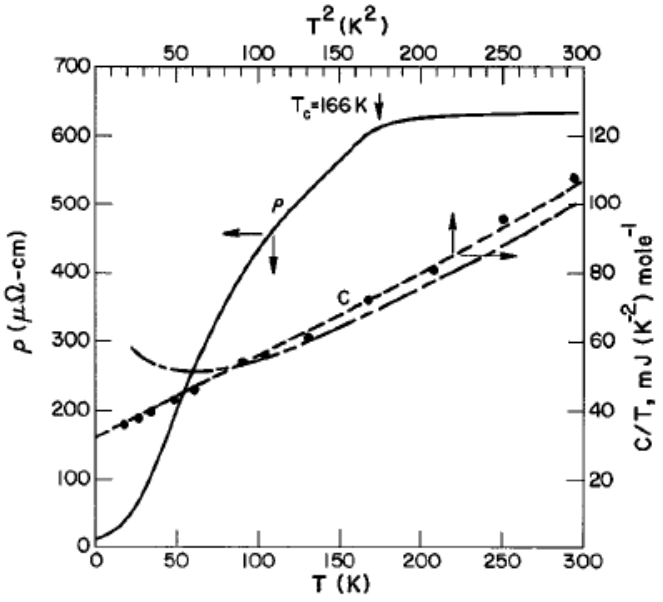

Figure 4.6. Temperature dependence of electrical resistivity of UD_3 [77].

Temperature dependence of electrical resistivity (fig. 4.6) was measured on β-UD_3 [77], which is an analog of β-UH_3, and could be prepared in monolithic form using high temperatures and very high pressures. The kink observed at 166 K corresponds to the Curie temperature. Resistivity values are very high, reaching about 600 μΩcm above T_C. Flotow measured the temperature dependence of resistivity of β-UH_3 but the data was remained unpublished [22]. The resistivity of hydride is about ten times higher than that of uranium metal. An explanation for the very high resistivity values can be seen in the reduction in concentration of conduction electrons due to hydrogen absorption.

5. Experimental

5.1. Sample preparation

5.1.1. Mono-arc furnace

The mono-arc melting furnace was used for preparation of the samples in the form of ingots. U–Mo and U-Zr alloys with various Mo and Zr concentrations were prepared from pure metals, of natural U (99.86% or better purity), Mo (99.95% purity) and Zr (99.8% purity). The mono-arc furnace consists of water-cooled copper crucible for samples, vacuum system with turbomolecular pump, W arc electrode, power supply and chamber (fig. 5.1). After all constituents of the sample are loaded in the crucible the chamber is evacuated to pressures $2 \cdot 10^{-6}$ mbar. After loading the chamber with pure argon atmosphere the arc can be ignited. For better homogenization, the ingots were turned over and re-melted 3 times. The weight of each specimen was approximately 200–350 mg, which is suitable for preparation of splat-cooled samples.

Figure.5.1. Photo of mono-arc furnace used for melting of initial components

5.1.2. Splat cooling

The alloys after melting in mono-arc furnace were subsequently transferred to the splat cooling system (high-vacuum splat-cooler produced by Vakuum Praha), which is also an arc-melter but the reaches the cooling rate up to 10^6 K/s. Due to high cooling rates splat cooling is considered as a very efficient technique for preserving high temperature phases and for reducing a grain-size to the order of nanometers or sometimes (depending on phase diagram) to amorphous structure.

The splat cooling system consists of high-vacuum chamber, arc electrode, copper crucible cooled by water, turbo pump, power supply and two copper anvils with electric capacitors (fig. 5.2). The chamber is pumped to pressure below $3 \cdot 10^{-5}$ mbar after the ingot is loaded to the edge of crucible. Alloy is melted by electrical arc in argon atmosphere. The molten drop of the alloy then falls through the hole in copper crucible, triggering an infra-red photoelectric switch that initiates movement of two anvils. When the droplet appears near anvils they entrap it and squeeze. The splat-cooled samples usually have an irregular disc-shape with a diameter of about 20 mm and a thickness of 100 - 200 μm. (fig. 5.3). This shape is convenient for further measurements of electronic properties like electrical resistivity and heat capacity.

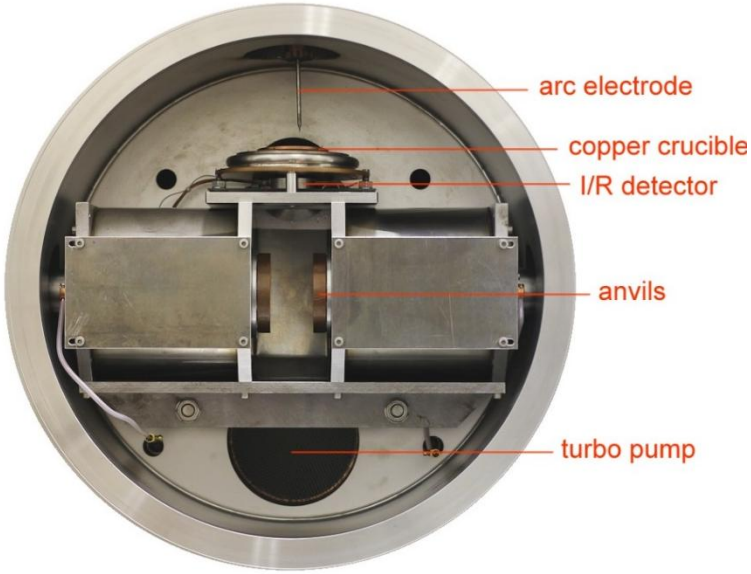

Figure 5.2. The high vacuum chamber of splat cooler by Vakuum Praha.

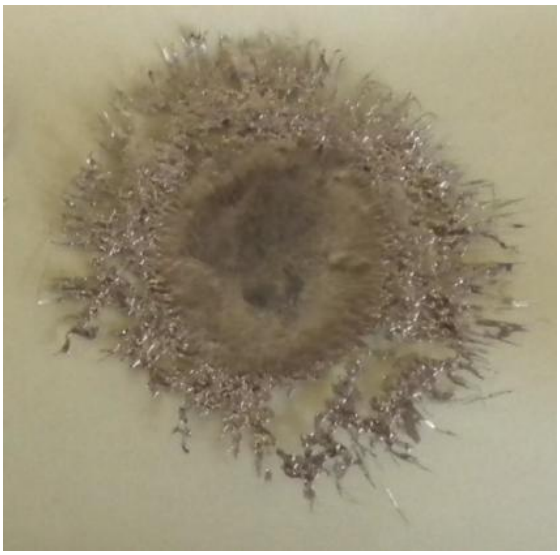

Figure 5.3. Photo of a splat cooled sample, with a diameter of about 20 mm and thickness 100-200 μm.

5.2. Hydrogenation and desorption experiments

Hydrogenation of U-Mo and U-Zr alloys was performed by means of the hydrogenation equipment at MFF UK (fig. 5.4). It consists of (fig. 5.5) reactor, H_2 container, heaters and vacuum pumps. The following procedure was performed for hydrogenation experiments. Sample was inserted into reactor (in an alumina crucible) and pumped down to pressures of 10^{-6} mbar. In our case we don't use any activation procedure (thermal desorption of impurities) before the hydrogenation experiment as it can cause decomposition of the starting metastable γ-U phase. From the same reason the hydrogenation was typically performed only at room temperature. After pumping was finished, hydrogen was released into the reactor with sample by heating the container with the $LaNi_5$ bed with absorbed hydrogen. Hydrogenation experiments were performed at various H_2 pressures. The maximal pressure applied was ≈ 100 bar. It was revealed that U-Mo and U-Zr alloys start to form a hydride at hydrogen pressures $P_H \geq 4.5$ bar. Hydrogen absorption was observed by the drop of pressure in reactor (fig. 5.6). When high pressures are necessary for hydrogenation of alloys, the relatively small drop of pressure can't be used for estimation of stoichiometry of observed hydride, as pressure variations due to small temperature variations can be larger than the pressure drop due to hydrogen absorption (several hundred mbar).

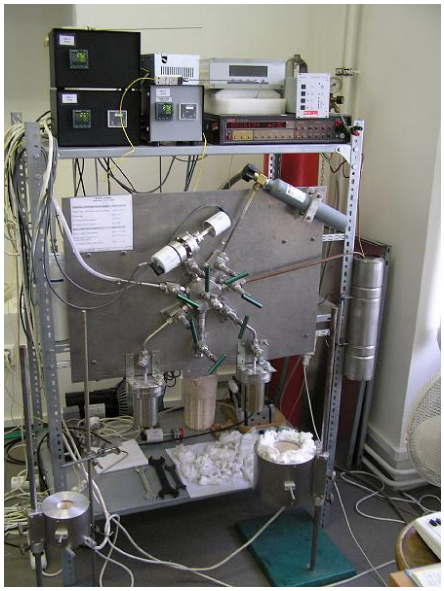

Figure 5.4. Hydrogenation equipment.

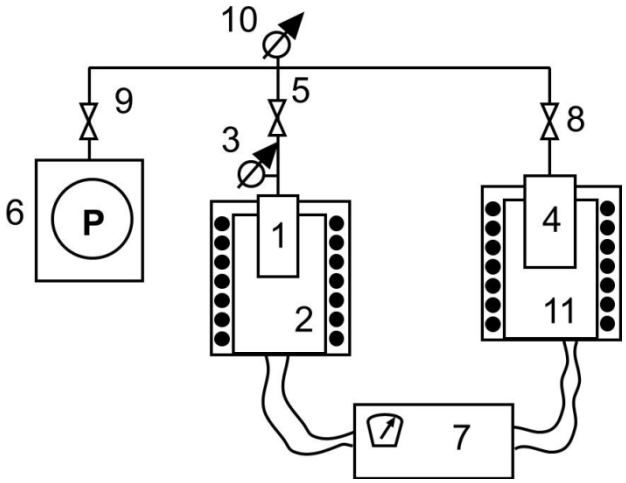

Figure 5.5. The scheme of hydrogenation equipment: 1 – reactor; 2, 11 – heaters; 3, 10 – vacuum gauges; 4 – $LaNi_5$ container with H_2; 5, 8, 9 – valves; 6 – vacuum pumps; 7 – temperature control unit.

In attempt to quantify the absorbed amount of hydrogen with better accuracy than during the absorption, hydride samples were decomposed in a close evacuated volume by heating to high temperatures (773-973 K). The stoichiometry of hydrides was calculated from the released amount of hydrogen in the calibrated volume. The desorption process consists of three stages. The first one is the heating of the reactor to temperatures ≈ 773-973 K with slow rate 2 K/min. During that process it is possible to observe increase of pressure inside reactor due to the release of hydrogen. Reaching certain temperature all hydrogen from the sample is released, which shows up as a plateau on the time dependence of pressure (fig. 5.7). After the heater is turned off, the sample cools down. Pressure decreases, which is, besides the direct effect on the gas in closed volume, in some cases also due to a re-absorption of part of the released gas. This happens when the equilibrium hydrogen pressure is lower than several tens of millibar obtained by desorption. Therefore is some cases the remaining desorbed gas was pumped out and the desorption process run for the second time. The total amount was obtained by summing both contributions.

After hydrogenation, the samples were crushed and subjected for further structure characterization by x-ray powder diffraction. Similar analysis was performed also with the material after desorption, which guarantees that all hydrogen left the sample. The procedures can be illustrated using the following figures.

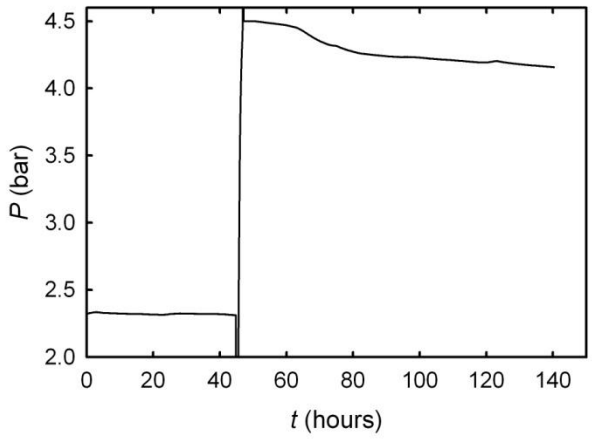

Figure 5.6. The time dependence of pressure for hydrogenation process of U-15 at.% Mo splat sample. Sample did not absorb hydrogen at H_2 pressure 2.5 bar, while at 4.5 bar absorption become visible.

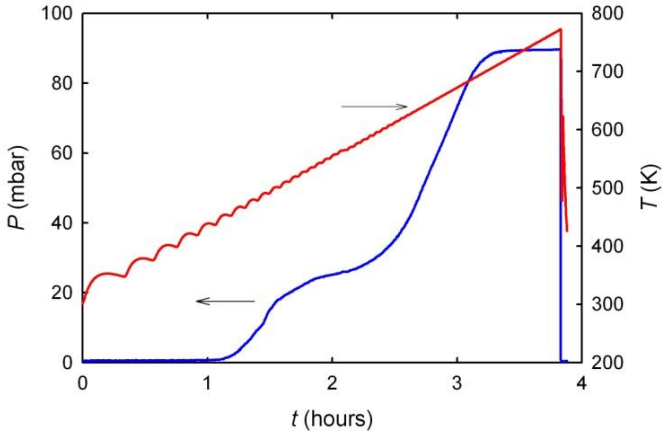

Figure 5.7. The dependence of hydrogen pressure and temperature of reactor during desorption experiment for $(UH_3)_{0.85}Mo_{0.15}$.

5.3. Structure characterization

5.3.1. X-ray powder diffraction

Sample characterization of the samples was performed using powder X-ray diffraction on the Bruker D8 Advance diffractometer and the Cu Kα radiation (λ = 1.54056 Å). Splat samples were measured directly from the surface of splats to avoid any possible decomposition due to mechanical treatments. In the case of hydride samples XRD patterns were obtained using powder samples.

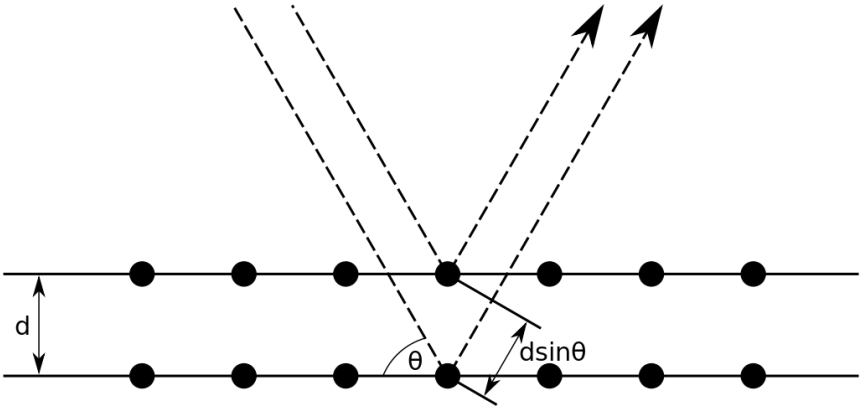

Figure 5.8. The scheme of crystal lattice diffraction of scattered waves.

Diffraction pattern is observed by measuring the intensity of scattered waves as a function of scattering angle. Diffraction peaks on the pattern appear after x-rays waves are reflected from different crystal planes and interfere between each other. This means that waves should be in the phase. Such a condition for interference of scattered waves from crystallographic planes is described by the Bragg law:

$$2d \sin \theta = n\lambda, \qquad (5.3.1.)$$

where d – the interplanar distance, λ – the wavelength, θ – the scattering angle, n – an integer.

In other words, difference in path for scattered waves should be equal to integer number of half wavelengths.

The crystal structure refinement was done by using the FullProf software which is based on the Rietveld analysis. The main principle of the Rietveld analysis

is to minimize the function *S* (by using a least squares approach) which is represents the difference between a calculated profile y_{ic} and y_{io} and the observed from measurement profile at *i*-th step.

$$S = \sum w_i |y_{io} - y_{ic}|^2, \quad (5.3.2.)$$

where w_i is the statistical weight given by

$$(w_i)^{-1} = \sigma_i^2 = \sigma_{ip}^2 + \sigma_{ib}^2, \quad (5.3.3.)$$

σ_{ip} is the standard deviation associated with the peak intensity due to the counting statistics and σ_{ib} is that relates to background intensity.

5.3.2. Scanning electron microscopy

Scanning electron microscope (SEM) was used for microstructure analysis of splat samples. Microstructure investigation by Electron Back Scattered Diffraction (EBSD) mapping and X-ray energy dispersive microanalysis (EDX) were performed by means of the scanning electron microscope with spatial resolution 1 μm. For some of the samples the FEI Quanta 200 FEG microscope was used, which has much higher spatial resolution (50 nm).

SEM is a type of microscope which can image a sample by focused electron beam. Information about the sample structure and microstructure can be obtained from different sources: secondary electrons (SE), backscattered electrons (BSE), electron backscatter diffraction (EBSD) and energy dispersive X-rays (EDX).

Secondary electrons are emitted by atoms excited by primary electron beam. Usually only low energy electrons are collected for SE images, which are emitted from the first inner electron shell of atoms (*K*-shell). As these electrons have low energy they originate from the surface layer only few nanometers. Secondary electrons provide information about surface topography.

Backscattered electrons are high-energy electrons reflected from the surface by elastic scattering. It is possible to see the contrast on BSE images between areas with different composition, as heavier atoms with higher atomic number *Z* scatter electrons stronger than lighter atoms. BSE provide information about chemical elements distribution in the sample. BSE are also used for electron backscatter

diffraction (EBSD). By EBSD it is possible to index orientations of grains, determine texture, defects, phases and grain boundaries. By scanning the sample and indexing phase and orientation of grain at each point it is possible to build a phase distribution and orientation maps of some area at the sample surface. Example of such orientation map is presented on figure 5.9.

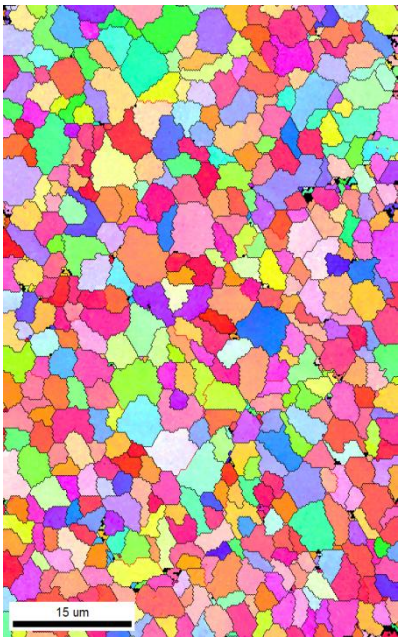

Figure 5.9. Example of orientation map for splat sample U-11 at.% Mo.

Some of SEM can be equipped by focused ion beam (FIB). FIB can be used for cutting the sample by Ga ions. Such cuts made by FIB allow to image and investigate not only the surface of sample but also deeper inside the sample, making cross-section mapping or tomography.

Chemical analysis of the sample can be performed by using energy dispersive X-ray spectroscopy (EDX). EDX method is based on characteristic energies in X-ray spectra for different chemical elements. The high-energy electron beam of SEM can excite and eject an electron from an inner shell of the atom. Electron from the outer shell can fill this electron hole in inner shell and emit X-rays with energy equal to the difference of shells energies. These characteristic energies are detected by EDX detector. It is possible to know from the EDX spectrum peaks (fig. 5.10) which chemical elements are in the investigated area and how large concentration of these

elements. By making an EDX scanning of some area we can find a distribution of elements in sample.

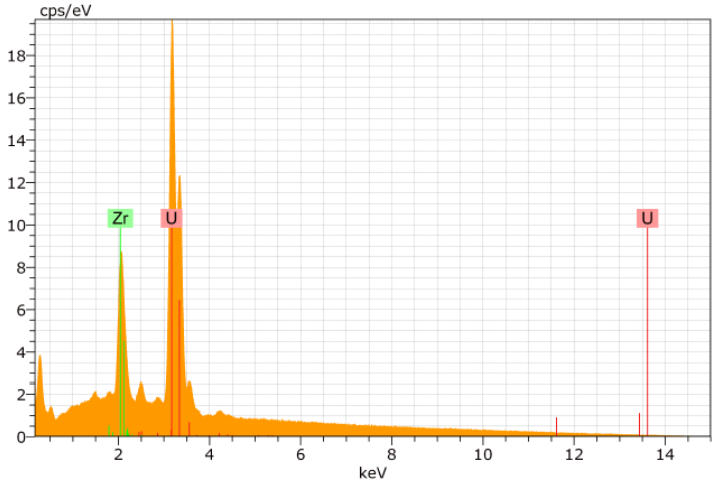

Figure 5.10. Example of EDX spectrum for one of U-Zr samples.

In our work we used two different equipment

5.3.4. Transmission electron microscope

Transmission electron microscopy (TEM) is a technique which uses the information from a beam of electrons transmitted through a thin sample. The microscope consists of electron gun, series of electromagnetic lenses, vacuum camera, and imaging devices (fluorescent screen or CCD camera). A high-voltage current in the electron gun forms an electron beam which is then focused by a lens system. Transmitted electrons are in the form of black and white image which represents information on the structure, texture, shape and size of the sample. White parts of the image shows low density areas where more electrons pass through. Black part shows more dense regions of the sample.

The main advantage of this type microscopy is a very high resolution of images, which can exceed 1 nm. In addition, samples can exhibit diffraction contrast which can be observed in the back focal plane. The diffraction pattern provides information about the space group symmetry and crystal orientation.

In our experiment the JEOL JEM 2000 FX microscope was used. The sample ($(UH_3)_{0.85}Mo_{0.15}$) particles were crushed up to fine powder by hand milling in

crucible under acetone. The powder obtained was fixed between two Cu grids and holey carbon layers and was subjected for further investigation by TEM.

5.4. Magnetization measurements

Measurements of magnetic properties were performed using the Physical Property Measurement System (PPMS) and Superconducting Quantum Interference Device (SQUID) magnetometer by Quantum Design. Samples were crushed and prepared as randomly oriented powder fixed inside a plastic straw by glue. The random orientation prevents any influence of texture of sample and possible rotation of particles in magnetic fields. The mass of each sample was typically 50-100 mg. Measurements were performed in temperature range 2-300 K and in applied magnetic fields up to 14 T. The basic instrument is an extraction magnetometer, which registers a change of magnetic flux (proportional to magnetization of the sample) induced by extraction of sample from a coil placed into a static magnetic field.

Then same setup is used for AC magnetic susceptibility measurement (ACMS). The sample with a given magnetization affects the coupling between a primary coil and detection (secondary) coil. Small oscillating AC magnetic field is superimposed on the DC field (which can be zero or a given non-zero value). The time-dependent magnetic moment of sample in oscillating field induces a current in the detection coil according to the Faraday law. From these measurements we obtain not only the values of $\chi = dM/dH$, but also real χ' and imaginary χ'' components. This method is very sensitive for thermodynamic phase changes and usually used for determination of transition temperatures (Curie temperature for ferromagnets).

Vibrating Sample Magnetometer (VSM) was used in this work for magnetic susceptibility measurements of splat samples. The principle is similar to ACMS and based on the Faraday law. The sample is mounted on the rod (sample holder) and placed into pickup coils. The oscillator moves the sample holder and makes vertical vibrations with a given frequency and amplitude. All the setup is located into static magnetic field produced by a superconducting solenoid. The oscillations of the sample induce a voltage in pickup coils. Using the Faraday law it is possible to

deduce the magnetization of the sample, i.e. magnetic susceptibility, from the induced voltage.

High field magnetization measurement was performed in a pulsed magnetic field up to 60 T at Dresden High Magnetic Field Laboratory. High magnetic fields can be obtained only for a very short period (about 10 milliseconds) due to a high force which explodes the coils. For that reason, a large bank of capacitors is used for discharging in coils. That creates a pulse of high magnetic field up to 100 T for a short period.

5.5. Heat capacity measurements

For heat capacity measurements splat samples were cut by spark erosion into rectangular-shape pieces approximately 2×2 mm^2. In the case of hydrides produced from ingots we use larger bulk pieces. Hydrides which were produced from splat samples consisted from too small particles. We used a hydraulic press to produce the pellets, pressed hydride powders. Samples were measured by using the PPMS Heat Capacity Option in temperature range 2-300 K. For investigation of superconducting transitions we use Helium-3 insert which allows performing measurements down to 0.4 K. Magnetic field up to 6 T was also applied.

Sample is mounted to a platform of the calorimeter puck with a small amount of Apiezon N for better thermal contact. Thermometer and heater are attached to bottom side of the sample platform. The platform is connected to main body of the puck only by small connecting wires (fig. 5.11). After the sample is mounted, the colorimeter puck is installed inside the PPMS and pumped down to a high vacuum. This provides a sufficient thermal equilibrium during a measurement.

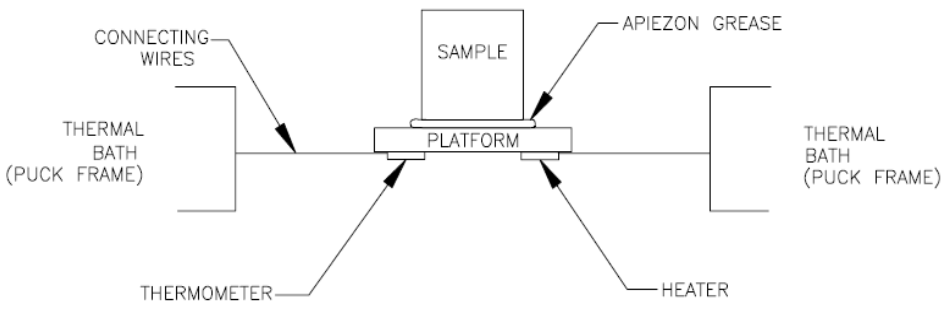

Figure 5.11. The principal scheme of the sample mounting puck for heat capacity measurements.

PPMS Heat Capacity option measures the heat capacity by relaxation method at constant pressure $C_p = \left(\frac{dQ}{dT}\right)_p$. During a measurement, a known heat pulse $P(t)$ with the constant power for a fixed time is applied to the platform, and then heating period is followed by a cooling period of the same duration.

The Heat Capacity option uses models to describe the measured temperature response and to give the values of heat capacity. The simple model is used in case of a good thermal contact between the sample and the platform so that temperatures T_{sample} and $T_{platform}$ can be considered to be the same. Thermal equilibrium of the platform with sample developing with time t obeys the equation:

$$C_{total}(T)\frac{dT}{dt} = P(t) - K_{wires}(T - T_{bath}), \qquad (5.5.1)$$

where C_{total} is the total heat capacity of the sample and sample platform; K_{wires} is the thermal conductance of the wires between platform and bath; T_{bath} is the temperature of the thermal bath (body of the puck); $P(t)$ is power applied by the heater. The solution of this equation for $T(t)$ is proportional to exponential function $\exp(-t/\tau)$, where $\tau = C_{total}/K_{wires}$ is the relaxation time

The two-tau model is used if thermal contact between the sample and the sample platform is not good enough. The two-tau model takes in account the heat flow between the sample platform and the sample. Following equations describe heat flow:

$$\begin{aligned} C_{platform}\frac{dT_{platform}}{dt} &= P(t) - K_{wires}(T_{platform}(t) - T_{bath}) + \kappa_g(T_{sample}(t) - T_{platform}(t)) \\ C_{sample}\frac{dT_{sample}}{dt} &= -K_g(T_{sample}(t) - T_{platform}(t)), \end{aligned} \qquad (5.5.2)$$

where Kg is the thermal conductance between sample and platform. In such case two τ are used for description of relaxation. τ 1 describes the relaxation between the platform and the thermal bath, τ 2 describes the relaxation time between the platform and the sample.

5.6. Resistivity measurements

The resistivity measurements were done by using PPMS with AC Transport Measurement System (ACT). ACT based on standard four-probe method: two contact wires for electrical current and two for voltage measurement (fig. 5.12). Measurements were done by passing a known AC current trough the sample and by measuring the drop of the voltage across the sample in one direction. The current in AC mode vary between +/- directions to remove the thermal voltage offsets. The resistance is calculated by the Ohm's law:

$$R = \frac{U}{I}, \qquad (5.6.1.)$$

where I is the electrical current and U is the drop of voltage on sample. Then resistivity can be calculated by:

$$\rho = R \cdot \frac{s}{l} = \frac{U}{I} \cdot \frac{s}{l}, \qquad (5.6.2.)$$

where s is the cross-sectional area of the sample through which current passes and l is the distance between voltage contact wires.

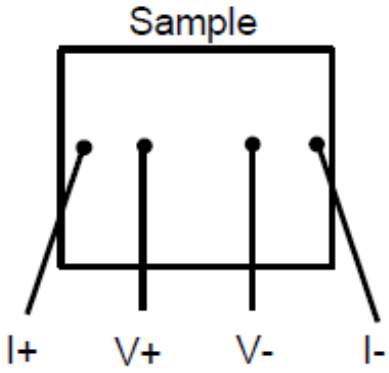

Figure 5.12. The scheme of electrical contacts for resistivity measurements.

For resistivity measurements, the splat samples were cut by spark erosion. Rectangular-shaped pieces of approximately 1 × 3-5 mm^2 were used for measurements. The length and the width of samples were determined by a caliper with error ± 0.5 mm. The thickness was determined by micrometer (error ± 0.005 mm) as our samples a in shape of foils. Due to irregular shape of our samples the actual error in determination of thickness could be larger (approx. ± 0.02 mm). In some cases for hydrides it was possible to find longitudinal particles (3-4 mm long),

which were suitable for resistivity measurements. The copper thin wires were used for electrical contact. In addition, colloidal silver paste was used to fix the wires to the sample. Measurements were performed in the temperature range 4-300 K, as standard, some samples were also studied at lower temperatures (0.4-4 K) using the ^{3}He insert. For investigation of superconducting transitions magnetic field up to 5 T was applied.

6. Results and discussion

6.1. Superconductivity of splat-cooled γ-U alloys

6.1.1. U-Mo splats

Samples of uranium doped by different concentrations of Mo (0 - 15 at.% Mo) were melted in argon atmosphere and subsequently moved to the splat cooling machine for preparation of splat samples. Here we will use different notations for the samples, $U_{1-x}Mo_x$ or U-*x* at.% Mo. For example, sample $U_{0.85}Mo_{0.15}$ can be also denoted as U-15 at.% Mo or U-15% Mo. The preparation methods were in details described in Chapter 5. At the beginning we characterized the crystal structure of our samples by XRD method and microstructure by SEM with EBSD.

The XRD patterns of the splat-cooled U-Mo alloys in the as-formed state are shown in Fig. 6.1. Diffraction patterns were measured directly from the surface of splats. For an easier comparison, we showed the normalized XRD pattern (i.e. the intensity of the most intense reflection at around $2\theta = 36^o$ was set to 1). They are then shifted upwards along the y-axis with respect to each other for clarity. Phase analyses using XRD information can be summarized as follow:

1) A double-phase (α+γ) structure was obtained in the splat-cooled U-Mo alloys with Mo content ≤ 10 at.%. EBSD revealed a small amount of the (cubic) γ-U phase retained at room temperature alongside the majority (orthorhombic) α-U phase even in the pure uranium specimens (0 at.% Mo). α-U reflections decrease with increasing Mo content, while the reflections of γ-U increase visibly. Moreover, all the γ-reflections appear as single and sharp peaks, except of the reflection at 35.8^o (with an overlap of the α(021)+γ(110) peak). We notice here that the well-separated α(021) and γ(110) peaks were observed for water-quenched $U_{0.94}Mo_{0.06}$ alloy (6 at.% Mo) [82]. The appearance of the γ phase in U-Mo alloys with Mo content ≤ 10% is not very surprising, since the double (α+γ) phase was already found to exist in U-Mo alloys with 3.3-3.5 at.% Mo [56,83].

2) Further increase of Mo content leads to the formation of the γ^o phase in 11 and 12 at.% Mo, while the pure cubic γ-phase was observed for 13-15 at.% Mo. For all these alloys, the recorded diffraction peaks can be attributed exclusively to γ-type reflections, i.e. without any (orthorhombic) α-phase. In particular the intense peak at 35.8° became narrower, indicating that it contains mostly the γ(110) reflection. For U-11 at.% Mo and U-12 at.% Mo, a splitting of the γ reflection into a doublet with unequal intensity was observed for all γ-peaks (see Fig. 6.1, right panel), indicating that these alloys have actually the designated γ^o-phase [53]. The XRD pattern with single sharp γ-peaks for U-13 at.% Mo and U-15 at.% Mo alloys corresponding to "fundamental" A2 (cubic) structure reflections. Reliable lattice parameters could be obtained for the γ-phase alloys (see Table 1). Alloys with dominant α-component do not give reliable refinement due to the overlap of the diffraction peaks.

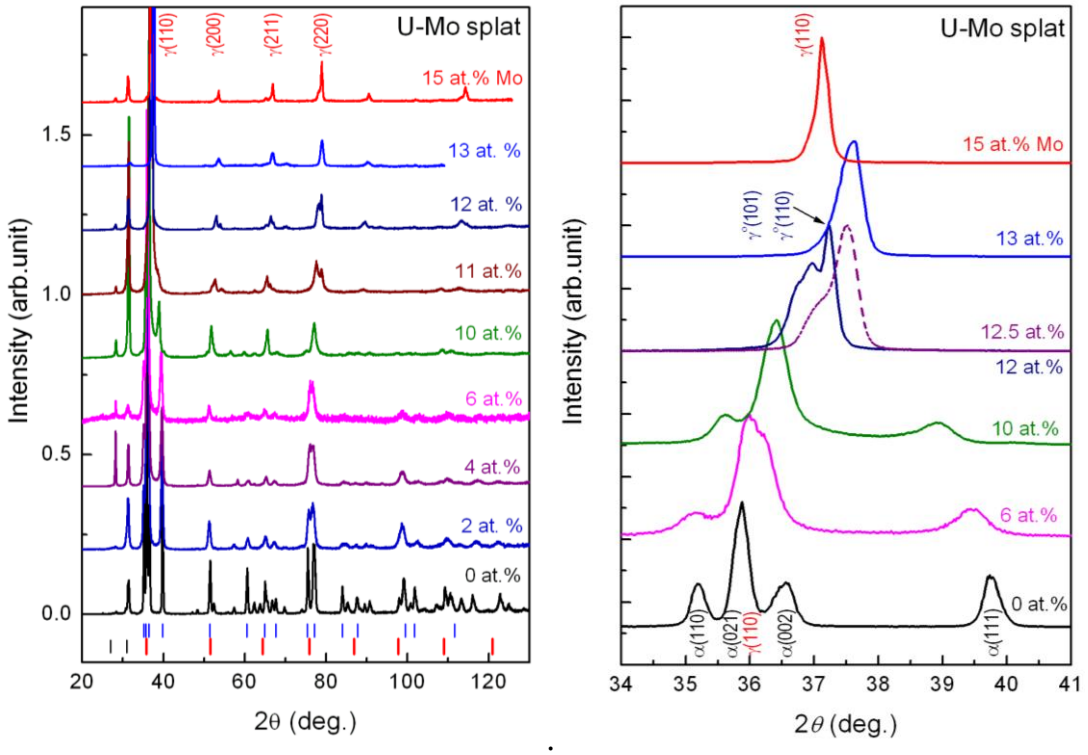

Figure 6.1. (left panel) X-ray diffraction patterns of U-Mo splats for various Mo concentrations. Each curve was normalized to the intensity of the most intense peak at $2\theta = 36^o - 37^o$ and then shifted upwards. The (colour) vertical ticks indicate the main XRD lines of orthorhombic α-U (blue) and cubic γ-U (red) structures. The two leading peaks at low angles belong to surface impurities (black ticks). The indices of

four main γ-U reflections are given at the top. The low-angle X-ray reflections of selected U-Mo alloys (right panel) further illustrates the phase transformation from the double (α + γ) phase for alloys with 1 - 10 at.% Mo (coexisting of α and γ reflections) to γ^o phase for alloys with 11-12.5 at.% Mo (splitting of the γ-reflections into doublets) and pure cubic γ phase for alloys with ≥ 13 at.% Mo (single γ-reflections).

3) The calculated lattice parameters (Tab.1) determined for the γ^o/γ phase detected in the splat-cooled U-Mo alloys, especially the values for the *c*/*a* ratio for the γ^o-phase alloys (0.98-0.99), are in a good agreement with those reported earlier [83]. At low angles, peaks corresponding to UO_2 and UC were observed irrespective of composition, originating mostly from the surface of the splats (as they are suppressed by scraping/polishing).

We have been primarily interested in how low one can get the Mo concentration without any admixture of the α-phase and where γ^o and pure γ is obtained. One can see that 100% pure cubic γ-phase was obtained for U-13 at.% Mo. Although the observed γ-peaks are not as sharp as those for U-15 at.% Mo, however, they are not split (i.e. all are single peaks). Single-peak character was also observed in U-12.5 at.% Mo for all high-angle γ-reflections. Although no visible splitting of the γ(110) reflection was observed, a trace of doublet-type was still present (see Fig. 6.1, right) revealing that the $\gamma^o \rightarrow \gamma$ transformation in U-12.5 at.% Mo alloy was still not complete.

For a clear view of the phase development in splat-cooled U-Mo alloys, the low-angle XRD patterns of selected U-Mo alloys are shown in Fig. 6.1, right panel. The XRD patterns obtained for samples with 0 – 10 at.% Mo are very similar, except of the fact that with Mo doping (≥ 1at.%) the α(002) peak was merged to the overlapped α(021)+γ(110) peak forming a very diffuse peak at 36^o. With increasing Mo concentration, the intensity of α-U peaks largely decreases. Besides, whilst alloys with Mo concentration up to 6 at.% exhibited almost no shift of the α-peaks, a significant shift of these peaks was observed with further increasing of the Mo concentration up to 10 at.%. This was ascribed to a large contraction in the *b*-parameter of the regular orthorhombic structure, resulting in what is traditionally referred to as the α_b'-phase [53]. In other words, these intermediate Mo-concentrations (6-10 at.% Mo) consist of the mixed (α_b' + γ) phase. The so-called α_b''

monoclinic phase (indicated by a splitting of the α-uranium peaks into two components), previously observed in water-quenched alloys with 7.2-11.18 at.% Mo [54], is not observed in our case. However, the monoclinic distortion cannot be completely ruled out, since a line broadening was revealed for all α-reflections. As we mentioned above, for U-11 at.% Mo and U-12 at.% Mo, the splitting of the γ-reflection into a doublet was observed for all γ-peaks. As an example, it was shown in Fig. 6.1 (right panel) that the γ(110) reflection of U-12 at.% Mo splits into a doublet located around 37.0^o (γ^o(101)) and 37.2^o (γ^o(110)). In U-12.5 at.% Mo, although the γ^o(101) reflection disappeared, a shoulder-like feature was observed indicating that such an alloy still consists of a mixed γ^o +γ (dominant) phase. Increasing Mo content to 13 at.%, all γ-reflections exhibit as single-type peaks, e.g. the γ(110) reflection at 37.6^o, revealing that it consists of 100% pure cubic γ-phase. However, all these peaks are diffuse, considered to be corresponding to superlattice reflections caused by the atom shifts (from their ideal A2 sites). Increasing the Mo concentration to 15 at.%, the γ-peaks become very sharp, e.g. the γ(110) reflection located at 37.1^o (Fig. 6.1 right panel), revealing that they are corresponding to the fundamental A2 structure reflections.

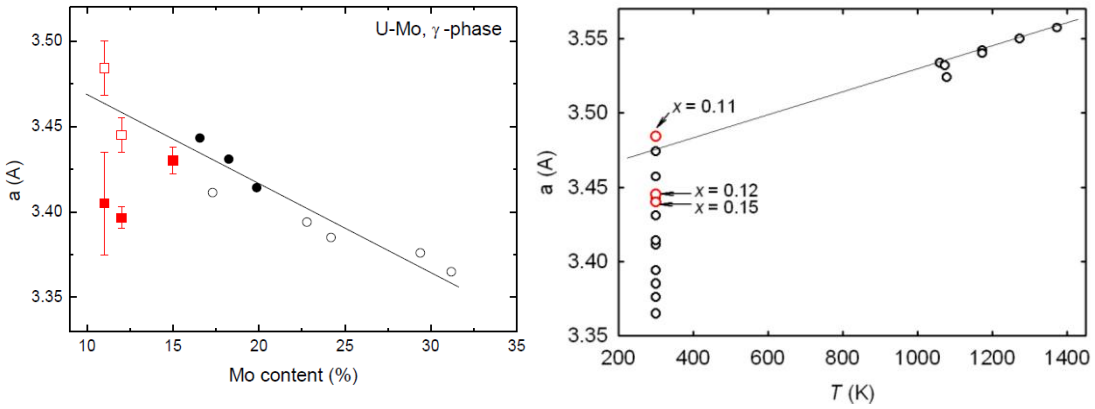

Figure 6.2. (left) Lattice parameters of the U-Mo alloys with γ-structure as a function of Mo content ($a = b$: open squares; c: solid squares). The alloy with 15 at.% Mo is with the cubic structure ($a = b = c$). The data for a high Mo content taken from XRD database (open circles) and Ref. 2 (solid circles) were shown for a comparison. The straight line is a guide for the eyes. (right) Lattice parameters of the U-Mo alloys in comparison with XRD database data for γ-U at various temperatures (at which γ-U is thermodynamically stable). Extrapolation of this data to 300 K is shown by line.

The calculated lattice parameters (*a*, *b*, *c*) determined for the γ^o and γ phase detected in the splat-cooled U-Mo alloys as a function of Mo concentration are shown in fig. 6.2 (left). As mentioned above, the structure with tetragonal distortion ($a = b \neq c$) is observed for alloys with 11– 12 at.% Mo, while the cubic structure ($a = b = c$) was found for the alloy with 15 at.% Mo. For a comparison, the data for high Mo concentrations in earlier reports (e.g. [36]) are also shown in fig. 6.2 (left). Our data for the *a*-parameter are in a good agreement with the linear fit of the lattice parameter dependence on the Mo content. Also it is in good agreement with extrapolation of high temperature data of pure γ-U to 300K (3.474 Å), which is shown on fig.6.2 (right). Crystal lattice is shrinking with Mo concentration as Mo has a lower atomic radius than U.

Our values for the three alloys are given in Table 1. We should mention, that the shortest inter-uranium distance for γ and γ^o-phase U-Mo splat samples is 3.0 Å, which is far below the Hill limit (3.4 – 3.6 Å). That predicts possible superconductivity in U-Mo γ-phase alloys.

Mo concentration. *x*	*a* = *b* (Å)	*c* (Å)
0.11	3.484	3.404
0.12	3.445	3.396
0.15	3.440	3.440 (*a*=*c*)

Table 1. Lattice parameters for γ^o / γ splat samples with different Mo concentration: 11, 12 and 15 at.% Mo.

EBSD analysis was so far performed on the pure-U and U-15 at.% Mo alloy. For both splat samples, crystallographic and phase mapping were performed on surface and sectional cuts through the alloy. The EBSD maps recorded from the cross-sections revealed an unusual microstructure of the splat-cooled pure uranium (fig.6.3, top), which exhibits a range of distorted grains shapes and intra-granular twinning. Grain sizes were typically large, with the modal average being 24.6 μm diameter, and exhibited a preference for a (101) orientation. A significant number of twins were observed. The most abundant were narrow 69^o misorientations ({130} twins), although there were a number of much wider 90^o misorientations ({172} twins).

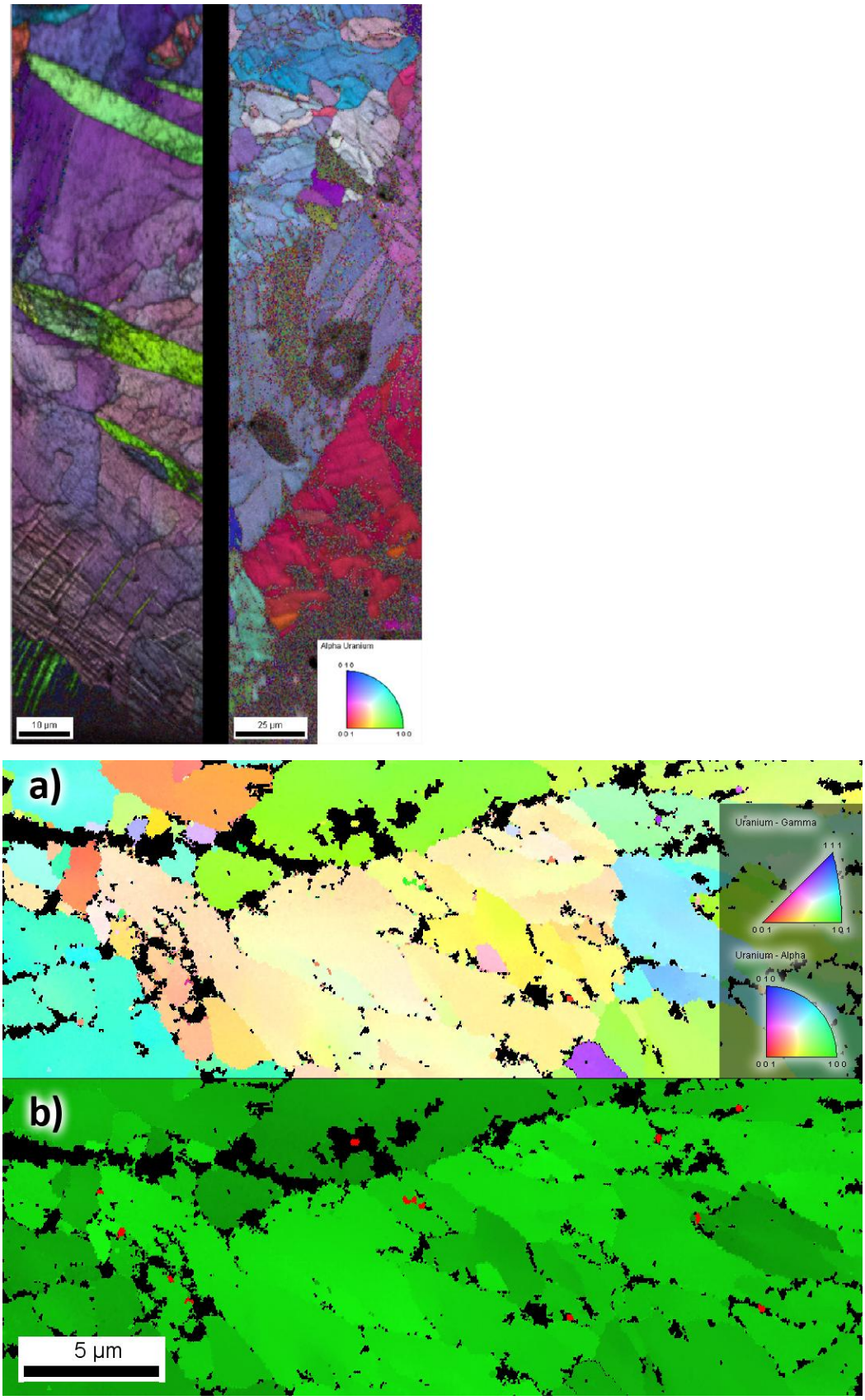

Figure 6.3. (top) Two EBSD crystallographic orientation maps highlighting the cross-sectional microstructure of the pure U splat. The section maps determined only

α-U, with numerous incidences of crystal twinning and low angle sub-boundaries. The grains are color coded relative to the inverse pole figure plot in order to represent their relative crystallographic orientations. (bottom) EBSD maps recorded from the pure U splat surface showing a) crystallographic orientation and b) phase distribution. The metal is predominantly α-U (green) with small and well dispersed γ-U (red) grains.

No γ-phase was detected with confidence throughout the cross-section (i.e. sectional cuts through the U-sample performed at arbitrary chosen points), only α-U was recognized in the bulk U-specimen. Despite the distorted structure observed throughout the splat, no evidence for dendritic growth was observed, unlike many other splat cooled metals. For the U-15 at.% Mo alloy, the data clearly indicated the presence of a γ-U phase structure with no detectable α-U (in the bulk of U-15 at.% Mo alloy).

The EBSD crystallographic and phase mapping of the ion-sputtered regions of the surface of the pure U splat is shown in fig. 6.3 (bottom). It indicates with good confidence a predominantly α-U structure with rare, few small isolated grains of γ-U, typically no more than 1 μm in maximum dimension. As the surfaces of the splat would be subject to the most rapid cooling, it is also the region where the γ-phase is most likely to be preserved, while such a phase did not exist in the bulk of the sample (i.e. no γ-phase was detected throughout the cross-section mentioned above). The γ-phase observed using EBSD were both intra-granular micrograins (typically sitting along sub-boundaries) and inter-granular micrograins. Although the EBSD confirmed the XRD results for the existence of γ-phase, the scarcity of grains in the EBSD images does not correlate well with the intensity of the peaks in the XRD data. Namely, a smaller amount of γ-phase was revealed by the EBSD mapping. We assume that the electropolishing used to prepare the sample for EBSD have removed a sizable volume of the sample-surface and thus it is possible that quantities of γ-phase (mostly concentrated on the surface (in a thickness in the range up to hundreds nanometers) were removed at that point.

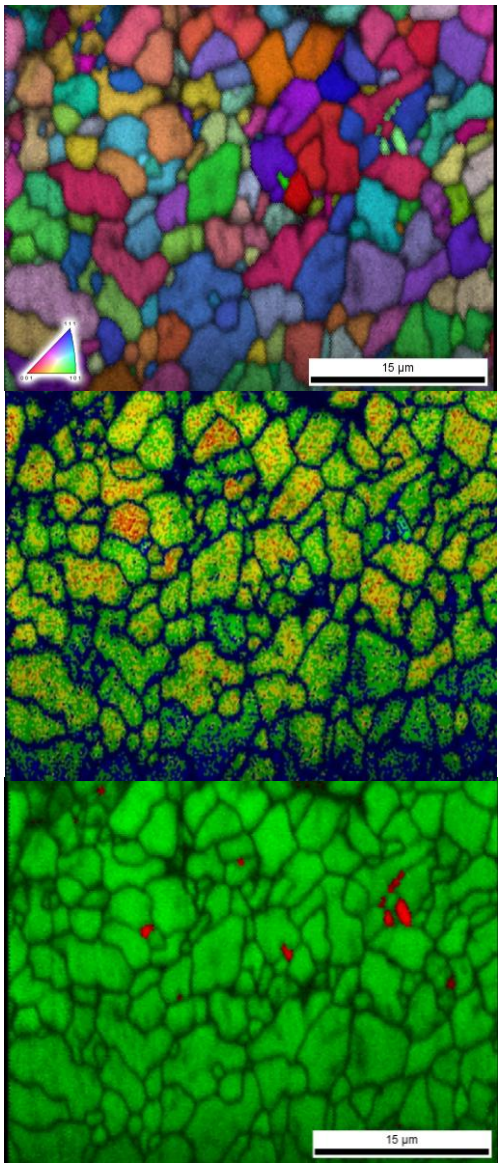

Figure 6.4. EBSD (top) crystallographic orientation and (bottom) phase distribution maps highlighting the surface microstructure of the splat-cooled U-15 at.% Mo alloy. The confidence index map (middle) was also shown. EBSD mapping identified only γ-U phase and UC with no evidence for α or α-related phases.

The EBSD maps recorded the surface microstructure of splat-cooled U-15 at.% Mo alloy were displayed in fig. 6.4, highlighting an equigranular grain structure, without crystal twinning and without preferred crystallographic orientation. EBSD mapping identified only γ-U phase, with no evidence for α or α-related phases, but with some isolated monocarbide (UC) inclusion particles (shown by the red spots in Fig. 6.4 (bottom)).

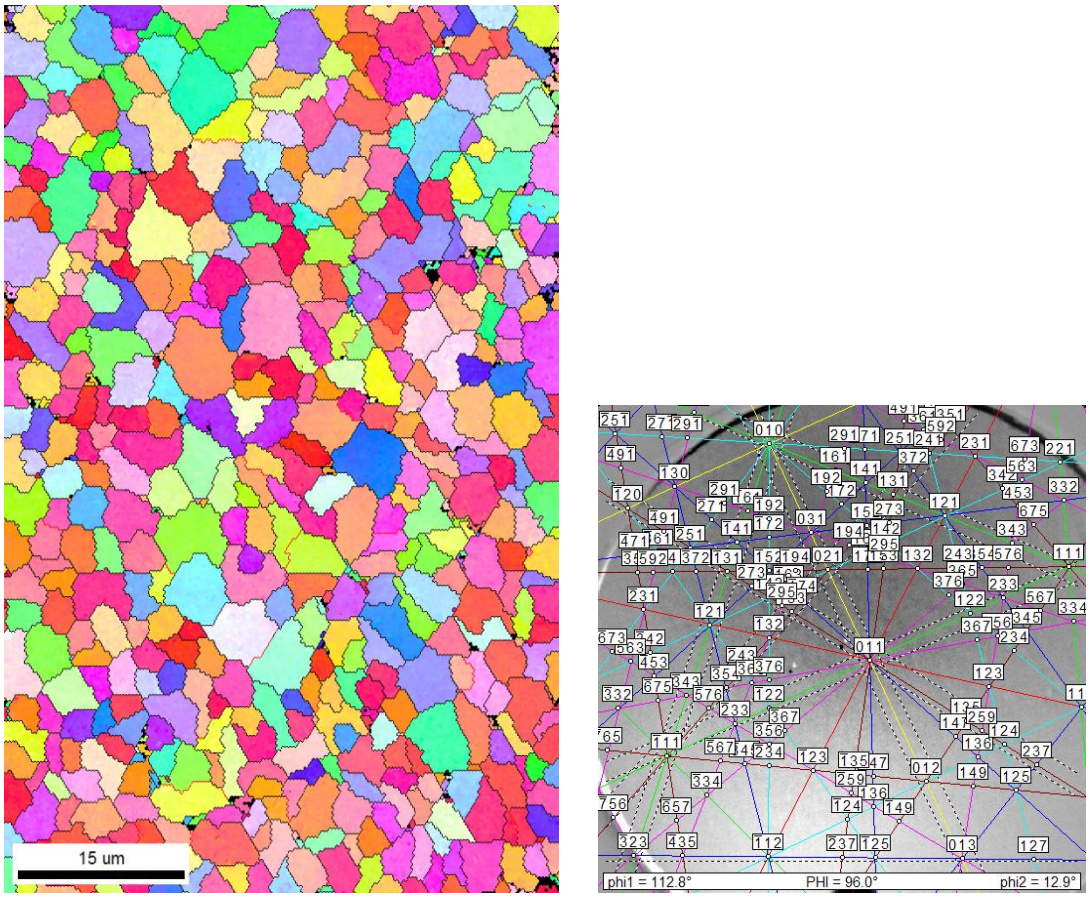

Figure 6.5. EBSD crystallographic orientation map (left) highlighting the surface microstructure of the splat-cooled U-12 at.% Mo alloy. EBSD mapping identified only γ-U phase and UC (small black areas) with no evidence for α or α-related phases. Small black areas identified to be UC, which was confirmed by EBSD (showed by Kikuchi lines) (right).

The EBSD map recorded from the surface of splat-cooled U-12 at.% Mo alloy is presented in fig. 6.5. The EBSD highlighting an equigranular grain structure, without crystal twinning and without preferred crystallographic orientation was observed. The grain size is similar to ones for U-15 at.% Mo splat. Our equipment cannot resolve such small deviation of structures as small tetragonal distortion of γ-U phase (γ°-phase). That is why the structure was identified from EBSD measurement just as a normal γ-phase. EBSD mapping identified only γ-type phase (from XRD investigation we know that it is γ°-phase), with no evidence for α or α-related phases. Some isolated areas (see black areas in fig.6.5) identified to be UC, which was confirmed by EBSD (right).

The crystal structure appears to be finer than that of the pure U splat (modal average diameter of 3.1 μm, with over 60% of grains between 3.1-5.2 μm), and shows less signs of distortion. We notice here that one EBSD map indicated that there was a possibility of grain size varying significantly across a cross-section of the sample.

The structure stability tests have been performed in order to see how stable our splat samples are. The XRD measurements were performed on the splat-cooled pure U specimen kept in atmospheric conditions after 1, 3, 6 and 12 months. Except of a small change in the relative peak-intensity, no visible change was observed. Especially all the γ-peaks are well preserved. Our results indicate that both α- and γ-phase formed in the splat-cooled U-specimen have a long-term stability at ambient conditions.

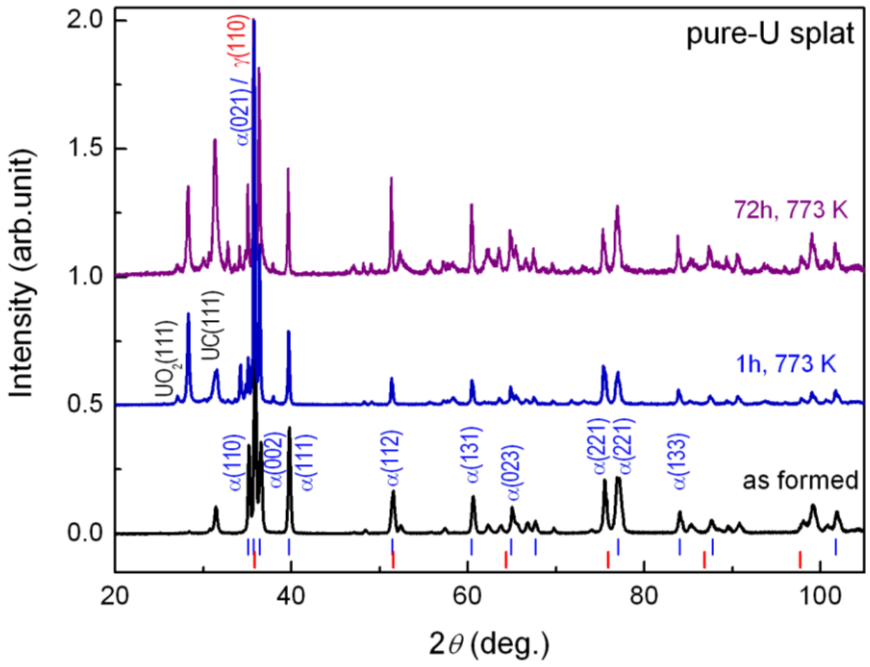

Figure 6.6. Comparison of XRD pattern of the pure-U splat in the as-formed state with those upon annealing at T = 773 K (500 ^{o}C) for different time. (The curves were normalized and shifted for clarity). The vertical ticks indicate the main peak positions for the (blue) orthorhombic and (red) cubic structures. The four main cubic γ-phase reflections are labelled.

No change in the XRD patterns of the pure U-splat was revealed upon annealing at T = 773 K (500 ^{o}C) up to annealing time of 144 h, except of some small

changes in the relative peak intensity. Fig. 6.6 shows the comparison of XRD pattern of the pure-U splat in the as-formed state with those upon annealing at 773 K for various annealing time. Each curve was normalized to the maximal intensity of the most intense peak at $2\theta = 36^{o} - 37^{o}$. The curves were then vertically shifted for clarity. Fig. 6.6 also contains the vertical lines at the bottom indicating the main XRD lines of the orthorhombic and cubic structures. Increasing annealing time mostly implies a larger sample contamination showed by a large increase of the peak-intensity related to oxides and carbides. Moreover, the background signal increases enormously after 72 h. Increasing annealing time to 144 h leads to a strong increase of the UC (111) peak and an appearance of high-angle UC/UO_2 peaks.

Similar to pure U splat, all U-Mo alloys are very stable to exposure to atmospheric conditions; no visible change in XRD pattern was observed after e.g. one year in air.

Fig. 6.7 shows a comparison of XRD pattern of the splat-cooled U-12 at.% Mo alloy in the as-formed state with those upon annealing at T = 773 K (500 ^{o}C) and 1073 K (800 ^{o}C) for various annealing time. Upon annealing at T = 773 K, the α(021) reflection appeared after annealing for 4 h (fig. 6.7 left). With further increasing annealing time (10 h), more and more α-U reflections appeared. Besides, they are gradually more intense. After 72 h, the two main α-reflections, α(021) and α(002), are well separated from each other and have almost equal intensity. The double γ peak around 37^{o} (γ^{o}(110) and γ^{o}(101) peak of the γ^{o}-phase) merged into one broad and asymmetric peak upon annealing after 4 h, which then becomes more symmetric and shifted towards higher angles after 10 h. Upon further annealing such a peak was split into two separated peaks (fig. 6.7 left) assigned as γ'(110) and γ'(103) reflection of U_2Mo intermetallics. Moreover, high-angle γ' peaks were observed (at 53.6^{o}, 55.8^{o}, 79.2^{o}, 81.2^{o} respectively for γ'(220), γ'(213), γ'(200), γ'(206)).

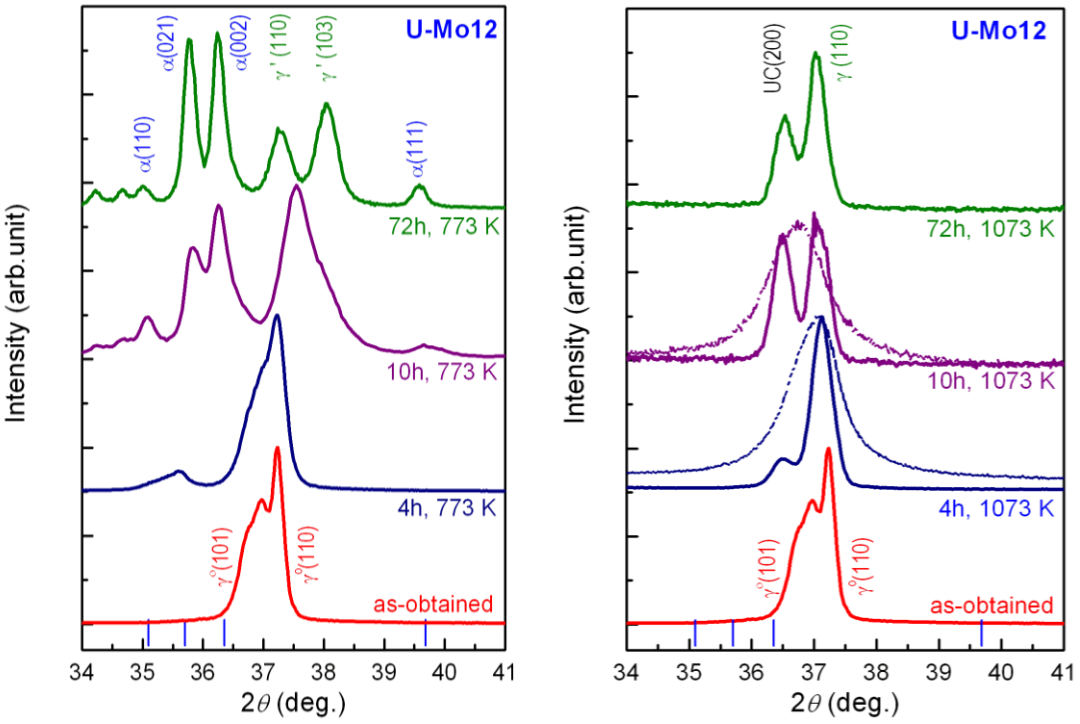

Figure 6.7. Comparison of (low-angle) XRD pattern of the U-12 at.% Mo splat (U-Mo12) in the as-formed state (γ^o-phase) with those upon annealing at 773 K (left) and 1073 K (right) for different annealing time. The (blue) vertical ticks indicate the main reflections of the orthorhombic structures. Solid lines show the results obtained on samples just after annealing, while those after sample scraping to remove partially surface contaminations (e.g. carbide) indicated by dashed lines.

The results confirmed that annealing at T = 773 K leads to a decomposition of the initial γ^o-phase and $\gamma^o \rightarrow \gamma'$ transformation, yielding a composite ($\alpha + \gamma'$) structure in U-12 at.% Mo alloy. We notice here that the α-phase reflections did not appear until 3 h annealing (at the same temperature 773 K) for U-9 at.% Mo alloy [56] (which had undergone additional sample treatments and exhibited the pure γ phase before annealing). In our case, the α-reflections are located at the expected reflection angles of the α-U phase, indicating that the α-phase formed due to the γ decomposition does not show any significant change in the lattice parameters. A small but visible peak-shift to higher reflection angles, however, was observed for the $\gamma^o \rightarrow \gamma'$ transformation. No peaks associated with the decomposition of the γ^o-phase were found upon annealing at T = 1073 K (800 ^{o}C) for different annealing times up to 144 h (fig. 6.7, right panel). The double γ^o-peak (i.e. γ^o(101) and γ^o(110)

located respectively at 36.9^o and 37.2^o in the as-formed state) has changed into a single broad peak located at 37.2^o after annealing of 1 h. Increasing the annealing time to 4 h implies an appearance of a satellite peak at 36.5^o, which became enhanced with increasing annealing time. We notice here that, unlike annealing at T = 773 K, no peak shift and no peak-splitting was observed for all γ-reflections upon annealing at T = 1073 K up to 72 h, e.g. the γ(110) reflection is always located at around 37.2^o. Besides, no peak appeared at 37.9^o, i.e. at expected position of the γ'(103) reflection. Thus we assumed that annealing at 1073 K leads to the $\gamma^o \rightarrow \gamma$ transformation and stabilization of such γ phase, which does not have to be accompanied by any change in the lattice (or any change in the Mo concentration).

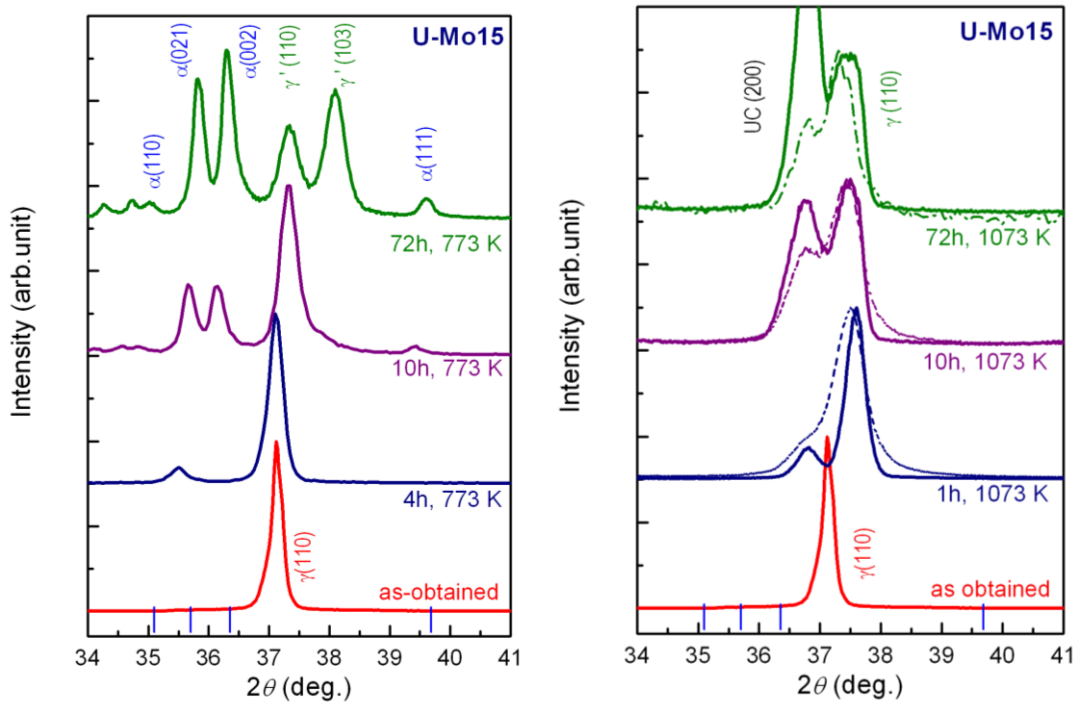

Figure 6.8. Comparison of (low-angle) XRD pattern of the U-15 at.% Mo splat (U-Mo15) in the as-obtained state (pure cubic γ-phase) with those upon annealing at 773 K (left) and 1073 K (right) for different annealing time. The (blue) vertical ticks indicate the main reflections of the orthorhombic structures (α-U). Solid lines show the results obtained on samples just after annealing, while those after sample scraping to remove partially surface contaminations (e.g. carbide) indicated by dashed lines.

The additional peak at 36.5^o was attributed to UC(200) present as a surface contamination. It is visible that increasing annealing time leads to the appearance of more UC as well as UO_2 reflections with a higher intensity, indicating obviously that increasing annealing time leads to an enhanced surface contamination. In order to confirm it, we have performed the XRD on the annealed sample after scraping the surface (i.e. removing the surface contamination). The comparison of data obtained on annealed samples at T = 1073 K before and after scraping was presented in fig. 6.8 right panel. The scraping produces a large reduction of UC peaks. For instance the (relative) intensity of UC(111) reduced by 50% after scraping. A large reduction of the peak at 36.5^o was also observed confirming that it is originated from UC(200). The scraping can influence also the microstructure of the splat surface, evidenced by a large broadening of the γ(110) peak. In the case of annealing at 773 K, the intensity of α(002) reflection is strongly enhanced. Namely, for the as-formed splats with mixed phases, the α(021) reflection (at 35.4^o) was the most intense one, while for the splats consisting of α-phase from the γ-decomposition, the peak at around 36.5^o turned out to be the most intense one. Since the UC(200) peak is very close to the α(002) one, we assumed that the intense peak at 36.5^o was as a result of overlapping of the α(002) and UC(200) ones (at 36.4^o and 36.5^o, respectively).

A similar change was observed for U-15 at.% Mo upon annealing at T = 773 K, shown in fig. 6.8 (left panel). Namely, annealing leads to a partial decomposition of the γ-phase to form the equilibrium α-phase and the intermetallic compound U_2Mo (revealed by the appearance of the γ'(110) and γ'(103) reflections). The pure cubic γ-phase in the as-formed state shows up as sharp γ peaks. Annealing at T = 773 K only leads to a small broadening of the γ reflections. Similar to U-12 at.% Mo alloy, a shift towards higher angles was also observed in this case, indicating a small change in the lattice parameter related to γ → γ' phase transformation. During the ordering process the larger uranium atoms become closer together. The smaller molybdenum atoms after ordering are surrounded by atoms at a slightly larger distance than that in the disordered state. The γ-phase was well stabilized upon annealing at T = 1073 K (fig. 6.8 right panel). The γ(110) peak was shifted visibly towards the higher angles after annealing of 4 h. No further peak-shift was observed with increasing annealing time (≥10 h). However, a large peak-broadening of e.g. γ(110) peak was revealed. The peak broadening for U-15 at.% Mo alloy is even more enhanced than that for U-

12 at.% Mo alloy. It indicates that the cubic phase has a quite inhomogeneous molybdenum distribution. The additional peak at around 36.5° was attributed to UC(200) due to its specific behaviour (e.g. its intensity was much enhanced with increasing annealing time and it was much suppressed after scraping the sample surface). More peaks attributed to UC and UO_2 were observed at high angles for longer annealing time, revealing more surface contamination upon annealing at T = 1073 K (in comparison with that at 773 K). In this case, annealing at 1073 K leads to a stability of the cubic γ-phase without γ → γ' (disordered-ordered) phase transformation. Not only the γ(110) peak but all other γ-peaks are diffuse, indicating an inhomogeneous Mo distribution in the sample.

We started the investigation of electronic properties of U-Mo samples from the measurements of electrical resistivity (3-300 K) .The temperature dependence of the electrical resistivity of U-Mo splats is shown in fig. 6.9 in comparison with the resistivity of the pure U metal (bulk U) from the same batch, which was used as a precursor for the splats production.

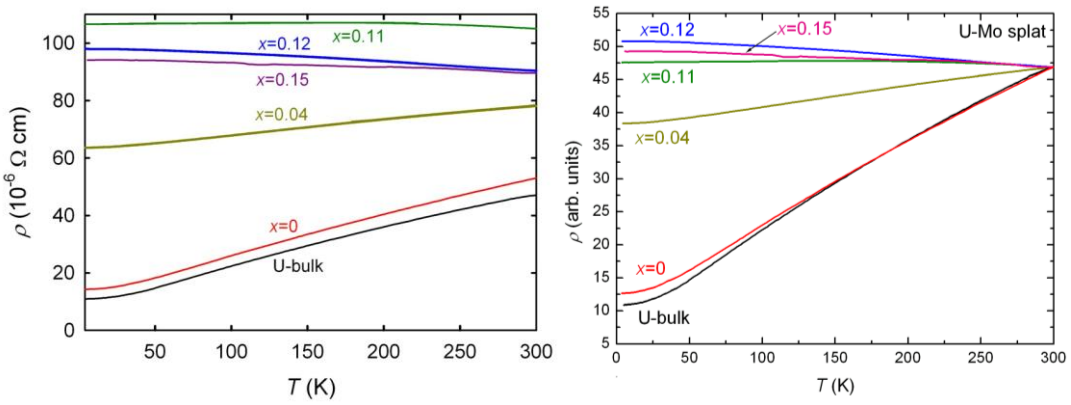

Figure 6.9. Temperature dependence of electrical resistivity $\rho(T)$ for U-Mo splats with various Mo concentrations compared with bulk uranium data. Data are presented in absolute values (left panel) and normalized to the value $\rho_{300\ K}$ (right panel).

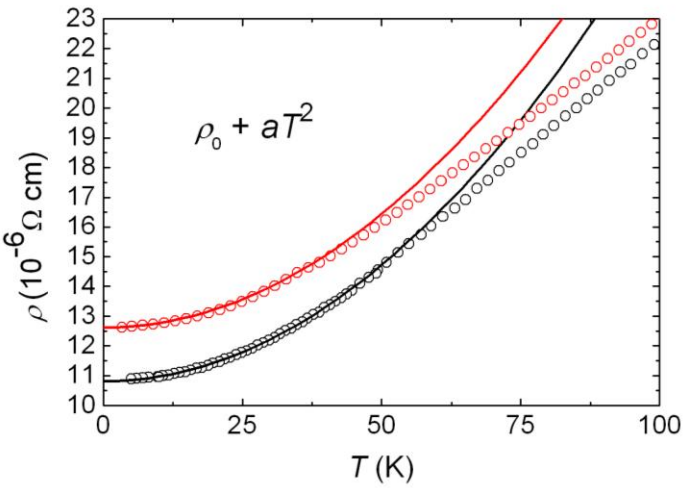

Figure 6.10. Low-temperature part of temperature dependence of electrical resistivity for pure U splat (red symbols) and pure U bulk (black symbols). The data were tentatively approximated by the ρ_0+aT^2 type of dependence, shown by the full lines.

The bulk U sample exhibits typical temperature dependence with weakly negative $d^2\rho/dT^2$. Anomalies related to charge density wave transition, which manifest for single crystal U [23,84], were not observed in bulk U. The residual resistivity ρ_0 value increases from 10 μΩcm for bulk U to 14 μΩcm for pure-U splat sample, and this increment remains almost constant for the whole temperature range, which can be attributed to the higher amount of defects in the crystal lattice of the splat sample. Resistivity increases smoothly with increasing T from 3 to 300 K and below 50 K $\rho(T)$ follows a quadratic dependence, which reflects the electron–electron scattering (see fig. 6.10): $\rho = \rho_0+aT^2$. The values of a = 15.4·10^{-4} μΩcm/K^2 and a = 16.3·10^{-4} μΩcm/K^2 were estimated, respectively, for the pure bulk- and splat-cooled U samples. The Kadowaki-Woods ratio is the ratio $R_{KW} = a/\gamma_e^2$, where a is quadratic term of the resistivity and γ_e is Sommerfeld coefficient [85]. R_{KW} for U and other correlated systems should be equal to approx. 1·10^{-5} μΩcm·(mol·K/mJ)^2. For pure U splat sample this ratio gives the value approximately 1.3·10^{-5} μΩcm·(mol·K/mJ)^2 which is consistent with the Kadowaki-Woods rule.

The alloys corresponding to the pure γ^o or γ–phase have the resistivity much higher (Table 2) and exhibit dramatically different temperature dependence. Instead of the decrease of ρ with decreasing T, common in metals, we observed a weak but systematic increase and saturation in the low-T limit. The highest relative increase,

8%, between 300 K and 3 K was found for 12 at.% Mo. The resistivity curves are similar to those recorded for high Mo concentration alloys mentioned in Ref. 28. Such type of behavior was originally attributed to a strongly dependent density of states at the Fermi level, compensating for the standard electron-phonon scattering effect, leading normally to the positive $d\rho/dT$. Nowadays there is lot of evidence associating such behavior with strong disorder, observed for example in some amorphous systems and Heusler alloys [86,87]. We suggest that in our case the statistically distributed Mo atoms lead to a large disorder effect. Additional disorder can be induced by ultrafast cooling. Maximum resistivity value is reached for the sample with 11 % Mo. The mechanism behind negative $d\rho/dT$ can be seen in weak localization [31], i.e. a quantum effect appearing when the wavelength of conduction electron is comparable with the spacing between scattering centers. It appears under conditions of strong disorder (electron is scattered at almost every atom), and is partly suppressed by electron-phonon scattering at elevated T, which disturbs the quantum coherence. It is believed to give explanation for the Mooij criterion, relating the appearance of the negative slope to enhanced residual resistivity ρ_0 [32]. The intermediate concentrations (see e.g. 4% Mo splat in fig.6.9) exhibit resistivity behavior clearly consisting of both components, with positive $d\rho/dT$ but $\rho(T)$ much more flat than in α-U.

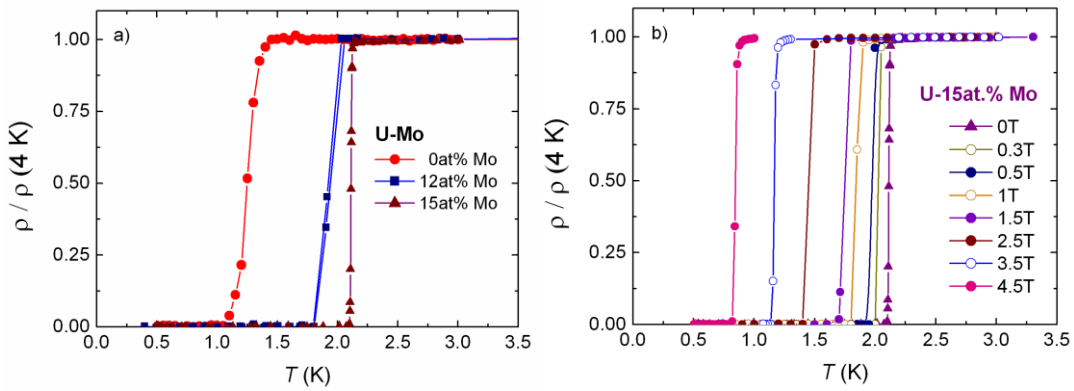

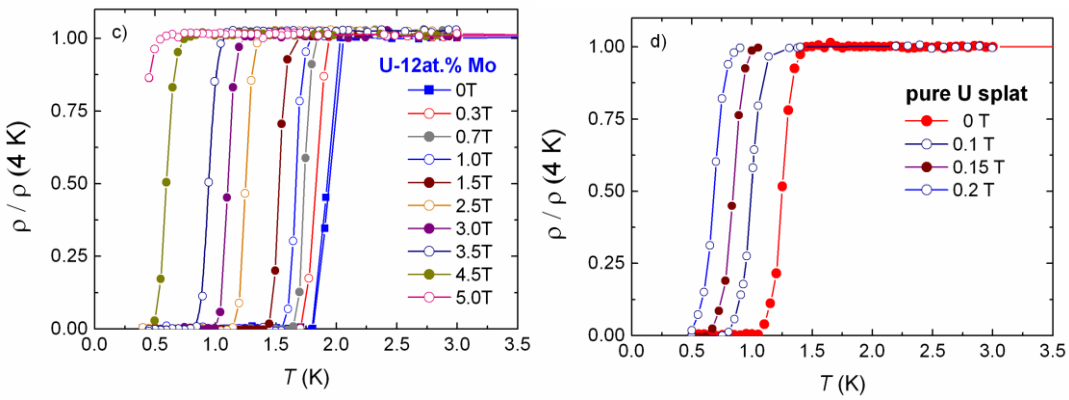

Figure 6.11. Low-temperature resistivity of U-Mo alloys (with 0, 12 and 15 at.% Mo) prepared by splat-cooling: (a) comparison of the resistivity in zero field, (b-d) the results in applied magnetic fields. The curves were normalized to respective resistivity values at T = 4 K.

In order to observe superconducting transitions, resistivity was measured also in the low temperature range (down to 0.4 K; see fig. 6.11). All curves were normalized to the resistivity value at T = 4 K. We found that all the samples studied become superconducting with the critical temperature decreasing with decreasing Mo concentration (T_c = 2.11 K, 1.91 K, and 1.24 K for 15 at.% Mo, 12%, and 0%, respectively). The maximum value well correlates with that of Chandrasekhar and Hulm [28], who reported that T_c decreases again with more Mo doping. The superconducting phase transition seen in resistivity is abrupt, especially for the 15 at.% Mo sample. The width of the superconducting transition in resistivity transition, defined as $\Delta T = T(\rho_{90\%})-T(\rho_{10\%})$, can be estimated as 0.01 K for this splat.

Mo conc. x	ρ_{300K} (μΩcm)	T_c (K)	$-\mu_0(dH_c/dT)_{Tc}$ (T/K)	$\mu_0 H_{c2}(0)$ WHH (T)	$\mu_0 H_{c2}(0)$ (T)	γ_e (mJ/mol K^2)	Θ_D (K)
0	53	1.24	0.35	0.30	0.30	11.0	179
0.03		0.65					
0.06		0.7	2.6	1.3			
0.11	105	1.25	3.8	3.3	4.9	13.0	147
0.12	90	1.91	3.9	5.2	6.0	15.8	139
0.15	89	2.11	3.6	5.3	6.7	16.0	139

Table 2. Summary of measured electronic properties for U-Mo splat-cooled alloys.

Applying external magnetic field, the superconducting transitions shift towards lower temperatures as expected, and eventually the superconductivity is suppressed entirely (fig. 6.11). For pure-U splat, the superconductivity is suppressed relatively fast. On the other hand, the γ-U type splats (12% and 15% Mo) exhibit much higher field resistance. The results are summarized in fig.6.12, which gives an idea that the α-U and γ-U superconductivity are qualitatively different, despite the fact that T_c does not differ substantially. To quantify the difference, we determined the critical slope at T_c, $-\mu_0(dH_{c2}/dT)_{Tc}$. The values are given in Table 2.

The upper critical field of classical superconductors with weak electron-phonon coupling is given by the Werthamer-Helfand-Hohenberg (WHH) theory, which predicts, assuming an orbital pair breaking, a universal function H_c vs. T, which is quadratic in T. It provides the $T \rightarrow 0$ limit value $H_{c2}(0) \approx 0.7 \cdot T_c \cdot (-dH_{c2}/dT)$ [8]. As the WHH theory is frequently violated for less conventional superconductors, we also parameterized the variations of H_{c2} in fig. 6.12 by a quadratic polynomial including a linear term, which can better account for more linear than the standard quadratic shape (observed e.g. in U_6Fe) [11]. The values do not come out very different for each alloy, so we can conclude that the upper critical field at $T = 0$ is in the range 5-7 T for the γ-U type of superconductivity, very different from 0.3 T found for α-U superconductivity. The high upper critical slope at T_c and correspondingly high upper critical field of the γ-U superconductivity correspond to materials as A15 superconductors with strong coupling, which have, however, the T_c values exceeding 10 K.

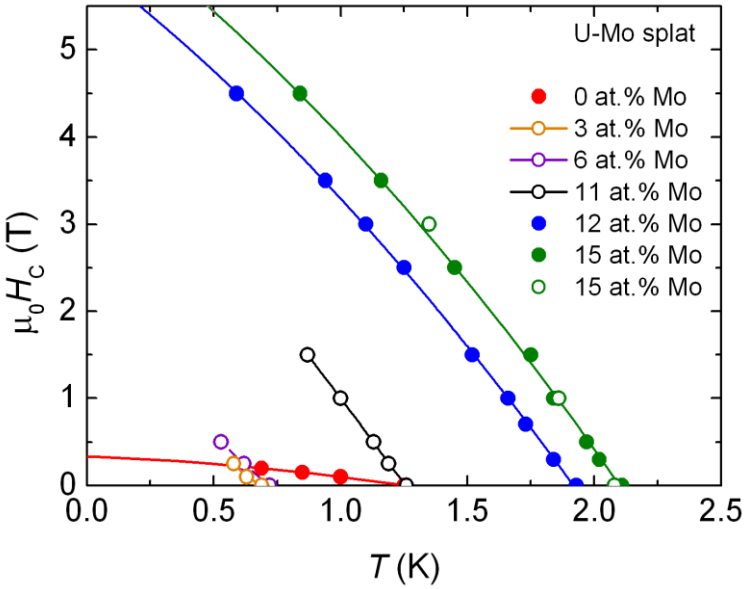

Figure 6.12. Critical magnetic field H_c vs temperature T for pure-U and U-Mo alloys prepared by splat cooling, as determined from electrical resistivity (full circles) and specific heat (empty circles). The fits by second-order polynomial function are shown by full lines.

The difference between the standard A15 superconductors and γ-U alloys is the disorder. It is interesting to point out that the A15 superconductors as Nb_3Ge, V_3Si have the T_c values much reduced by progressing disorder, increasing the resistivity to the values around 100 μΩcm [88]. The BCS theory predicts the value of critical slope $-dH_{c2}/dT$ to depend on normal-state parameters and on T_c in a way $-dH_{c2}/dT \sim T_c \cdot \gamma_e^2$, where γ_e is the Sommerfeld coefficient of electronic specific heat in the normal state [89]. Then, if all other microscopic parameters as the Fermi surface remained unchanged, the increase of T_c and γ_e (see the next section) between the α-U and γ-U phases would enhance $-dH_{c2}/dT$ by the factor of 3.6. The real enhancement is by the factor of 10-20.

The specific heat measurements was performed in the range of temperatures 4-300 K. Temperature dependence of the specific heat $C_p(T)$ exhibits no sign of CDW anomalies for pure U samples (bulk U and splat U) (fig. 6.13).

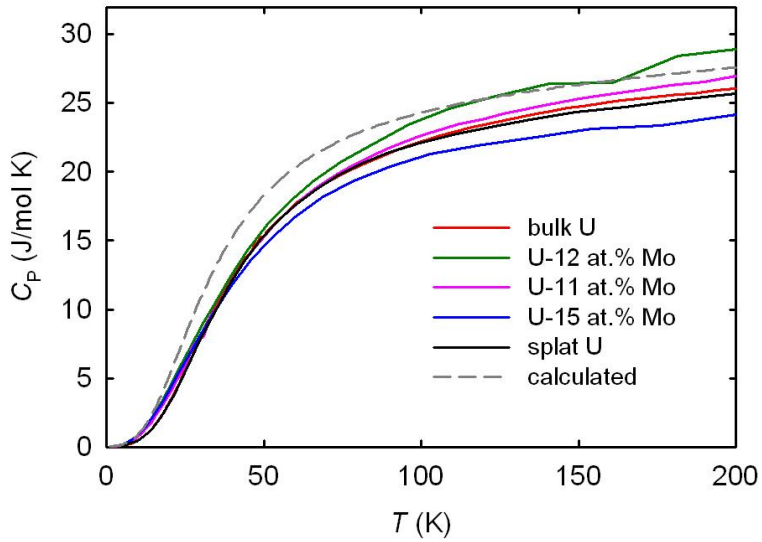

Figure 6.13. Temperature dependence of the specific heat of the selected U-Mo splats and bulk uranium sample. The dashed curve shows specific heat temperature dependence calculated by the Debye function (θ_D = 139 K) with addition of electronic contribution (γ_e = 16.0 mJ/mol K^2).

The temperature dependence of specific heat of the U-Mo splat samples shows a regular behavior. The linear low-temperature part (below 10 K but above respective T_c) in the C_p/T vs. T^2 representation (fig.6.14) was used to determine the Sommerfeld coefficient of electronic specific heat γ_e ($C_p/T = \gamma_e + \beta T^2$) and the Debye temperature θ_D ($\beta = 12\pi^4 R/5\theta_D^3$). The value γ_e = 11.0 mJ/mol K^2 is in a good agreement with the data obtained for the bulk sample using the same experimental setup (11.2 mJ/mol K^2), but slightly higher than that for uranium single crystal (9.13 mJ/mol K^2) [23]. The γ-phase splats are significantly different. For the splat U-15at.% Mo γ_e = 16.0 mJ/mol K^2 (i.e. 18.8 mJ/mol U K^2), which is a clear evidence of an increase of density of states at the Fermi level for γ-U. That can be ascribed to the increasing atomic volume and interatomic U-U spacing (affected additionally by the dilution of the U lattice by Mo atoms), and consequently a narrower 5*f*-band. It is interesting to realize that the enhancement is observed despite the atomic disorder, which may actually smear out the Density of States to some extent.

The specific heat temperature dependence, which was calculated (fig. 6.13, dashed curve) by the Debye function (θ_D = 139 K) with addition of electronic contribution (γ_e = 16.0 mJ/mol K^2), is in good agreement with measured data.

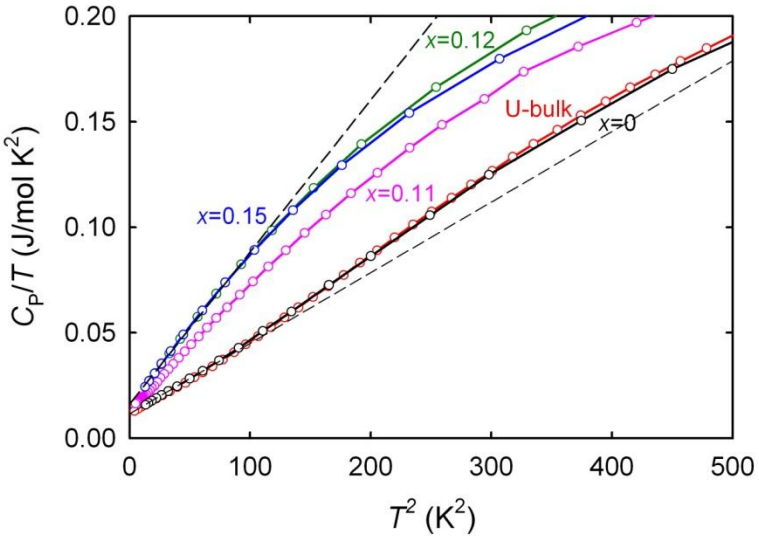

Figure 6.14. Temperature dependence of the specific heat of the selected U-Mo splats in the C_P/T vs. T^2 representation. The fits used to determine γ_e and θ_D are shown in two cases (dashed lines).

The Debye temperature θ_D = 139 K is reduced for γ-U samples, indicating a softening of the lattice, with respect to α-U, for which the same analysis provided θ_D = 179 K. The latter value is somewhat lower than the values given for bulk α-U in Ref. 23, which reviews values by different authors ranging from 183 K to 256 K. It is not clear whether the difference can be related to the character of the sample, being the splat-cooled material with very small admixture of γ-U in our case. A reader should be aware that the linear slope of C_p/T vs. T^2 scales with $1/\theta_D^3$; therefore the change of the slope between e.g. θ_D = 180 K and 220 K is much smaller than between 140 K and 180 K. The lattice softening between α-U and γ-U can be seen as parallel to similar but even larger effect between α-Pu (153 K) [90] and δ-Pu (103 K) [26]. The splat U-12 at.% Mo behaves similar, γ_e = 15.8 mJ/mol K^2 (corresponds to 17.7 mJ/mol U K^2).

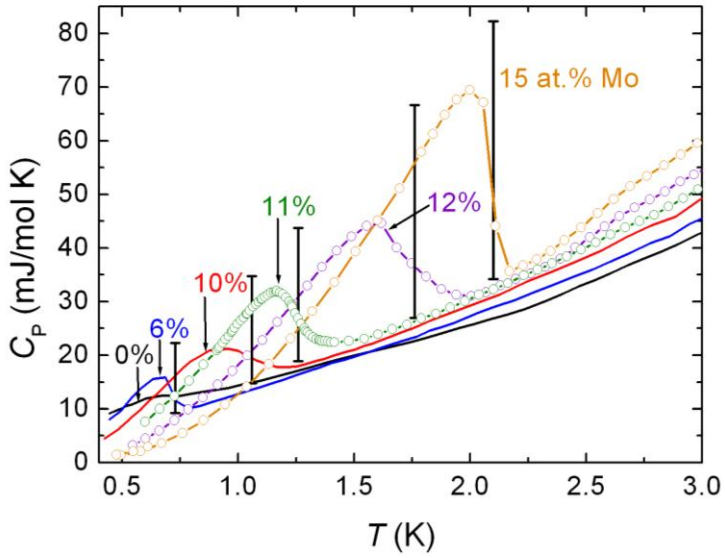

Figure 6.15. Superconducting transitions in U-Mo splats observed in the specific heat. The vertical bars indicate the theoretical BCS values ($1.43 \cdot \gamma_e \cdot T_c$) calculated using the experimental Sommerfeld coefficients γ_e.

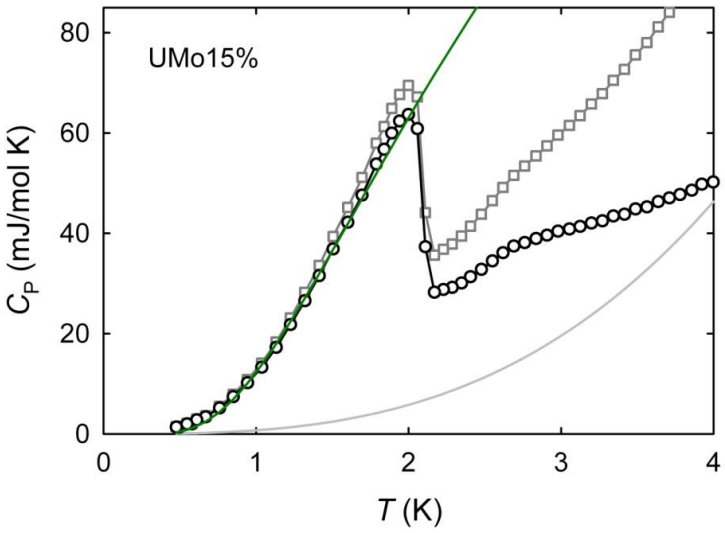

Figure 6.16. Low-temperature part of the specific heat for U-15 at.% Mo sample (grey symbols). Grey curve shows phonon contribution of specific heat which was subtracted (black symbols) from the initial data. After subtraction data was approximated (green curve) by the exponential term $\exp(-\Delta/k_B T)$.

To study in details superconducting transitions we also performed measurements at low temperatures. Results of the calorimetric study of superconducting phase transitions are plotted in fig. 6.15. For the 15 at.% Mo splat

we can see the λ-type anomaly marking the 2nd order phase transition. Its temperature agrees well with T_c determined from resistivity, marked by the respective vertical bars. The length of the bar should correspond to the difference of the specific heat of the superconducting and normal phase, calculated to be $\Delta C = C_s - C_n = 1.43 \cdot \gamma_e \cdot T_c$ in the weak coupling regime. The actual size of the step reaches such value of ΔC, calculated by means of the γ_e-value given in Table 2. This not only proves that the superconductivity is a bulk effect, but also points to a fact that a weak-coupling may be a good approximation. The specific heat after the subtraction of the phonon part C_{ph} can be well approximated (fig. 6.16) by the exponential term $\exp(-\Delta/k_B T)$ with the gap width Δ = 3.3 K, which is in a reasonable agreement using the BCS expression $2\Delta = 3.52 \cdot T_c$, giving Δ = 3.7 K. The peaks shift to lower temperatures with decreasing Mo concentration (fig. 6.15) following the trend of T_c observed already at resistivity. They also become lower and broader, which may reflect certain inhomogeneity of the Mo distribution and its impact in the concentration range, in which the T_c-values vary more with Mo concentration than around 15%, where they are close to a maximum.

Only very weak feature related to the superconducting transition was found in specific heat for pure-U splat. It suggests that only small fraction of the sample is really superconducting. This is in apparent contrast with the zero electrical resistivity. The only interpretation is that the superconducting fraction forms a 3D network, which is possible e.g. when the superconducting fraction is concentrated at grain boundaries. This finding supports the lack of superconductivity observed in good-quality U single crystals [1].

As we showed above, the size of the ΔC step for 15 at.% Mo can be well estimated due to the sharpness of the transition. It fulfills entirely the BCS expectations. For other samples, it is more difficult to evaluate the jumps, but they are apparently smaller than the calculated ones based on the real experimental γ_e-values. For splats with lower Mo concentrations (< 11%) the samples contain a certain amount of the α-phase, which has a lower γ_e-coefficient. The bars therefore represent a lower estimate. If we took for all such splats for example the γ_e-values for well defined γ-U phase with 15% Mo, the calculated bars ($1.43 \cdot \gamma_e \cdot T_c$) would be, as higher estimate, up to 50% longer. The peak broadening is particularly noticeable for 10% Mo. We cannot be sure whether the broadening is “intrinsic” or related to

the Mo concentration distribution, which could have been particularly large for this sample. In fact we observed some sample dependence for 11% Mo, at which concentration several splats were produced. The peak becomes again narrower for 6 and 3 at.% Mo. The fact that they exhibit almost identical T_c (≈ 0.7 K determined from $C_p(T)$) indeed indicates that possible Mo concentration variations do not play much role in this regime. The size is however smaller than the BCS estimate. The fact that it yields about 50% of $1.43 \cdot \gamma_e \cdot T_c$ for 6% Mo and 25% $1.43 \cdot \gamma_e \cdot T_c$ for 3% Mo (not shown in fig. 6.15) suggests that the observed superconductivity has to be associated with the *bcc* phase, the concentration of which progressively decreases with decreasing Mo concentration. We cannot, however, assume that there is a simple phase separation and the superconductivity of 11% Mo phase would remain in gradually reduced fraction as the contents of Mo decreases. That would lead to the reduced anomaly in $C_p(T)$, but the T_c value would remain constant and higher than 1 K. On the other hand, if superconductivity in the two-phase region would be due to the α_b'-phase, its fraction would decrease with increasing Mo concentration, which is at variance with our observations. The detailed phase analysis of the presumably two-phase region for low Mo concentrations, which can be done by means of EBSD, is left for further research.

The reaction of superconducting transitions to magnetic field was studied also by means of specific heat, providing data complementary to electrical resistivity. To see how the T_c anomalies develop, we measured low-temperature specific heat also in applied magnetic fields (fig. 6.17). The height of the peaks decreases and they are shifted to lower temperatures and broaden. For 15% Mo, the critical fields as a function of field lay on the same line with the resistivity data (fig. 6.12). The case of pure-U splat, for which also both methods were used, is different. Although T_c was determined as 1.24 K from resistivity (as the transition mid-point) and the sample is in zero-resistance state at T = 1.1 K, the anomaly in $C_p(T)$ looks like concentrated to the temperature range just below 1.0 K. Only a detailed inspection reveals that the curves in 0 T and 0.6 T start to deviate between 1.1 and 1.2 K already. The broad transition can mean that there is actually a broad distribution of T_c values, the upper ones can be associated with the resistivity T_c = 1.24 K.

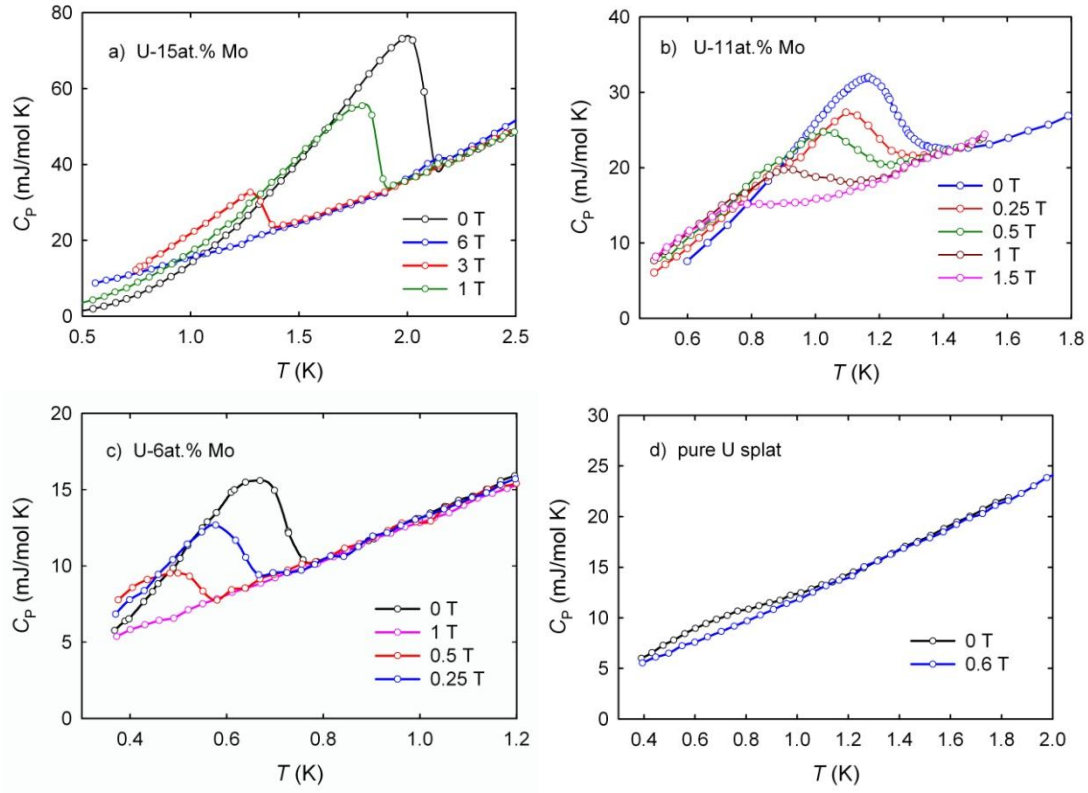

Figure 6.17. Temperature dependence of specific heat C_p and its field variations display anomalies related to superconducting phase transition for selected U-Mo splat samples.

In any case, the superconductivity of pure-U splats differs from all the Mo-containing splats by the fast suppression by magnetic field (fig. 6.15 and Table 2). As the anomaly is removed in the field below 0.6 T, it is undoubtedly related to superconducting phase transition, which, however take place only in a limited volume.

The concentration dependence of T_c is shown in fig. 6.18 in comparison with literature data from Ref. 28. The highest T_c value is observed for 15 at.% Mo. It is in good agreement with literature data, where T_c has a maximum at concentrations 15-19 at.% Mo. The difference of T_c values for samples with lower Mo concentration in comparison with literature data could be due to different sample preparation methods and as result different phase composition of the samples.

To check the correlation between $-(d\mu_0 H_{c2}/dT)_{Tc}$, the electronic specific heat coefficient γ_e and electrical resistivity we use so-called dirty-formula used e.g. for Chevrel-phase compounds [91]. Using our results (Table 2), the resistivity value in

the normal state was deduced to be $\rho = 88$ μΩcm, 67 μΩcm and 62 μΩcm, respectively, for U-Mo alloys with 11, 12 and 15 at.% Mo, that is lower than experimentally measured values but the values have the right order of magnitude.

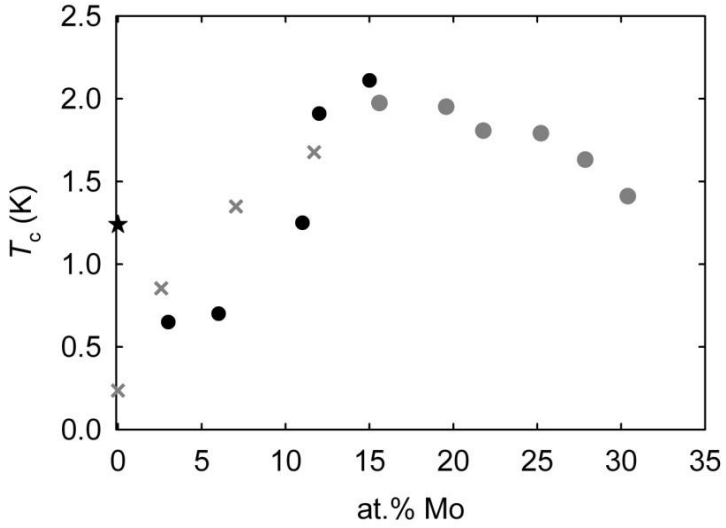

Figure 6.18. Concentration dependence of the critical temperature T_c. Our data on U-Mo splats are marked by black circles, the data from Ref. 28 are grey circles (claimed γ-phase) or grey crosses (claimed α-phase). This distinction should be taken with caution; the research in Ref. 28 apparently did not include detailed structure analysis. The black star marks the T_c of pure U splat.

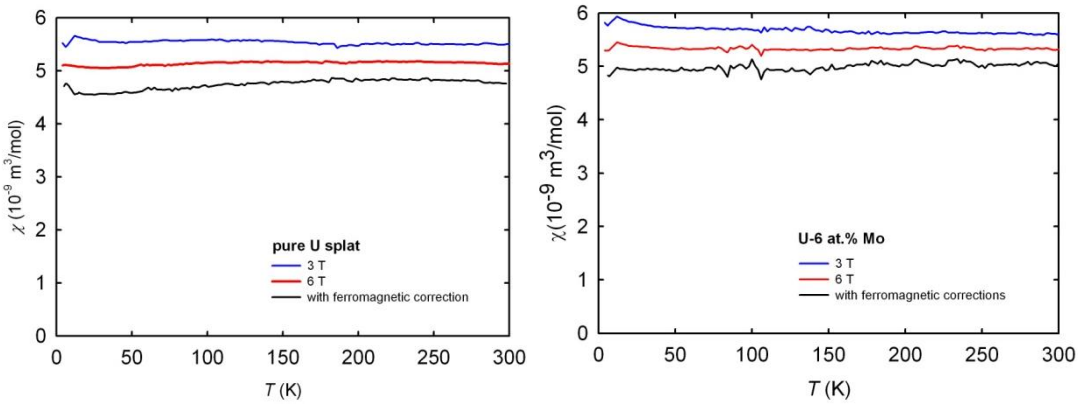

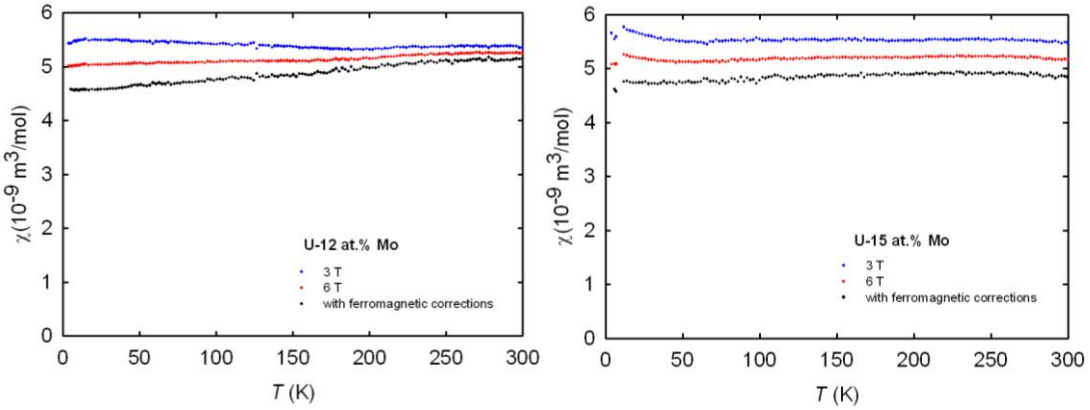

Figure 6.19. Temperature dependence of magnetic susceptibility for some selected U-Mo splat samples (0, 6, 12 and 15 at.% Mo). Measurements in different magnetic fields revealed presence of small amount of ferromagnetic impurity. Corrected data with the subtraction of ferromagnetic signal is also presented on graphs for comparison.

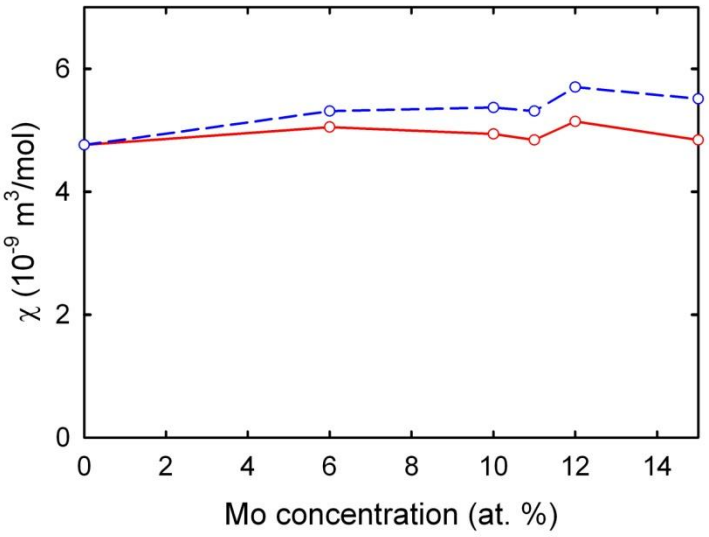

Figure 6.20. Concentration dependence of magnetic susceptibility at 300 K for U-Mo splat samples indicates only very small increase with Mo concentration (red line – per mol; blue line – per mol U).

As next, we investigated the samples by means of magnetization measurements in the temperature range 4 - 300 K. All U-Mo splat samples exhibit a small amount of a ferromagnetic impurity with T_C far above the room temperature, which could be eliminated by measurements in several magnetic fields (fig. 6.19).

The corrected data are practically temperature independent, on the level of $5 \cdot 10^{-9}$ m^3/mol for all alloys studied. It may be surprising that the Pauli susceptibility is almost independent of the Mo concentration (fig. 6.20). However, a tentative analysis subtraction a hypothetical contribution of Mo represented by Mo metal susceptibility ($1.04 \cdot 10^{-9}$ m^3/mol) [92] yields the susceptibility per mol U weakly increasing. The situation is somewhat similar to the difference between α- and δ-Pu. Despite γ_e increasing from 17 to 40 mJ/mol K^2 [26,90] the susceptibility changes are only moderate [93]. Although the susceptibility and linear term of electronic specific heat are both proportional to the density of states at the Fermi level in weakly correlated electron systems, the simple proportionality disappears on a more advanced level. The γ_e-value becomes dependent on the spectral density around the Fermi level, which reflects all kinds of low-energy excitations, the susceptibility is affected besides spin polarization also by orbital polarization and spin-orbit coupling. The decoupling of both parameters is not therefore surprising.

6.1.2. U-Zr splats

For comparison, we have chosen Zr doping for further investigation of γ-U alloys because the atomic radius of Zr (1.60 Å) is larger than for U (1.56 Å). We can expect expansion of the lattice and shortest inter-uranium distance. It is opposite effect to a case of Mo doping, where the lattice parameter was decreased with Mo concentration. Such expansion of the lattice can be considered as a "negative pressure" and can give us more additional information about investigated electronic properties of γ-U phase alloys.

Samples of uranium doped by different Zr concentrations (0 - 30 at.% Zr) were melted in argon atmosphere and subsequently moved to the splat cooling system for preparation of splats. In more details preparation methods were discussed in Chapter 5. Bulk sample with 40 at.% Zr (without splat-cooling) was also prepared, but it was not used for further measurements as EDX analysis indicates non-homogenous distribution of Zr in this sample.

At the beginning we characterized the crystal structure of U-Zr splat samples by XRD. The XRD patterns of the splat-cooled U-Zr alloys in the as-formed state are

shown in Fig. 6.21. Diffraction patterns were measured directly from the surface of splats. For an easier comparison, we showed the normalized XRD pattern (i.e. the intensity of the most intense reflection at around $2\theta = 36^{o}$ was set to 1). They are then shifted upwards along the *y*-axis with respect to each other to guide the eyes.

Coexistence of two phases ($\alpha+\gamma$) was indicated in the splat-cooled pure U, where the phase α is a dominant. EBSD confirmed a small amount of the (cubic) γ-U phase retained at room temperature alongside the majority (orthorhombic) α-U phase for pure U splat (structure investigation for pure U splat described in details in chapter 6.1.1). The intensity of α-U peaks decreases with addition of Zr, while the reflections of γ-U increase visibly. The reduction of α-U with increasing Zr concentration is clearly seen by decreasing of $\alpha(110)$ and $\alpha(111)$ peaks (fig. 6.21 right panel). These peaks persist for Zr concentrations 11 at.% and 15 at.% but become very broad for sample with 20 at.% Zr. These changes in X-ray diffraction pattern of U-Zr alloys illustrate the phase transformation from the α phase to γ with increasing Zr concentration. Finally, the α-phase peaks become indistinguishable and only feeble broad bumps can be found for U-30 at.% Zr. So we can consider this sample as practically a single-phase γ- alloy. The tetragonal distorted *bcc* structure (γ'-phase) was not observed for any U-Zr sample. We should mention here, that in Ref. 34 single-phase γ-alloys were obtained for the Zr concentrations between 25 at.% and 80 at.%. We can conclude that the γ-phase is the dominant for all splat samples with Zr concentrations $\geq$ 11 at.%. Most of γ-reflections (including the main peak $\gamma(111)$ at 35.9°) are broadened. A reason for such broadening can be seen in the overlap of the γ-peaks with the peaks of the α-phase. But α-peaks decrease with Zr concentration. So the main reason for peaks broadening should be in additional disorder by randomly distributed Zr atoms (less probable due to almost identical atomic size) and/or limited grain size due to splat-cooling. This suggestion is confirmed by the fact that peaks broadening increases with Zr concentration.

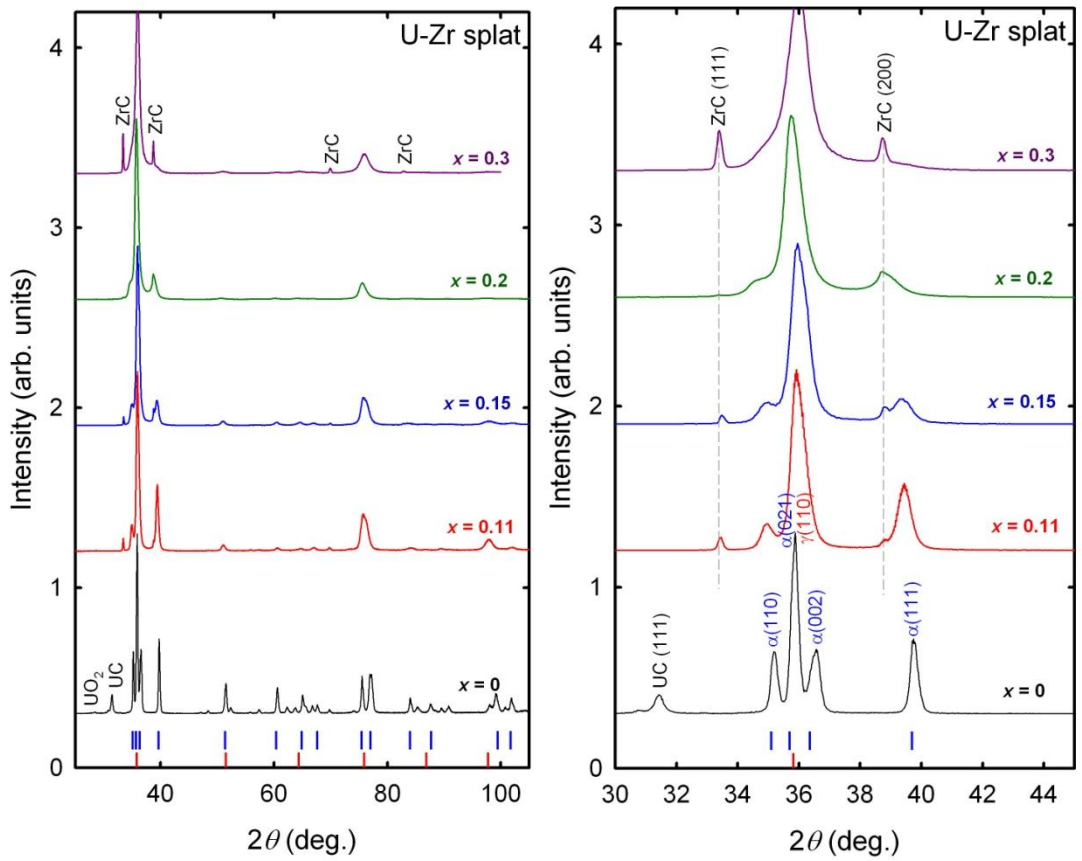

Figure 6.21. X-ray diffraction patterns of U-Zr splats for various Zr concentrations. Each curve was normalized to the intensity of the most intense peak at $2\theta = 36^{o}$ - 37^{o} and then shifted upwards. The vertical ticks indicate the main XRD patterns of α-U (blue) and γ-U (red) structures. The two peaks at low angles for pure U splat belong to surface impurities UO_2 and UC. Peaks of ZrC impurity are observed for samples with Zr. The indices of four main α-U reflections and γ-U are given at the top. (right panel) The low-angle X-ray reflections of selected U-Zr alloys illustrates the phase transformation from the α phase to γ.

In addition, UC(111) and UO_2(111) impurity peaks were observed in the low-angle part of the XRD pattern for pure U. These impurities are segregated at the surface of the splat and can be easily removed by scraping (XRD peaks of impurities are highly reduced after scraping). Narrow peaks of ZrC were observed for U-Zr samples with the most intense reflections ZrC(111) and ZrC(200) at 33.4° and 38.7° respectively. Traces of carbon are ubiquitous in uranium metal, and it seems that it couples preferentially to Zr when it enters the alloy and moreover it has a high surface segregation tendency.

We also notice, that no sign of the phase UZr_2 (δ-phase) was found in XRD patterns even for samples with high Zr content (20 and 30 at.% Zr).

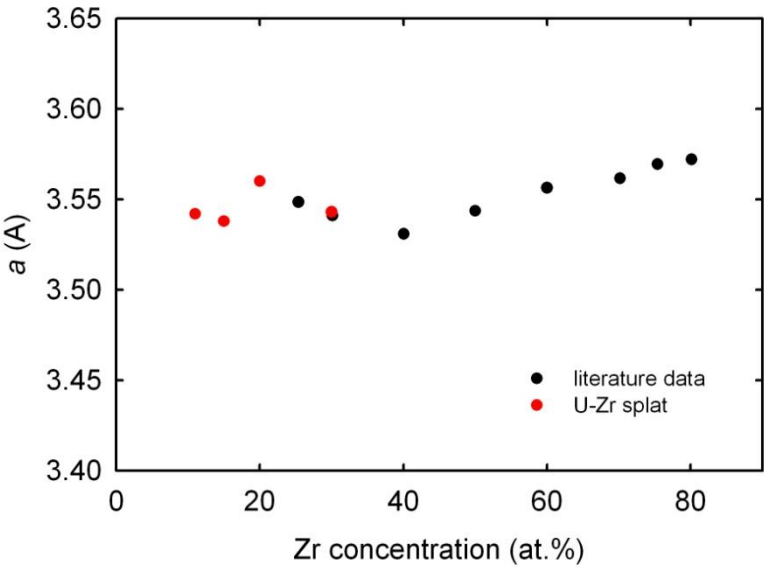

Figure 6.22. Lattice parameters of the U-Zr alloys with γ-phase structure (*bcc*) as a function of Zr content. The data for high Zr concentrations is taken from Ref. 34 and references therein (black circles) is shown for a comparison. Lattice parameters for our U-Zr splat samples are marked by red circles.

The lattice parameter *a* obtained from the structure refinement for the *bcc* γ-phase detected in the splat-cooled U-Zr alloys as a function of Zr concentration is shown in fig. 6.22. For comparison, the data for high Zr concentrations from Ref. 34 and references therein are also included. Our data are in a good agreement with the literature data. Numerical values of *a* for the U-Zr alloys are also given in Table 3. We should mention that the shortest inter-uranium distance (see Table 3) for γ-phase in U-Zr samples is below the Hill limit (3.4 – 3.6 Å). That is compatible with superconductivity of the U-Zr γ-phase alloys.

As it was expected, the lattice is somewhat expanded by addition of Zr atoms in the γ-phase structure. As a result, the lattice parameters for U-Zr splats are significantly higher than for U-Mo. For example, for 15 at.% of Zr doping gives the value a = 3.538 Å, and for 15 at.% Mo a = 3.440 Å. The difference is due to atomic radii of Mo (1.40 Å), U (1.56 Å) and Zr (1.60 Å).

Zr concentration. x	$a = b = c$ (Å)	$d_{U\text{-}U}$ (Å)
0.11	3.542	3.067
0.15	3.538	3.064
0.2	3.560	3.084
0.3	3.543	3.068

Table 3. Lattice parameters and shortest inter-uranium distance for γ-phase U-Zr splat samples with different Zr concentration: 11, 15, 20 and 30 at.% Zr.

The temperature dependence of the resistivity of U-Zr splats is shown in fig. 6.23 in comparison with the resistivity of the pure U metal (bulk U) from the same batch, which was used as a precursor for the splats production.

As was already mentioned in Sub-chapter 6.1.1, the bulk U and pure U splat samples exhibit typical temperature dependence with weakly negative $d^2\rho/dT^2$. Anomalies related to charge density wave transition, which were reported for single crystal U [23,84], were not observed. The residual resistivity ρ_0 value increases from 10 μΩcm for bulk U to 14 μΩcm for pure-U splat sample, and this increment remains almost constant for the whole temperature range, suggesting that in the spirit of the Matthiessen's rule it is due to the higher amount of defects in the crystal lattice of the splat sample. Resistivity increases smoothly with increasing T from 3 to 300 K and below 50 K $\rho(T)$ follows a quadratic dependence, which reflects the electron–electron scattering (see fig. 6.10): $\rho = \rho_0 + aT^2$. The values of $a = 15.4 \cdot 10^{-4}$ μΩcm/K^2 and $a = 16.3 \cdot 10^{-4}$ μΩcm/K^2 were estimated, respectively, for the pure bulk- and splat-cooled U samples.

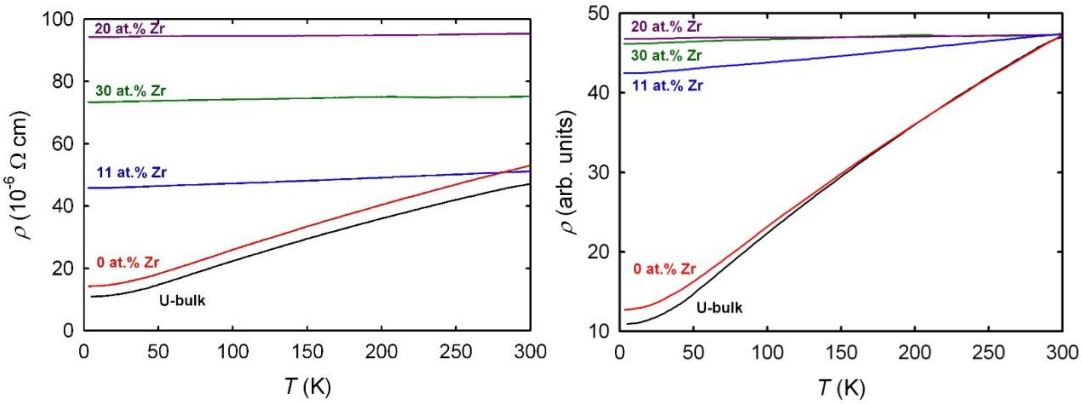

Figure 6.23. Temperature dependence of electrical resistivity for U-Zr splats with various Zr concentrations compared with bulk uranium data. Data is presented in absolute values (left panel) and normalized to the same value at 300 K (right panel) to show changes of slope for resistivity temperature dependence.

The alloys with Zr, which mostly consist of the γ–phase, have the resistivity much higher than for pure U splat (Table 4) and similar to the U-Mo case exhibit dramatically different temperature dependence (fig. 6.23). Instead of the dominant increase of ρ with increasing T, common in metals, we observed different behavior. Splat samples with 20% and 30% Zr have flat temperature dependence but still remain very small (close to zero) positive $d\rho/dT$ for whole range of measured temperatures (4-300 K). The residual resistivity ρ_0 is highly enhanced for these splats (94 μΩcm for 20% Zr and 73 μΩcm for 30% Zr) in comparison with pure U splat and bulk U samples The maximum resistivity value is reached for sample with 20 at.% Zr. As discussed in the context of U-Mo alloys, such behavior is associated with strong atomic disorder. We suggest that in our case the statistically distributed dopant atoms lead to a large disorder effect. Additional disorder can be induced by ultrafast splat-cooling. All that leads to weak localization similar to the U-Mo case. The quantitative difference at U-Zr is that the absolute resistivity values remain somewhat smaller, which is the reason why the negative slope does not develop for at least for low Zr concentrations. We should mention here, that although we found very small positive slope of the temperature dependence for our U-Zr splats, Barnard in his paper [35] reports about negative slope ($d\rho/dT < 0$) for sample with 70 at.% Zr. Probably negative slope can be observed for U-Zr splats but for higher Zr concentrations, i.e. over 30 at.% Zr.

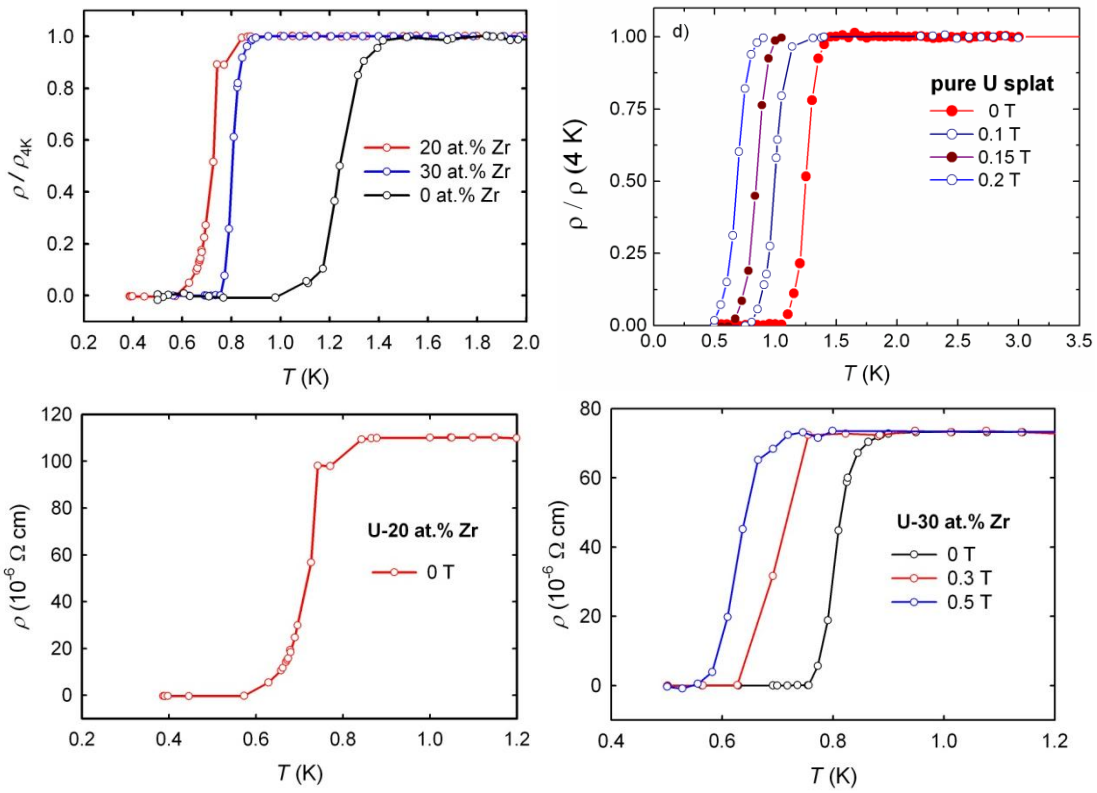

Figure 6.24. Low-temperature resistivity of U-Zr alloys (with 0, 20 and 30 at.% Zr) prepared by splat cooling: comparison of the resistivity in zero field and the results in applied magnetic fields. The curves were normalized to respective resistivity values at T = 4 K.

In order to observe superconducting transitions, resistivity was measured in the low-temperature range (down to 0.4 K, see fig. 6.24). All curves are normalized to the resistivity value at 4 K. The sample U-11 at.% Zr appeared non-superconducting, at least superconducting transition was not observed down to 0.5 K. We can only speculate that T_c for this sample can be below 0.5 K. Also U-11 at.% Zr sample contains a significant fraction of the α-phase, which has the T_c value variable over a significant temperature range, as seen from the literature data [22]. Excluding this sample, we found that all U-Zr splat samples become superconducting. The critical temperature of superconducting transition slightly increases with increasing Zr concentration (T_c = 0.72 K and 0.80 K for 20 at.% and 30 at.% Zr respectively). Such increase of T_c correlates well with the data reported by Huber and Ansari [34] for U-Zr fast quenched alloys. T_c for pure U splat is higher (1.24 K) than for the splats with Zr. The superconducting phase transition seen in resistivity is quite abrupt, especially for 20 at.% and 30 at.% Zr samples. The width of the superconducting

transition in resistivity, is defined as $\Delta T = T(\rho_{90\%})-T(\rho_{10\%})$, can be estimated as 0.06 – 0.07 K for these splats. The superconducting transition for pure U splat is somewhat broader (0.16 K).

Zr conc. x	ρ_{300K} ($\mu\Omega$cm)	T_c (K)	$-\mu_0(dH_c/dT)_{Tc}$ (T/K)	$\mu_0 H_{c2}(0)$ WHH (T)	$\mu_0 H_{c2}(0)$ (T)	γ_e (mJ/mol K^2)	Θ_D (K)
0	53	1.24	0.35	0.30	0.30	11.0	179
0.11	46	-	-	-	-	7.9	173
0.20	94	0.72	≈ 3.5-4.0		≈ 3	11.0	164
0.30	73	0.80	≈ 2.8		≈ 2.2	11.8	165

Table 4. Summary of measured electronic properties of the U-Zr splat samples.

Applying external magnetic field, the superconducting transitions shift towards lower temperatures as expected, and eventually the superconductivity is suppressed entirely (fig. 6.24). For pure-U splat, the superconductivity is suppressed at lower fields than for samples containing Zr. On the other hand, the γ-U type splats (20% and 30% Zr) exhibit much higher field resistance (higher critical field H_c). This gives an idea that the α-U and γ-U superconductivity are qualitatively different. Situation is similar to case of U-Mo splat samples, where we observe qualitative difference between pure U splat (α-U) and splat samples which retain the metastable γ-U phase.

For further investigation we performed specific heat measurements in the range of temperatures 4-300 K (see fig.6.25). Temperature dependence of the specific heat $C_p(T)$ exhibits no sign of CDW anomalies for pure U splat sample. Temperature dependence for U-Zr splat samples shows normal metal behavior as in the case of U-Mo splat samples.

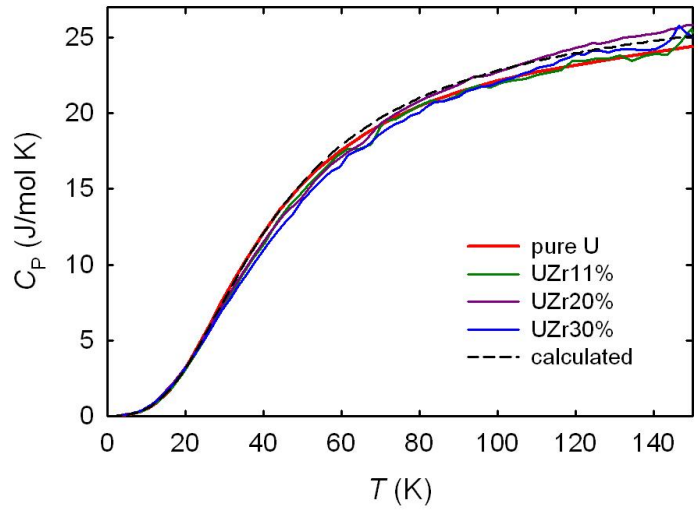

Figure 6.25. Temperature dependence of the specific heat of the selected U-Zr splats and pure U splat. The dashed curve shows specific heat temperature dependence calculated by the Debye function (θ_D = 170 K) with addition of electronic contribution (γ_e = 11.0 mJ/mol K^2).

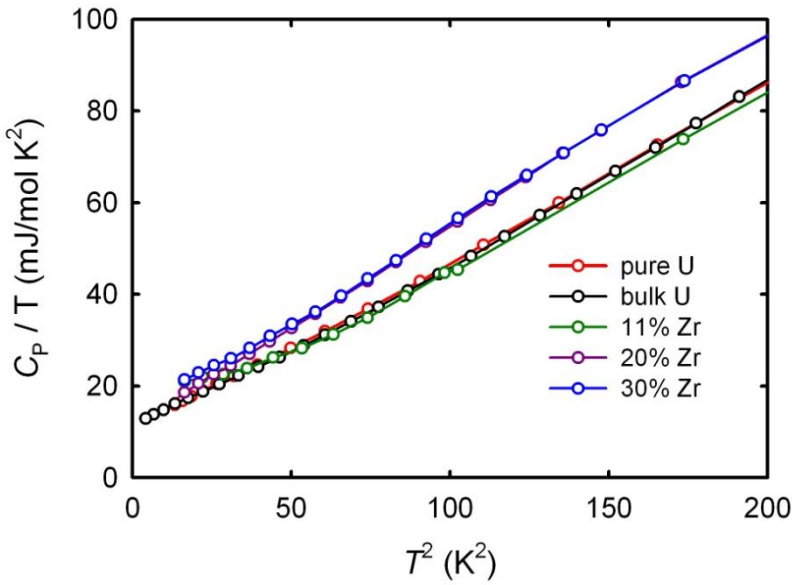

Figure 6.26. Temperature dependence of the specific heat of the selected U-Zr splats in the C_P/T vs. T^2 representation. The fits were used to determine γ_e and θ_D.

The low-temperature part plotted as C_p/T vs. T^2 (fig.6.26) was used to determine the Sommerfeld coefficient of electronic specific heat γ_e ($C_p/T = \gamma_e + \beta T^2$) and the Debye temperature θ_D ($\beta = 12\pi^4 R/5\theta_D^3$). The results are given in Table 4. The value γ_e = 11.0 mJ/mol K^2 for pure U splat is in good agreement with the data

obtained for the bulk U sample using the same experimental setup (11.2 mJ/mol K^2), but slightly higher than literature data for uranium single crystal (9.13 mJ/mol K^2) [23]. Sommerfeld coefficient slightly increases with Zr concentration (disregarding the mixed-phase sample U-11 at.% Zr). This increase will be more evident if values are recalculated per mol of U. So γ_e values increase up to 11.8 mJ/mol K^2 (i.e. 16.9 mJ/mol U K^2) for U-30 at.% Zr. This indicates a certain increase of the density of states at the Fermi level for γ-U. The values are close to that was observed for γ-phase U-Mo splat U-15 at.% Mo γ_e = 16.0 mJ/mol K^2 (i.e. 18.8 mJ/mol U K^2). Such increase of DOS at the Fermi level can be ascribed to the increasing atomic volume and shortest inter-uranium spacing and also to the larger atomic radius of Zr than for U (1.60 Å and 1.56 Å respectively). The inter-uranium spacing can be also affected by the dilution of the U lattice by Zr atoms. As a consequence, 5*f*-band becomes narrower.

The Debye temperature values were also determined from the low-temperature part of specific heat, linear in C_p/T vs. T^2. For pure U splat θ_D is equal 179 K, which is little lower than the given values for bulk α-U in Ref. 23, where values by different authors range from 183 K to 256 K. The Debye temperature decreases with Zr concentration down to 164 K for U-20 at.% Zr and 165 K for U-30 at.% Zr, indicating softening of the lattice. Such decrease of the Debye temperature is much smaller than that was observed earlier for U-Mo splats, where θ_D decreases down to 139 K.

Fig. 6.25 demonstrates that the Debye function (θ_D = 170 K) (with addition of electronic contribution γ_e = 11.0 mJ/mol K^2) reasonably well describes all the U-Zr data.

In order to study in details superconducting transitions we also performed measurements of specific heat at low temperatures (0.4-4 K). Results of the calorimetric study of superconducting phase transitions are plotted in fig. 6.27. We observed peaks related to superconducting transition. Peaks are rather broad comparing to the case of U-Mo alloys. The shape of the peak for this sample is not of a λ-type. The peaks shift to lower temperatures with decreasing Zr concentration (fig. 6.27) following the trend of T_c observed already at resistivity. They also become lower and broader, which may be described by certain inhomogeneity of the Zr distribution or by inhomogeneity due to mixing of α- and γ-phases. The critical

temperature for the sample with 20 at.% Zr is little bit higher (0.79 K) than it was determined from the resistivity measurements. Only very weak feature related to the superconducting transition was found in specific heat for pure-U splat, as discussed in the U-Mo part.

The difference of the specific heat of the superconducting and normal phase predicted in the weak coupling regime can be calculated by $\Delta C = C_s - C_n = 1.43 \cdot \gamma_e T_c$. The actual size of the ΔC step for U-30 at.% Zr does not reach the calculated one using of the γ_e-value given in Table 4. The actual ΔC is only 30-40% of the calculated step. It can be perhaps interpreted as inhomogeneous superconductivity even in zero magnetic field.

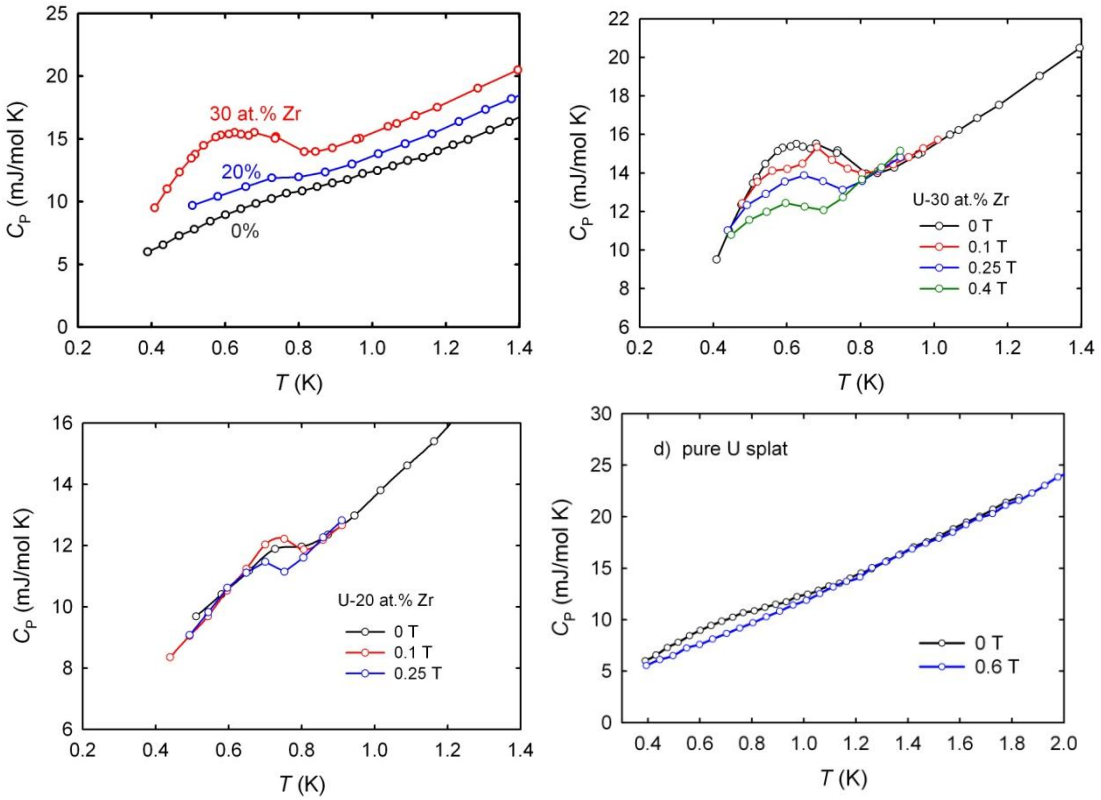

Figure 6.27. Temperature dependence of specific heat C_p and its field variations display anomalies related to superconducting phase transition for selected U-Zr splat samples and pure U splat.

The anomalies are further suppressed in applied magnetic fields (fig.6.27). The height of the peaks decreases, they are shifted to low temperatures and broaden with magnetic fields.

Similar to U-Mo, we clearly can see the difference in behavior of T_c in applied magnetic fields with respect to pure U. Superconductivity is more field resistant in samples 20 at.% Zr and 30 at% than for pure U splat. We suggest that we observe two types of superconductivity related to α- and γ-phases as it was already observed in the case of U-Mo splats.

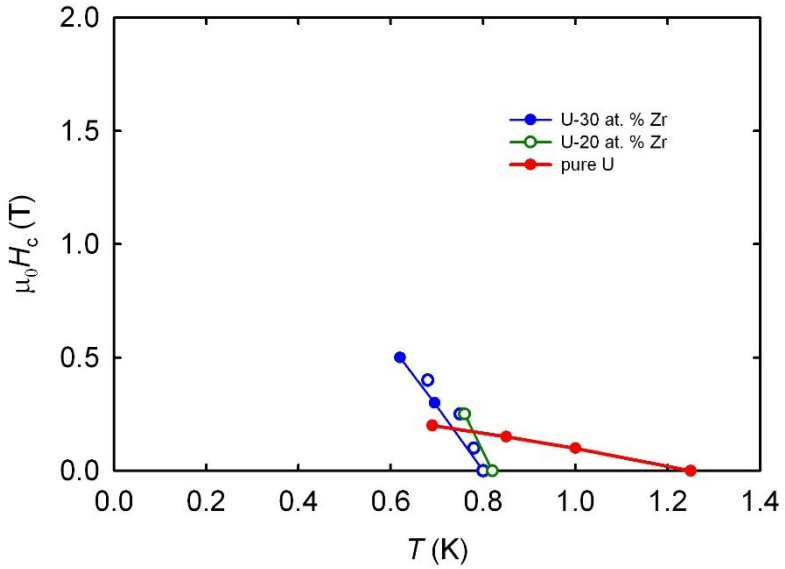

Figure 6.28. Critical magnetic field H_c vs temperature T for pure-U and U-Zr alloys prepared by splat cooling, as determined from electrical resistivity (full circles) and specific heat (empty circles).

The results are summarized in fig.6.28, where we use the data of both specific heat (empty circles) and resistivity measurements (solid circles). For 30 at.% Zr, the critical field as a function of field was determined from the specific heat data, which give the T_c values close to the points observed from the resistivity measurement. For 20 at.% Zr only points from specific heat measurements was used as resistivity for this sample was not measured in magnetic fields. We could not approximate our data similarly to Mo alloying due to low T_c values, which are close to the experimental limit (0.4 K). So we use only a rough estimate for the critical field values due to lack of data points. For approximation of 20 at.% Zr and 30 at.% Zr data we used a linear dependence as we have lack of data points. Data for pure U splat was approximated by a quadratic polynomial including a linear term. Difference between the superconductivity of samples is clearly visible from the fig. 6.28. The upper critical

field for the samples with 20 at.% and 30 at.% Zr estimated from measurements data is approximately 10 times higher than for pure U splat (0.3 T) and lay in the range 2.2-3 T. The respectively values are given in the Table 4. To quantify the difference, we also determined the critical slope at T_c, $-\mu_0(dH_{c2}/dT)_{Tc}$. Critical slope is also approximately 10 times higher for 20% Zr and 30% Zr (2.8-4 T/K) than for pure U splat (0.35 T/K), which gives an idea that the α-U and γ-U superconductivity are qualitatively different. The critical field values observed for U-Mo γ-phase alloys are, however, even higher.

The high upper critical slope at T_c and correspondingly high upper critical field of the γ-U superconductivity corresponds to materials as A15 superconductors with strong coupling, which have, however, the T_c values exceeding 10 K. The difference between the standard A15 superconductors and γ-U alloys is the disorder. It is interesting to point out that the A15 superconductors as Nb_3Ge, V_3Si have the T_c values much reduced by progressing disorder, increasing the resistivity to the values around 100 μΩcm [88].

The BCS theory predicts the value of critical slope $-dH_{c2}/dT$ to depend on normal-state parameters and on T_c in a way $-dH_{c2}/dT \sim T_c \cdot \gamma_e^2$, where γ_e is the Sommerfeld coefficient of electronic specific heat in the normal state [89]. Then, if all other microscopic parameters as the Fermi surface remained unchanged, the increase of T_c and γ_e between the α-U (pure U splat) and γ-U (U-30 at.% Zr) phases would make $-dH_{c2}/dT$ values be more or less of the same order. The real enhancement is by the factor of 8.

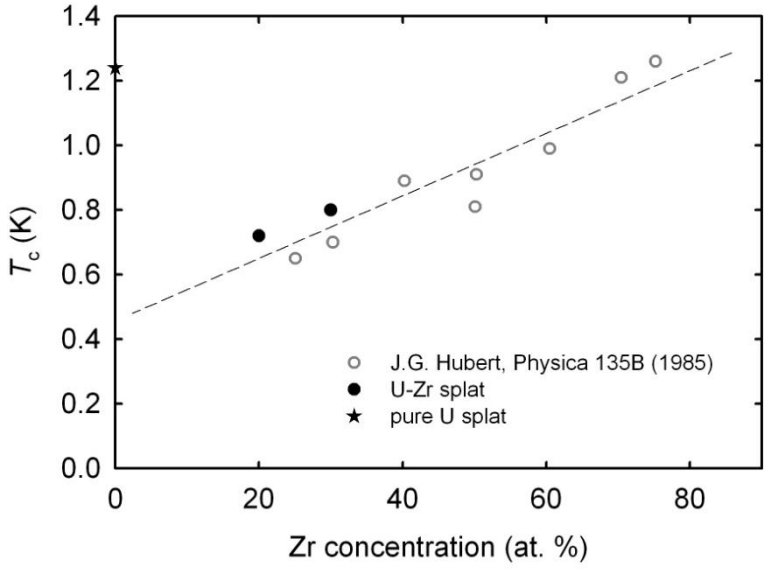

Figure 6.29. Concentration dependence of the critical temperature T_c. Our data on U-Zr splats are marked by black circles, the data from Ref. 34 are marked by open circles. The black star marks the T_c of pure U splat sample (0 at.% Zr).

The other thing that obviously shows the difference in superconductivity related to α-U and γ-U is critical temperature. Fig. 6.29 shows concentration dependence (in at.% Zr) of the critical temperature. T_c for samples, where γ-phase is the dominant phase, is follow to the same linear dependence as was described in Ref. 34. Critical temperature for pure U splat is clearly out of this dependence. It again confirms that superconductivity related to α-phase and γ-phase is different.

6.1.3 Discussion of U-Mo and U-Zr splats

U-Mo and U-Zr splats stabilized in γ-U structure by splat cooling. Single phase γ-U samples was obtained already at concentration of Mo ≥ 11 at.%, which is less than obtained earlier by other techniques. For U-Zr samples, pure γ-U was stabilized at concentrations of Zr = 30 at.% Zr.

Lattice parameter and shortest inter-uranium distance are equal a = 3.44 Å, d_{U-U} = 3.0 Å for γ-U samples with Mo, and a = 3.54 Å, d_{U-U} =3.1 Å for γ-U samples with Zr. The difference is due to atomic radii of Mo (1.40 Å), U (1.56 Å) and Zr (1.60 Å). Inter-uranium distances are much below the Hill limit predicting superconducting ground state for these samples.

Both U-Mo and U-Zr splats are superconducting. U-Mo splats have higher T_c (2.1 K) and sharper features on specific heat related to superconducting transitions than for U-Zr (0.8 K). Nevertheless, both show large $\mu_0 H_{c2}(0)$ and $-\mu_0(dH_c/dT)_{Tc}$ values, which indicates a substantial difference between γ-U phase and α-U phase related superconductivity.

6.2. U-Mo and U-Zr hydrides

The primary aim to investigate hydrides of metastable γ-U splat cooled alloys was to test their stability with respect to hydrogen, which is an Achilles heel of α-U products. As early experiments demonstrated that alloying elements make the hydrogenation much more difficult (high H_2 pressures needed) and alloying elements do not segregate, which would leave ordinary UH_3 as a product, we started to use the γ-U alloys as precursors for synthesis of UH_3-based hydrides, probing interesting magnetic properties of UH_3.

Uranium metal can form a stable hydride β-UH_3, which crystallizes in a cubic structure with large unit cell (8 U atoms per unit cell). β-UH_3 is a ferromagnet with magnetic moments μ = 0.9 μ_B/U [71] and the relatively very high Curie temperature T_C = 165-170 K. The main reason why the 5*f* magnetism arises (U metal is a weak Pauli paramagnet) can be seen in the U-U spacing, enhanced from 2.84 Å (α-U) to 3.30 Å (β-UH_3). This spacing, however, remains below the critical Hill limit (3.40 Å), above which magnetic order should appear systematically.

We use the splat cooled U-Zr and U-Mo alloys retained in the *bcc* structure (γ-U) for hydrogenation. For higher Zr or Mo concentrations, the ultrafast cooling is not necessary for stabilization of γ-phase, and normal cooling in the arc furnace is sufficient to retain the single-phase *bcc* structure. Therefore we could alternatively work further on with ingots for higher concentration. Ingots with Mo concentration ≥18 at.% were used in this work in addition to splats.

For the hydrogenation, the samples were placed in an alumina crucible into a reactor, which could be pressurized to 150 bar of H_2. The reactor was first evacuated down to 10^{-6} mbar and then H_2 gas was introduced at room temperature. We found that minimum H_2 pressure for the hydride formation is irrespective of composition of γ-U alloys in the range 4-5 bar. Higher pressures (up to 100 bar) can only fasten the process, but the H amount absorbed remains the same.

As resulted hydrides have a stoichiometry analogous to UH_3, we used such notations for our hydrides: $(UH_3)_{1-x}Mo_x$ and $(UH_3)_{1-x}Zr_x$. For example, splat sample

with initial composition of U-15 at.% Mo ($U_{0.85}Mo_{0.15}$) form a hydride $(UH_3)_{0.85}Mo_{0.15}$.

6.2.1. $(UH_3)_{1-x}Mo_x$ hydrides

We start to test our samples at hydrogen atmosphere from pure U splat. At the pressure of 1 bar, U metal without doping reacts after several hours long incubation period (needed for diffusion of H through the surface oxide barrier, which is substantial in a splat not subjected to any surface cleaning) in a violent reaction, turning material into very fine powder, prone to self-ignition when exposed to air. Low hydrogen pressure 1 bar allows us to use a glass reactor and to make a photo of hydrogenation process developing in time (see fig. 6.30). After the reactor was opened, the powder started to burn in air.

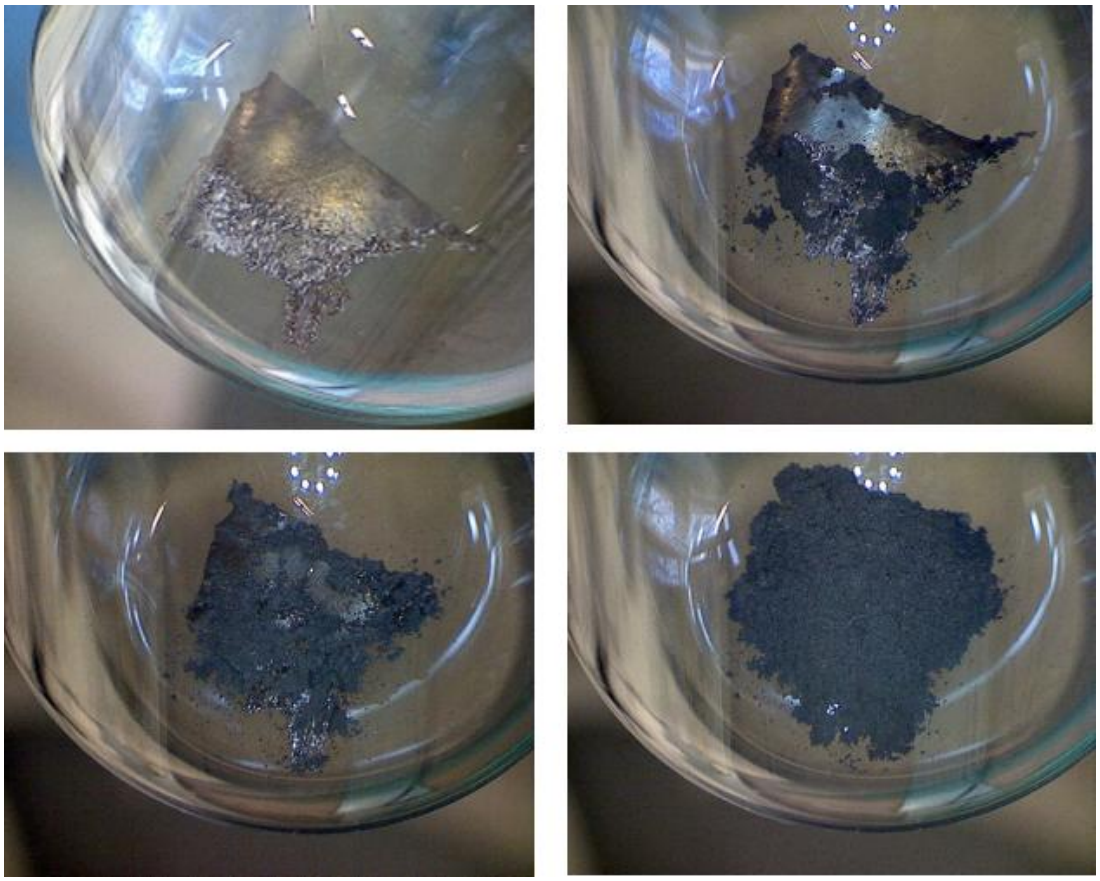

Figure 6.30. Photo of pure U splat hydrogenation process in steps. Uranium metal form a hydride black fine powder, which easily ignites being exposed to air.

We undertook the second attempt of pure U splat hydrogenation at higher pressure (110 bar). This time the reactor was opened only one day after the hydrogenation process had stopped and hydrogen was pumped out from the reactor. Such process apparently slowed down the oxidation, which was proceeding slowly in a residual gas, avoiding the violent burning releasing the exothermic reaction heat in one shot.

Structure investigation by powder X-ray diffraction revealed the presence of two hydride phases, α-UH_3 and β-UH_3. The XRD pattern is shown in fig. 6.31. It is well known from the literature, that α-UH_3, is formed as an unstable transient species, which is subsequently converted into stable β-UH_3. Therefore α-UH_3 was always observed only in a mixture with a large fraction of β-UH_3 [22]. Refinement of XRD patterns gives us relation of the α-UH_3 and β-UH_3 phases inside the sample, which is close to 50%/50%. The concentration of α-UH_3 is further reduced with time, as indicated by XRD study after several months. The repeated XRD patterns also indicated increase of UO_2 impurity peaks (fig. 6.31).

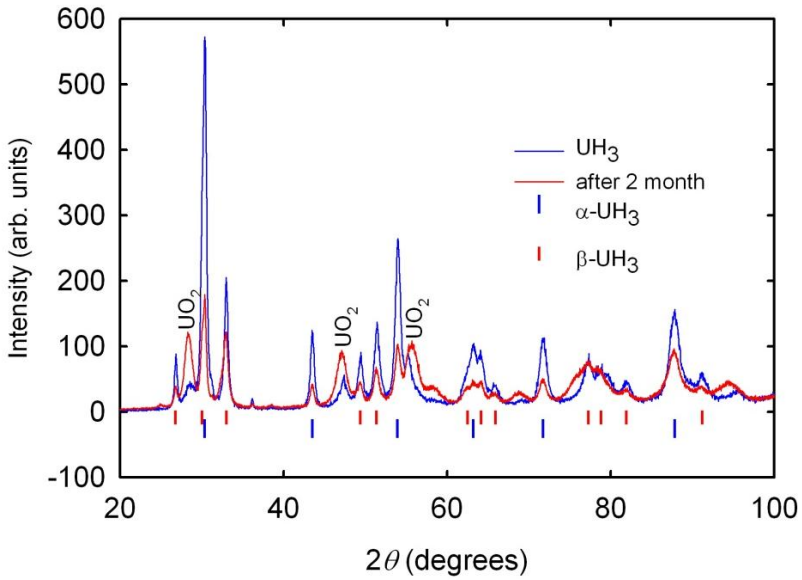

Figure 6.31. Comparison of XRD patterns of the fresh hydride (prepared from pure-U splat) immediately (blue curve) and after 2 months (red curve). The vertical ticks indicate the main peak positions for the (blue) α-UH_3 and (red) β-UH_3. The three main peaks of UO_2 are labelled, as well.

When testing the single phase *bcc* U-Mo alloys, no pressure reduction was registered after one week under the same conditions. This is a signal of a higher

stability of γ-U under hydrogen atmosphere. As next we tried to stimulate the process by higher pressure of H_2 gas. H absorption was achieved under 100 bar, producing material, the stoichiometry of which can be characterized as $(UH_{\approx 3})_{1-x}Mo_x$, therefore, to stress the similarity to UH_3 and to allow easy comparison of magnetic quantities per mole U, we adopted the notation $(UH_3)_{1-x}Mo_x$.

The Mo-doped hydrides are brittle, but they did not turn into fine powder. When starting from splats with ≈ 100 μm thickness, we obtained lamellas several mm long (see fig. 6.32, left panel), which is a convenient shape for resistivity measurements. Massive ingots start cracking, but pieces of several mm^3 can be obtained (see fig. 6.32, right panel). That allows easy studies of bulk properties, as heat capacity using the microcalorimetry technique.

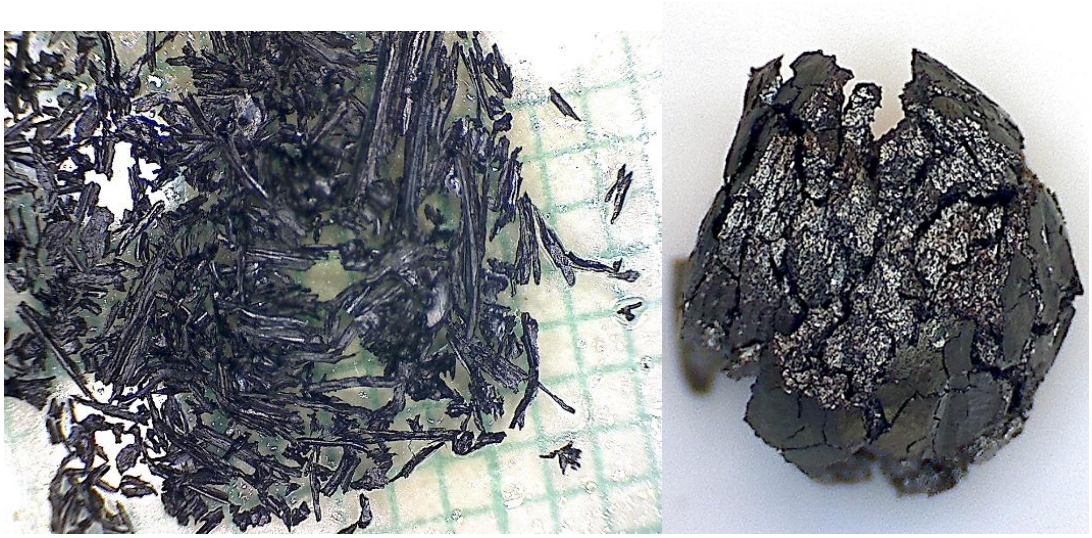

Figure 6.32. Photographs of $(UH_3)_{0.85}Mo_{0.15}$ hydride (left panel), which was made from the splat sample U-15 at.% Mo, and $(UH_3)_{0.82}Mo_{0.18}$ hydride (right panel), which was made from ingot U-18 at.% Mo. The hydride of splat sample consists of elongated particles of several mm long, displayed on a millimetre grid. The hydride of massive ingot starts cracking.

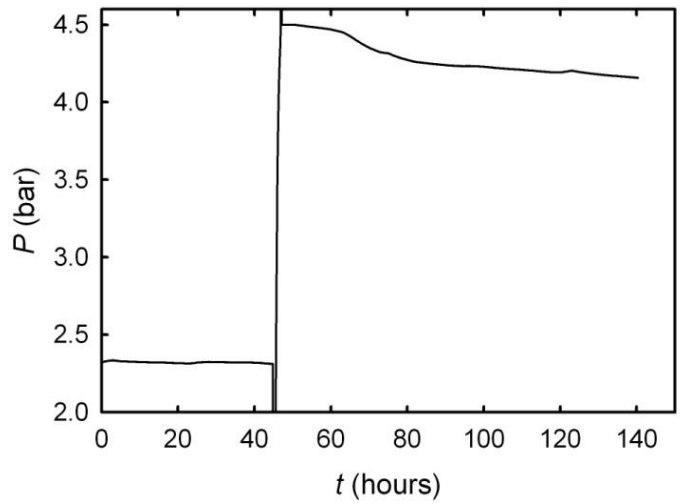

Figure 6.33. Example of hydrogen gas absorption (as a function of time) for $(UH_3)_{0.85}Mo_{0.15}$ monitored by the drop of pressure inside the reactor. Hydrogenation starts at hydrogen pressure close to 4.5 bar.

Testing the lowest pressure for hydrogenation we found that the reaction times extend, and the lowest pressure for which the H absorption was registered, 4.5 bar, needs, after about 1 day of incubation, several days to be completed (see fig. 6.33). High pressure of hydrogen (60-100 bar) was used for most of prepared hydrides to ensure that hydrogenation process goes fast and will be completed.

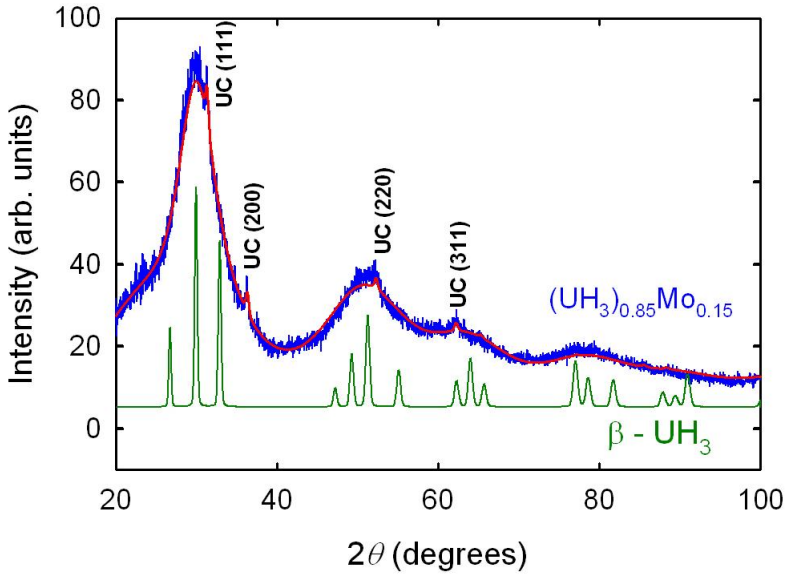

Figure 6.34. XRD pattern of $(UH_3)_{0.85}Mo_{0.15}$ (blue) together with the simulated pattern of β-UH_3 at the bottom (green) and our fit of the experimental data (red) used for the grain-size estimate (for details see the text).

After the hydrogenation was completed, parts of hydride samples were crushed and subjected for structure characterization by X-ray powder diffraction. No substantial difference was observed between XRD patterns of all U-Mo hydrides. As example, XRD pattern of $(UH_3)_{0.85}Mo_{0.15}$ is presented in fig. 6.34. The patterns exhibit only several very broad maxima, pointing to amorphization. Small narrow peaks which correspond to UC impurity phase, which can be observed in most of the hydride samples. The broad maxima can be related to the structure of β-UH_3 (see fig. 6.34 green pattern). A quantitative analysis by using Rafaja model [94] shows that the XRD patterns can be reproduced by assuming nano-crystalline grains of two different size, approx. 1.4 and 0.8 nm (data listed in Table 5). The deduced lattice parameters for all U-Mo hydrides are in the range 6.60-6.65 Å, being close to values from the literature for β-UH_3 (a = 6.64 Å) [22,71]. The shortest inter-uranium distance is in the range 3.30-3.33 Å, i.e. close to the Hill limit.

To have complementary information on structure we used transmission electron microscopy (TEM), using the microscope JEOL JEM 2000 FX. The $(UH_3)_{0.85}Mo_{0.15}$ hydride sample particles were crushed up to fine powder by hand milling in crucible under acetone. The powder obtained was fixed between two Cu grids and holey carbon. Experiment revealed that our hydride sample consist of crystalline grains with different grain size. Some of them close to nanometer size (fig. 6.35), which is confirming results of XRD analysis. But based on analysis of electron diffraction pattern (fig. 6.36) material has some crystal grains (at least part of the sample). To reveal details of structure on the atomic length scale we plan to perform a HRTEM study at ITU Karlsruhe. However, the user program there has been suspended due to legal difficulties.

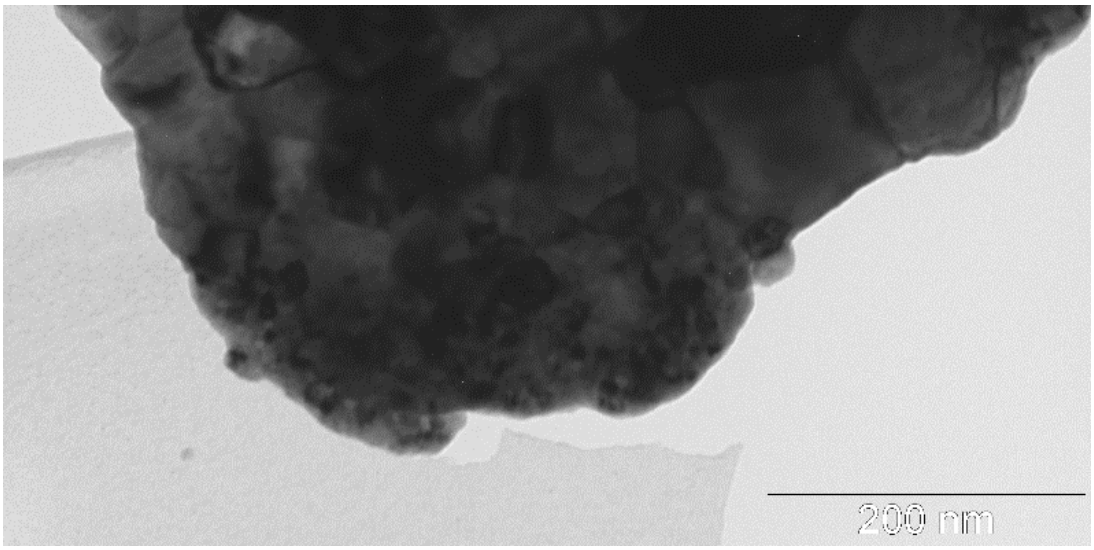

Figure 6.35. TEM image for $(UH_3)_{0.85}Mo_{0.15}$ hydride particle revealed nano-size grains.

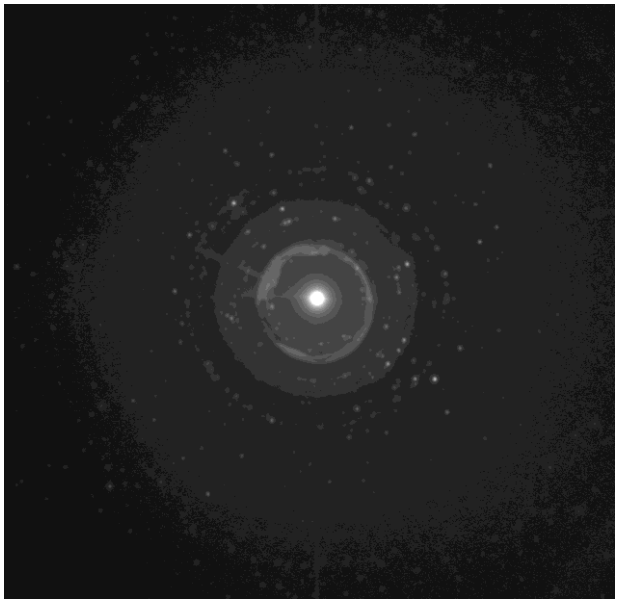

Figure 6.36. Electron diffraction pattern of $(UH_3)_{0.85}Mo_{0.15}$ hydride.

Sample	*a* (Å) (β-UH_3)	Grain size 1 (nm)	Grain size 2 (nm)	H/U
UH_3	6.65	60.8	49.9	
$(UH_3)_{0.88}Mo_{0.12}$	6.62	1.8	1.2	
$(UH_3)_{0.85}Mo_{0.15}$	6.65	1.3	0.7	3.0
$(UH_3)_{0.82}Mo_{0.18}$	6.62	1.4	0.8	2.9
$(UH_3)_{0.75}Mo_{0.25}$	6.60	1.4	0.84	3.0

Table 5. Summary of measured structure properties: lattice parameter, two different values characteristic grain size and hydrogen concentration per formula unit for U-Mo hydrides

Desorption in a closed evacuated volume was performed to determine the hydrogen concentration in prepared hydrides. We used the heating rate 2 K/min. As all H is released from β-UH_3 at 450 ^oC (723 K), we took 500 ^oC (773 K) as an upper limit for the U-Mo hydrides. In selected case heating up to 800 ^oC (1073 K) was tested, which however did not yield any further H release. We typically observed a release in the range 400-450 ^oC in two close steps (fig. 6.37, left), which we assign to two competing processes. The total amount of H_2 released corresponds to approximately 3 H atoms per 1 U atom. Therefore we adopted the formula $(UH_3)_{1-x}Mo_x$. The uncertainty as to the H concentration is affected by the fact that it has to be determined from the pressure increase in the closed system, which is not all at the same temperature. Cooling the reactor to the room temperature leads to a re-absorption of the gas, presumably by the α-U phase. Values of hydrogen concentration for the hydrides are given in Table 5. Deviations of values from the ideal UH_3 composition are within the experimental error, here 0.1-0.3 H/f.u.

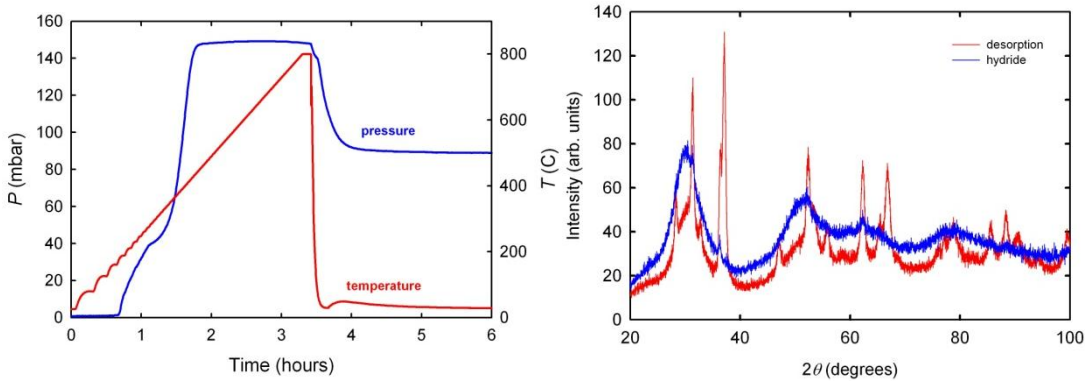

Figure 6.37. Desorption of hydrogen at 800 ^oC (1073 K) with consequent reabsorption during cooling for $(UH_3)_{0.85}Mo_{0.15}$ sample (left panel). Comparison of XRD patterns before and after desorption of hydride (right panel) indicating that only part of the sample converts to γ-U and large amount of β-UH_3 appears in the product due to reabsorption.

After desorption, the material was again characterized by XRD. After heating up to 800 ^oC (1073 K) and cooling, the $(UH_3)_{0.85}Mo_{0.15}$ sample starts to reabsorb

hydrogen from reactor, as seen from the fig. 6.37. From XRD pattern we see that in the sample after desorption a large amount of β-UH_3 phase still remained due to reabsorption (fig. 6.37, right panel). Crystalline narrow peaks can be attributed to the γ-U phase, UC, and UO_2. We observe different results if reactor is evacuated from hydrogen released from sample at the end of desorption (fig. 6.38).

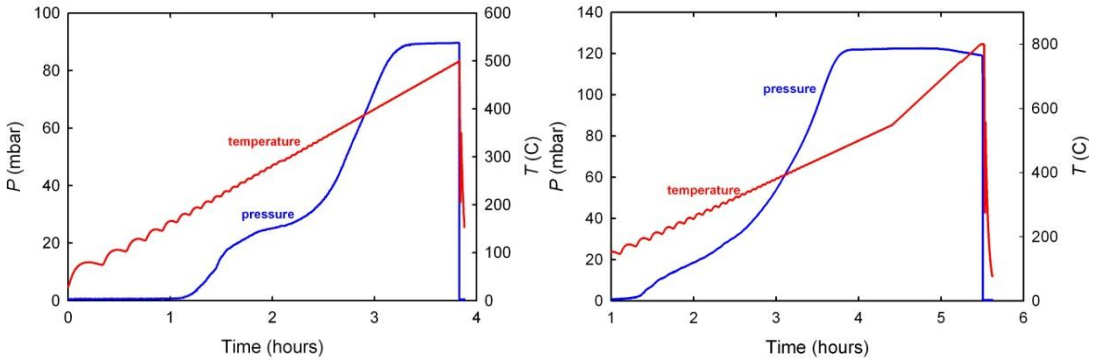

Figure 6.38. The time dependence of reactor pressure during desorption process for $(UH_3)_{0.85}Mo_{0.15}$ hydride up to 500 °C (773 K) (left) and 800 °C (1073 K) (right) with consequent evacuation.

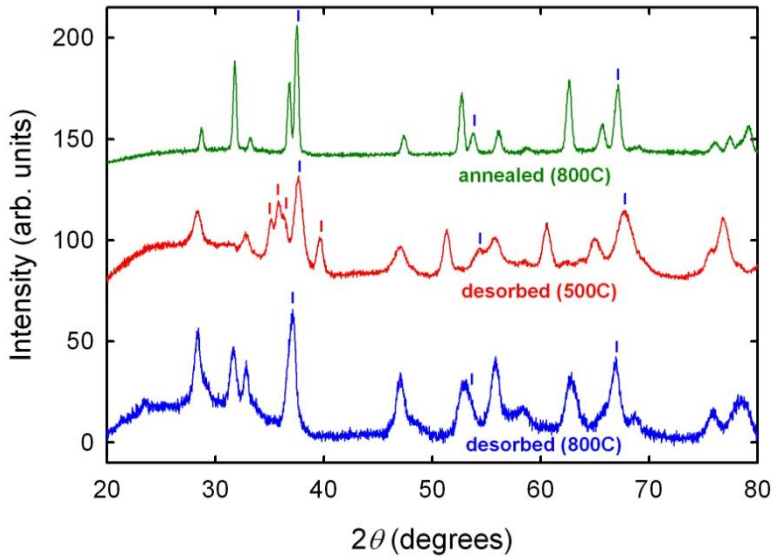

Figure 6.39. Comparison of XRD patterns for $(UH_3)_{0.85}Mo_{0.15}$ after desorption at 500 °C (773 K) and 800 °C (1073 K). After desorption at 500 °C (red pattern), sample was additionally annealed for 1 hour at 800 °C (green pattern). The vertical ticks indicate the main peak positions for γ-U (blue) and α-U (red).

No sign of hydride was observed in XRD patterns after the desorption (fig. 6.39) at 800 ^{o}C (1073 K) with subsequent evacuation of reactor. The hydride is transformed back to the γ-U phase with UC and UO_2 impurities. A large portion of the α-U phase is observed in addition to γ-U, UC and UO_2 in case of desorption at 500 ^{o}C (773 K). The reason for such difference in a phase composition after desorption at different temperatures is the phase transformation of γ-U. By heating up to 500 ^{o}C we not only desorb hydrogen, but also obtain α-U from γ-U, as we already observed earlier in Subchapter 6.1.1 (fig. 6.7 and fig. 6.8). As expected, the α-U peaks completely disappear (see 6.39, green pattern) after annealing (for 1 hour at 800 ^{o}C) in addition to hydride desorption at 500 ^{o}C.

Such recovery of the initial γ-U phase after absorption and desorption can be useful. Here we suggest it as a process of preparation of γ-phase U-Mo alloy powders, which can be used for fabrication of nuclear fuels. Powdering U-Mo alloys is a major issue when fuel fabrication is based on the dispersion technology [95]. There are three processes by which γ-phase U-Mo alloys can be powdered: centrifugal atomization; mechanical machining or grinding; and the hydriding-dehydriding process, also known as HD, or as HMD [96] when a milling operation is performed between these treatments.

When γ-U alloys form a hydride (without activation by heating) they can be easily crushed mechanically due to the brittleness of the hydride to any required particle size. Powders are not only desorbing hydrogen but also turns back to γ-U phase by using heating up to 800 ^{o}C where γ-phase is stable. Metallic luster and hardness are also appear after desorption. The main advantages of this process between that was described in Ref. 96 there is no temperature activation, resulted hydride is not pyrophoric and it is much easier to perform milling process even under air atmosphere.

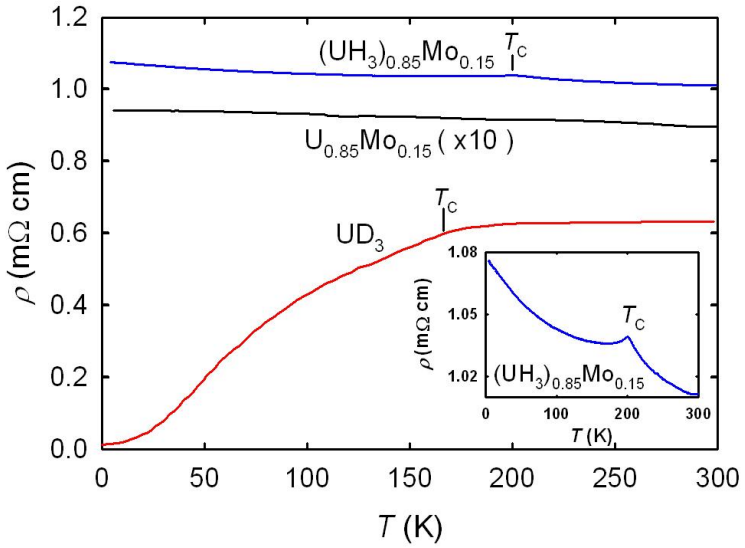

Figure 6.40. Temperature dependence of electrical resistivity of $(UH_3)_{0.85}Mo_{0.15}$ compared with the $U_{0.85}Mo_{0.15}$ (U-15 at.% Mo) splat alloy (data is multiplied by the factor of 10) and the data for UD_3 (analogy to β-UH_3) taken from Ref. 77. The inset shows the cusp at T = 200 K correlating with T_C.

After the structure investigation, we performed measurements of the temperature dependence of electrical resistivity. One of the $(UH_3)_{0.85}Mo_{0.15}$ hydride lamellas 2-3 mm long was chosen for such experiment. Electrical resistivity was measured in the temperature range 4-300 K using the four-probe method. The temperature dependence of electrical resistivity, $\rho(T)$, shown in fig. 6.40, exhibits a dominant weak negative slope ($d\rho/dT < 0$) throughout the whole temperature range. Such negative slope was detected already for the γ-phase U-Mo alloys with the *bcc* structure. As pointed out above, its reason can be seen in weak localization [31], which appears under conditions of strong disorder, and which is partly suppressed by electron-phonon scattering at elevated temperatures. The additional disorder introduced by amorphization cannot contribute much, the slope remains negative, but a pronounced kink appears at T = 200 K (see fig. 6.40, inset), which has be related to magnetic ordering (Curie temperature, as seen below). Such value is approximately 25 K higher than existing literature data for β-UH_3 [22,70]. The absolute resistivity values are unusually high, exceeding 1000 μΩcm. The resistivity, which was studied for UD_3 (fig. 4.6), also reaches similar values (over 600 μΩcm) [77]. Although such value is enormously high for a system, which is still essentially metallic, its reasons

were never discussed before. Low residual resistivity indicates, that cracks, which would modify the effective geometrical factor, are nor responsible. We tend to attribute the high absolute values to reduced concentration of conduction electrons due to H absorption, and very strong spin-disorder scattering in the paramagnetic state. $\rho(T)$ for $(UH_3)_{0.85}Mo_{0.15}$ combines both trends, the weak negative slope ($d\rho/dT < 0$) like in γ-phase U-Mo alloys and very high resistivity values resembling UD_3.

The temperature dependence of magnetization $M(T)$ measured in various magnetic fields (see fig.6.41) indicates ferromagnetic ordering. T_C was determined from inflection point of low field (0.05 T) temperature dependence. That gives values in the range between 184 and 202 K for all samples. That is rather unusual, as in other documented cases (as US or UN) amorphization leads to the suppression of U-5*f* magnetism [97]. The concentration dependence (Mo concentration) of the Curie temperature for $(UH_3)_{1-x}Mo_x$ hydrides is shown in fig. 6.42. As seen, T_C increases with increasing of Mo concentration, reaching a maximum approximately at Mo concentration 0.13-0.15, then starts to decrease and the transition broadens. The highest $T_C = 202$ K was observed for $(UH_3)_{0.87}Mo_{0.13}$ and $T_C = 200$ K for $(UH_3)_{0.85}Mo_{0.15}$, which is higher than the values given for β-UH_3 [22,70]. This value agrees with the cusp at 200 K in $\rho(T)$ for $(UH_3)_{0.85}Mo_{0.15}$ (fig. 6.40). We can conclude that this anomaly corresponds to the magnetic ordering temperature.

A closer inspection of $M(T)$ in the ordered state reveals that magnetization is not smoothly increasing with decreasing T, as usual in ferromagnets, but a maximum is achieved around 45 K (clearly seen for $(UH_3)_{0.88}Mo_{0.12}$ and $(UH_3)_{0.82}Mo_{0.18}$), below which magnetization slightly decreases. One has to stress that all the T dependences were measured in the field-cooling mode. Such effect is observed not for all of our samples. We can only suggest that this effect is attributed to a high anisotropy, progressively increasing with decreasing T, which forces some of the moments, from the field direction towards easy magnetization directions. Alternatively one may consider that some antiferromagnetic components of exchange coupling (leading to non-collinear moments) develop at low temperatures, perhaps in relation with the variable U-U spacing introduced by the Mo doping. This anomaly also can be caused by some magnetic impurities with magnetic ordering temperature close to 45 K for example UO_2.

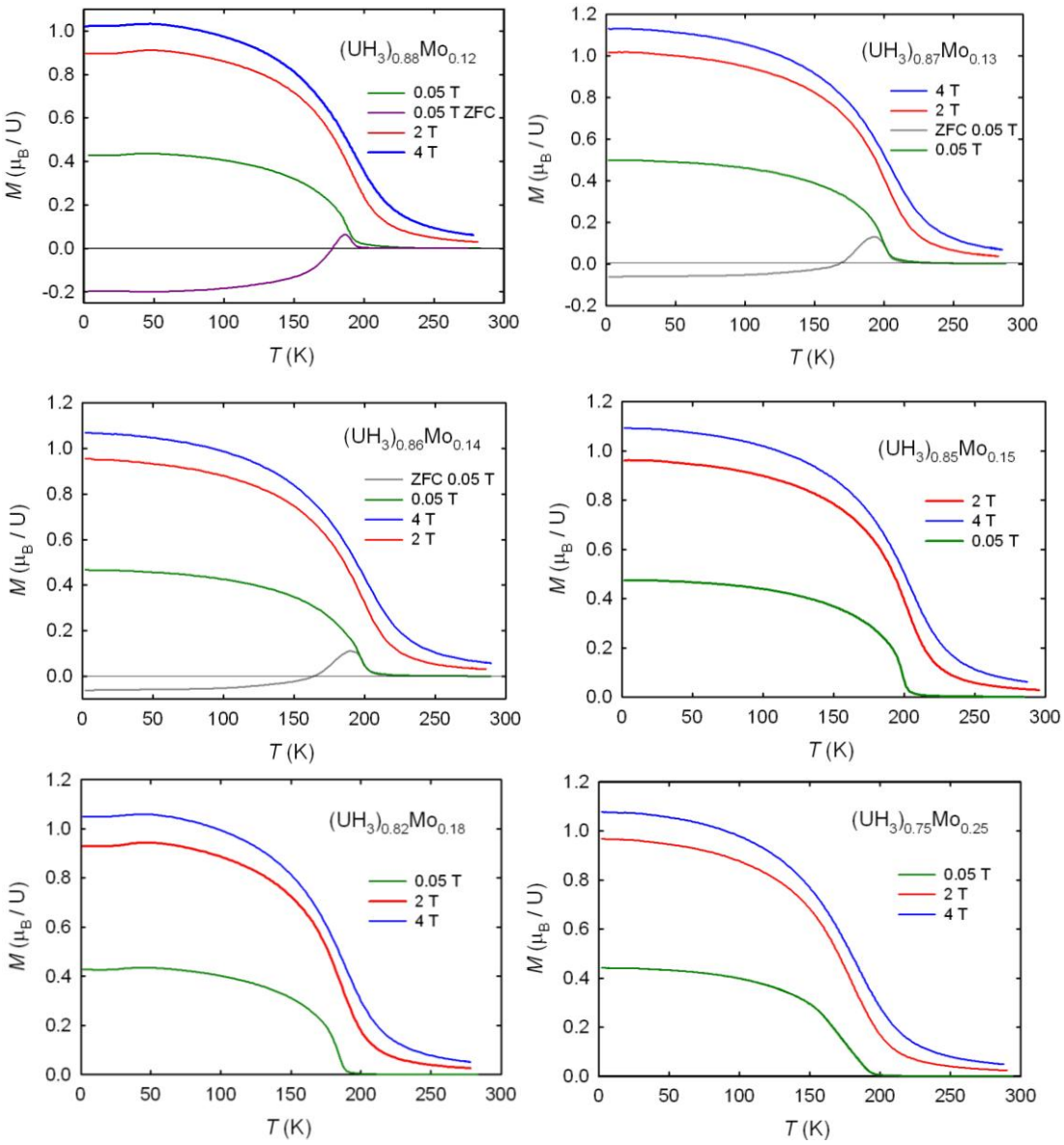

Figure 6.41. Temperature dependence of magnetization of $(UH_3)_{1-x}Mo_x$ in various magnetic fields (0.05 T; 2 T; 4 T) indicates ferromagnetic ordering with the Curie temperature 180-200 K.

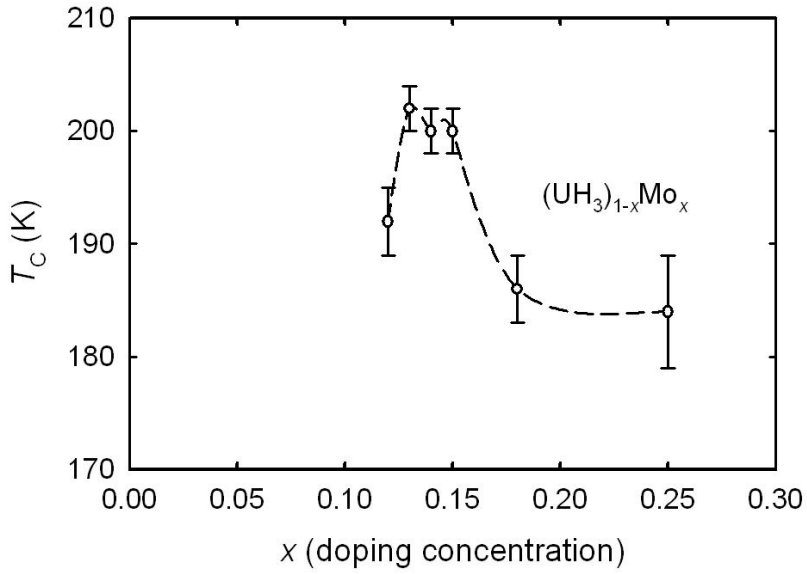

Figure 6.42. Concentration dependence of the Curie temperature for $(UH_3)_{1-x}Mo_x$ obtained from an inflection point on $M(T)$ dependence.

Using the temperature dependence of magnetization we could also determine values of the paramagnetic Curie temperature and the effective paramagnetic moments. Although the paramagnetic range is short, it does allow extracting reliable values of μ_{eff} and Θ_p, which are given in the Table 6. The values of μ_{eff} lay in the range 2.24-2.40 μ_B/U for $(UH_3)_{1-x}Mo_x$, which is in line with the data given for β-UH_3 or UD_3 [22]. The paramagnetic Curie temperature values are lay in the range 190-206 K which is 10-40 K higher than the values given for β-UH_3 or UD_3 [22].

$(UH_3)_{1-x}Mo_x$	T_C (K)	μ_{eff} (μ_B/U)	Θ_p (K)	M_s (μ_B/U)	γ_e (mJ/molU K^2)	Θ_D (K)
β-UH_3	175	2.24 [22]	176[22]	0.86 [70]	29 [98], 33.9[77]	270[98]
$(UH_3)_{0.88}Mo_{0.12}$	192	2.39	195	1.08		
$(UH_3)_{0.87}Mo_{0.13}$	202	2.44	206	1.01		
$(UH_3)_{0.85}Mo_{0.15}$	200	2.40	205	1.09	31.1	230
$(UH_3)_{0.82}Mo_{0.18}$	186	2.24	193	1.09	31.3	190
$(UH_3)_{0.75}Mo_{0.25}$	184	2.31	190	1.06	34.0	207

Table 6. Summary of magnetic and electronic properties of $(UH_3)_{1-x}Mo_x$ hydrides in comparison with β-UH_3 literature data. The value of T_C for β-UH_3 was determined by

modified Arrott plot procedure from the data given by Andreev [70]. Values of Θ_D were determined from the fit of low-temperature part of specific heat, where only U and Mo ions were considered (i.e. H vibrations were not included into the Debye model).

For a more accurate determination of the Curie temperature for $(UH_3)_{0.85}Mo_{0.15}$ and $(UH_3)_{0.75}Mo_{0.25}$ we also measured the field dependences of magnetization at various temperatures from 170 to 200 K for the Arrott plot analysis. As conventional Arrott plots are often curvilinear at such temperatures due to critical phenomena, we used the modified Arrott plots procedure, $M^{2.22}$ vs. $(\mu_0 H/M)^{0.79}$ [99], which gives a more linear dependence. For comparison, we used also the same procedure for data of β-UH_3 from Ref. 70 (fig. 6.43, left). This method gave T_C = 197.3 K for $(UH_3)_{0.85}Mo_{0.15}$, which is about 22 K higher than for β-UH_3 (see fig. 6.43). The same procedure gives T_C = 177 K for $(UH_3)_{0.75}Mo_{0.25}$ hydride.

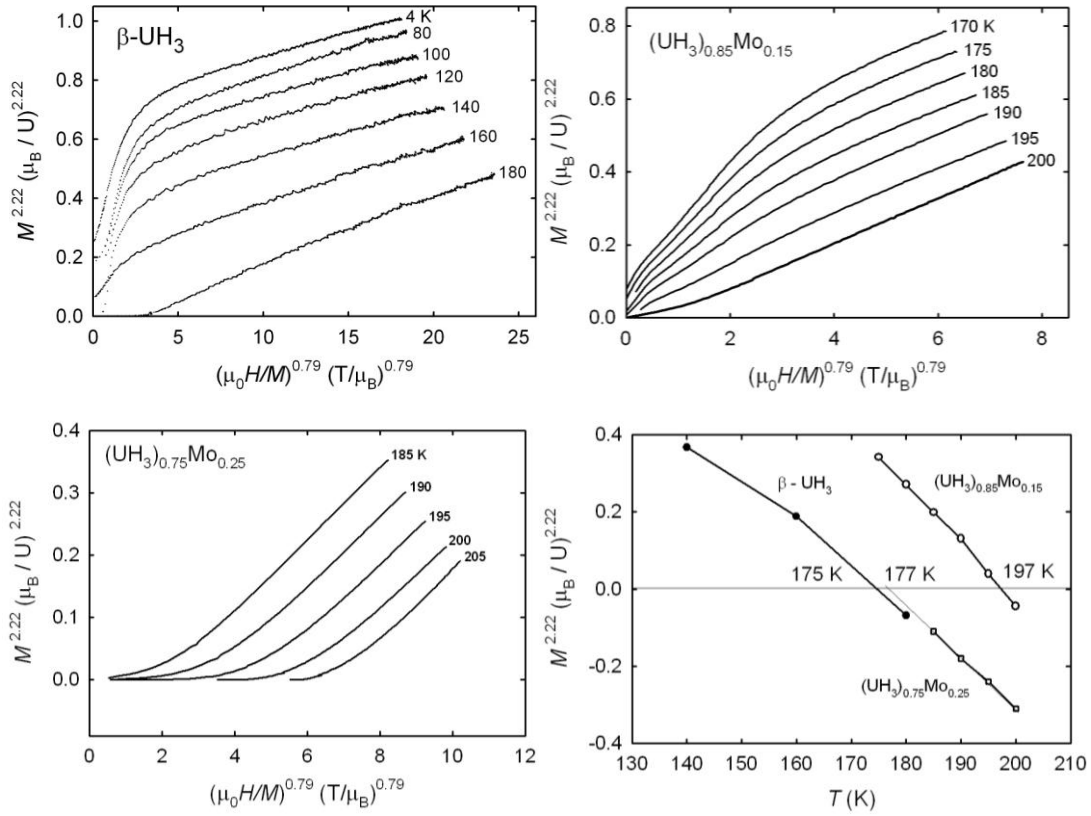

Figure 6.43. The modified Arrott plots ($M^{2.22}$ vs. $(\mu_0 H/M)^{0.79}$) for β-UH_3 [70], $(UH_3)_{0.85}Mo_{0.15}$ and $(UH_3)_{0.75}Mo_{0.25}$ and determination of the Curie temperatures.

Besides enhanced T_C, also the U moments are higher, reaching approximately 1.1 μ_B/U. Presence of magnetic moment on Mo atoms is very unlikely in metallic environment, so we observe enhancement of magnetic parameters due to doping of non-magnetic atoms. Such somewhat unusual situation can be explained by the influence on the 5*f* bandwidth by enhancing the separation of U atoms due to Mo atoms. Such mechanism can however work only to some extent.

Fig. 6.44 displays hysteresis loops at selected temperatures. With temperature decreasing down to 3-6 K the coercive field strongly increases and reaches its maximum value approximately 3.5-4 T. The highest coercive field was observed for the sample with the highest Mo concentration ($(UH_3)_{0.75}Mo_{0.25}$). The character of the hysteresis loops is changed at lower temperatures (T < 3 K). An abrupt single (in most of cases) and reproducible jump appears between 3.0-4.0 T, which is followed by another more smooth increase in still higher fields.

5*f* ferromagnets frequently exhibit large coercivity, which is conventionally related to pinning (to defects) of narrow domain walls, which can have, due to very strong magnetic anisotropy, thickness of several interatomic distances only. (More on anisotropy in the next section dealing with U-Zr hydrides.) In amorphous or other highly disordered systems the picture is modified by random distribution of local easy-magnetization directions (i.e. the ferromagnets become non-collinear). As we do not have any analogous amorphous strong ferromagnets among U compounds, we can look for analogies elsewhere. Our amorphous U-based hydrides have magnetization loops very similar to so called HARD (High Anisotropy Random Distribution) materials, which are amorphous substances e.g. on the basis of $SmCo_5$ [100]. Here Sm contributes by high anisotropy provided by Crystal Electric Field mechanism

A remarkable fact is certain asymmetry of the loop, best seen at $(UH_3)_{0.75}Mo_{0.25}$. One can notice that the sudden re-magnetization at T = 2 K occurs in low fields on the negative field side than on the positive side. In this case the coercivity apparently decreases with decreasing temperature. The reason can be seen perhaps in the range of the reach of exchange interaction decreasing with temperature. At low T, an avalanche of remagnetization triggered can be triggered by any local process and affects whole volume.

The virgin curve, recorder for T = 2 K, reaches beyond the branch corresponding to sweeping field from negative to positive, crossing it around 4 T field. Such effects can be tentatively attributed to accommodation of structure details to magnetization induced first to positive fields, which also contribute to the asymmetry, mimicking an exchange bias effect

The magnetization behavior in still higher fields is almost reversible, which means that there is either additional rotation towards the field direction or there is a pronounced development of the size of magnetic moments (suppression of longitudinal spin fluctuations), or both effects. The high magnetic anisotropy itself is not exceptional among U compounds. It is due to large orbital moments (due to strong spin-orbit interaction) even in itinerant magnets, and involvement of the 5*f*-5*f* bonding between nearest neighbors [101].

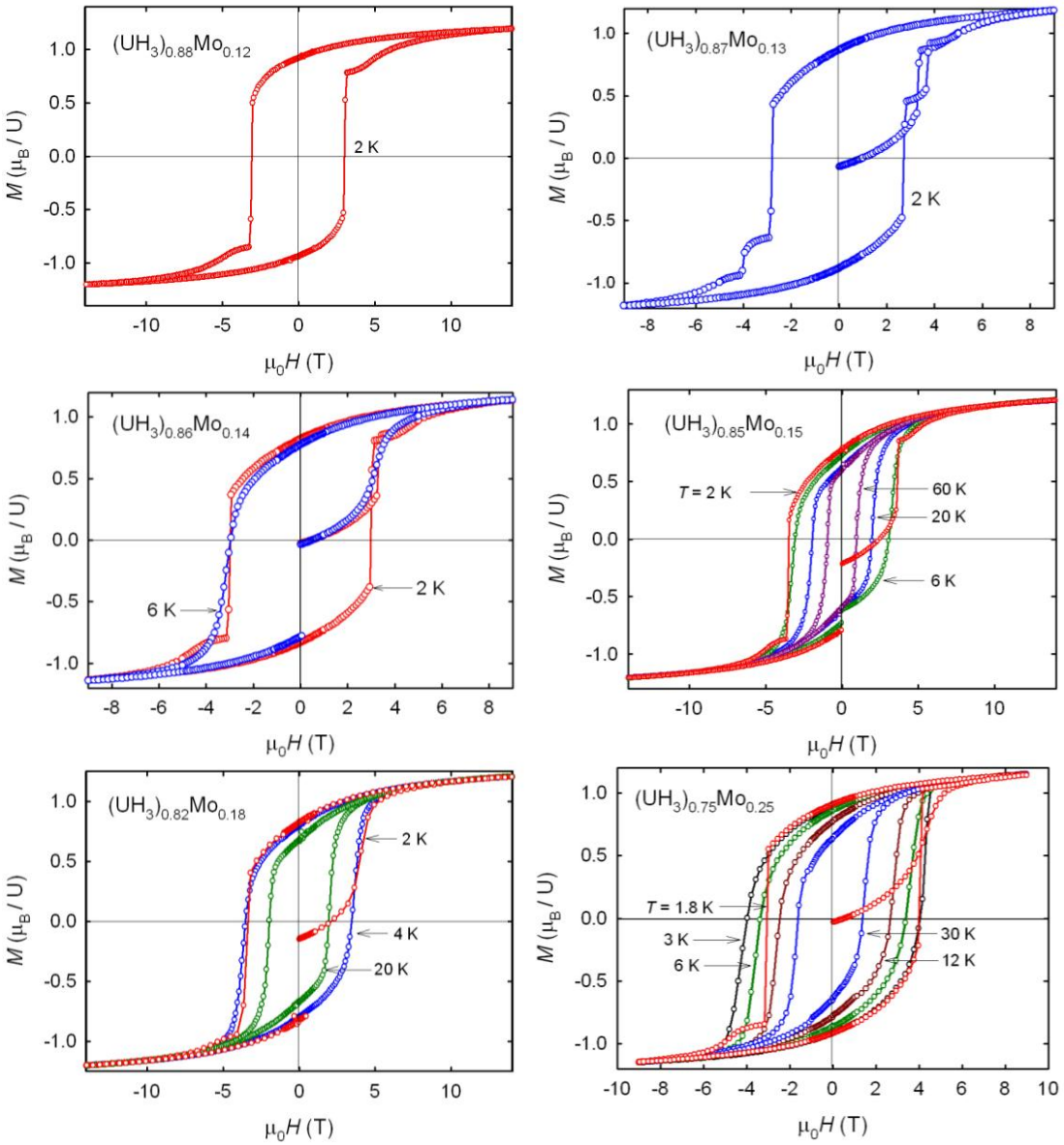

Figure 6.44. Hysteresis loops of $(UH_3)_{1-x}Mo_x$ measured at various temperatures. The negative magnetization, at which the virgin curve starts, could have been imposed by cooling in weak residual negative field of the superconducting coil.

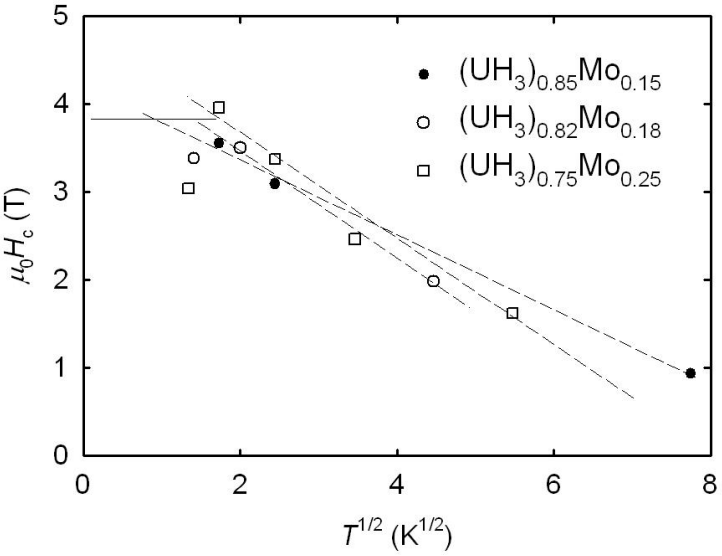

Figure 6.45. Values of the coercive field for the $(UH_3)_{1-x}Mo_x$ samples obtained from the hysteresis loops follow the scaling of the 1- $\eta T^{1/2}$ type in the high-T part.

The coercive field (fig. 6.45) decrease with temperature and follows the $-aT^{1/2}$ dependence deduced by Egami model of thermally activated movements of domain walls [102,103]. We did not observe any saturation at low temperatures predicted by Egami model. The coercive field even decrease at low temperatures.

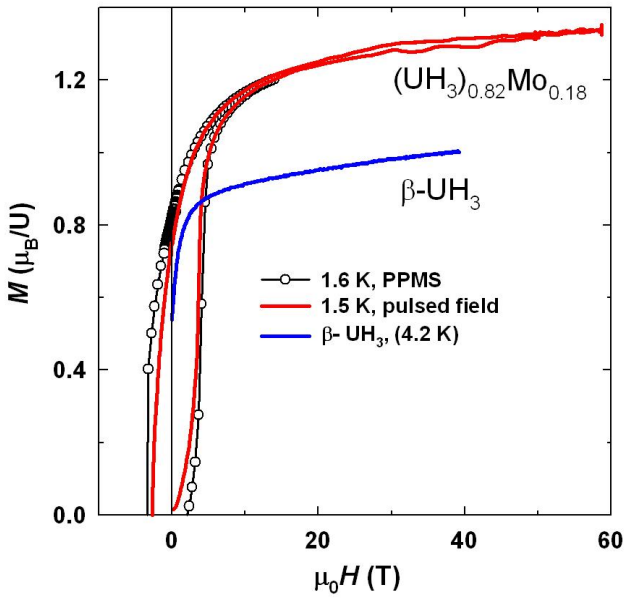

Figure 6.46. Magnetization curve of $(UH_3)_{0.82}Mo_{0.18}$ from a pulsed-field facility (red line) and static-field measurement (empty circles), compared with high-field measurement of β-UH_3 [70].

We also performed a measurement for $(UH_3)_{0.82}Mo_{0.18}$ in high pulsed-field (up to 60 T), as the magnetization of our samples does not reach saturation in magnetic fields up to 14 T. Figure 6.46 shows results of this measurement. Magnetization still not reached saturation even in magnetic field 60 T. Comparing to the size of spontaneous magnetization of β-UH_3 (0.86 μ_B/U at 4 K) [70], $(UH_3)_{0.82}Mo_{0.18}$ has the values undoubtedly higher. However, it is not easy to determine a more exact value. The high anisotropy randomly distributed almost on atomic scale leads effectively to a non-collinear ferromagnetism. Aligning the moments by the brute force of high external magnetic field leads presumably to the enhancement of the size of moments by the field. Nevertheless we can make a rough estimate of the spontaneous magnetization as corresponding to $\mu_U \approx 1.0$ μ_B for our hydride samples.

From the field dependence (up to 14 T) at T = 2 K, an estimate of the saturated moment can be done assuming a phenomenological relation $M(H)=M_s[1-a/H^2]+\chi_{hf} H$, where the second term is accounting for the influence of field on the size of individual moments, while the first accounts for the anisotropy. The values of M_s obtained for $(UH_3)_{1-x}Mo_x$ samples 1.06-1.09 μ_B/U are still far below the ionic moments (≈ 3.2 μ_B for f^2 or f^3), which is in line with the strongly itinerant magnetism of the U hydrides. One can compare with literature data on β-UH_3, exhibiting a linear dependence of magnetization in fields. The high-field measurement [70] gives the slope of magnetization χ_{hf} = 0.0028 μ_B/(U·T) for β-UH_3. Fitting the data on $(UH_3)_{1-x}Mo_x$ hydrides to the formula above yields 0.0068-0.0110 μ_B/(U·T) ($4.78\cdot10^{-8}$ – $7.74\cdot10^{-8}$ m^3/mol U).

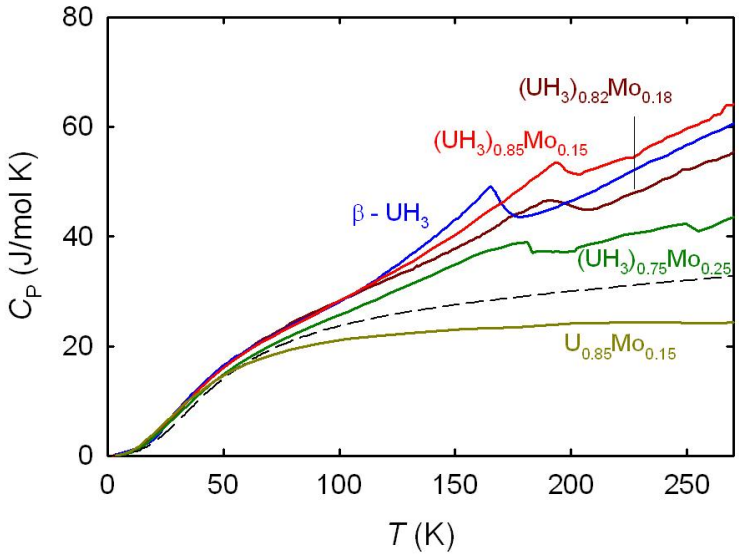

Figure 6.47. Temperature dependence of specific heat of $(UH_3)_{1-x}Mo_x$ hydrides compared with the data on β-UH_3 (from Ref. 71) and $U_{0.85}Mo_{0.15}$ splat sample. The dashed curve shows specific heat temperature dependence calculated by the Debye function (θ_D = 200 K) with addition of electronic contribution (γ_e = 31 mJ/mol K^2).

Also the temperature dependence of specific heat of $(UH_3)_{1-x}Mo_x$ demonstrates that T_C is shifted towards higher temperatures in comparison with β-UH_3 [71] (see fig. 6.47), reaching approximately 190-200 K, and exhibiting some broadening, especially for samples with high Mo concentration. That may indicate certain T_C distribution between grains due to disorder and amorphous structure of our samples. One can also expect a difference in critical behavior in a system with a high anisotropy of a random type.

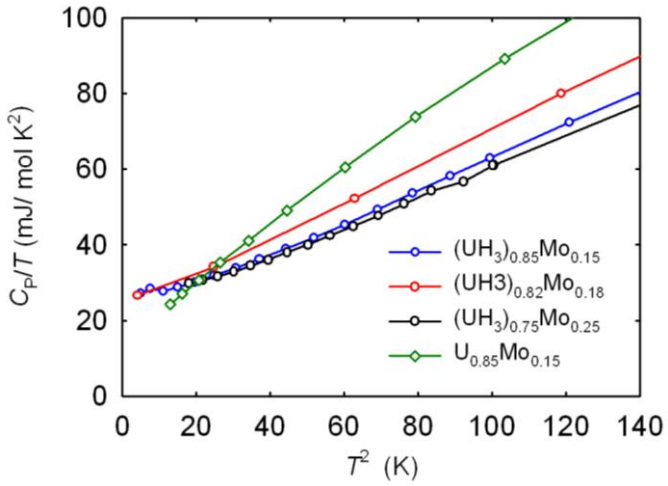

Figure 6.48. Temperature dependence of the specific heat of $(UH_3)_{1-x}Mo_x$ hydrides in the C_P/T vs. T^2 representation in comparison with $U_{0.85}Mo_{0.15}$ splat data. The fits were used to determine γ_e and θ_D values.

The low temperature part can be approximated by the Debye model from which it is possible to estimate the Sommerfeld coefficient of the electronic specific heat. A linear fit of C_P/T vs. T^2 yields values of γ_e per 1 mol U in the range 24-30 mJ/mol U K^2. However the best fit was obtained with an additional contribution to specific heat $C = \gamma T + \beta T^3 + \alpha T^{1/2} \exp(-T_0/T)$, where the last term accounts for magnons with the gap energy $k_B T_0$, which is the measure for the magnetic anisotropy energy per one U ion. This fit yields γ_e values in the range 31.1-34.0 mJ/mol U K^2 and T_0 values 30-37 K. These values are in a good agreement with part of literature data for β-UH_3 (29 mJ/mol U K^2 [98]) and for UD_3 [77] (33.9 mJ/mol U K^2). It is approximately 3 times higher than for α-U and 1.5 times higher than for γ-U (splat sample $U_{0.85}Mo_{0.15}$ has γ_e = 16.0 mJ/mol K, which corresponds to 18.8 mJ/mol U K^2 using the formula $UMo_{0.18}$).

The increase of γ_e for hydrides with respect to initial splat samples (as example fig. 6.48, $U_{0.85}Mo_{0.15}$) indicates an increase of $N(E_F)$, which can be attributed to the enhancement of the U-U spacing and consequent narrowing the 5*f* band. Values of Θ_D were also determined from the fit of low-temperature part of specific heat, where $\beta = 1944/\Theta_D^3$ for C_p in J/mol K divided by number of atoms in 1 mole. In our calculation only U and Mo ions were considered without hydrogen atoms, as it was determined for β-UH_3 in Ref. 98. Values of Θ_D are in the range 190-230 K for $(UH_3)_{1-x}Mo_x$, which is lower than that given in Ref. 98 for β-UH_3 (270 K). Ref. 77 gives value for UD_3 338 K including D atoms, which can be recalculated as 213 K without considering of D atoms. In that case our values are in good agreement with Ref. 77. If we include in consideration hydrogen atoms for $(UH_3)_{1-x}Mo_x$ samples, it will gives values of Θ_D in the range 290-350 K.

Using values from low-temperature fit (θ_D = 200 K (without consideration of H atoms); γ_e = 31 mJ/mol K^2), we calculate the *T* dependence of specific heat based on the Debye function with addition of electronic contribution, which is shown by the dashed curve in fig. 6.47. It can be seen that at low temperatures this dependence is

in a good agreement with experimental data for hydrides, as well as for initial alloys ($U_{0.85}Mo_{0.15}$), up to ≈ 70 K, where the curve exhibits an inflection. The similarity of the low-T part gives an alternative view of the lattice specific heat. The low-lying phonon modes (acoustic) are similar for the alloys and hydrides. The vibrations related to H atoms are characterized as high energy optical modes, revealed only at higher temperatures. Those were indeed observed by neutron scattering in the energy range 80–160 meV [104]. Only after the optical modes are populated, one can reach the classical limit for specific heat $3R{\cdot}N$ (N is the number of atoms in formula unit; R is gas constant equal 8.31 J/mol K), which should be in the range 80–90 J/mol K for $(UH_3)_{1-x}Mo_x$, depending on the actual concentration of H. For UH_3, it is 99.8 J/mol K. The high energy of the optical modes is the reason why the experimental C_p values are below this limit still at T = 250 K.

6.2.2. $(UH_3)_{1-x}Zr_x$ hydrides

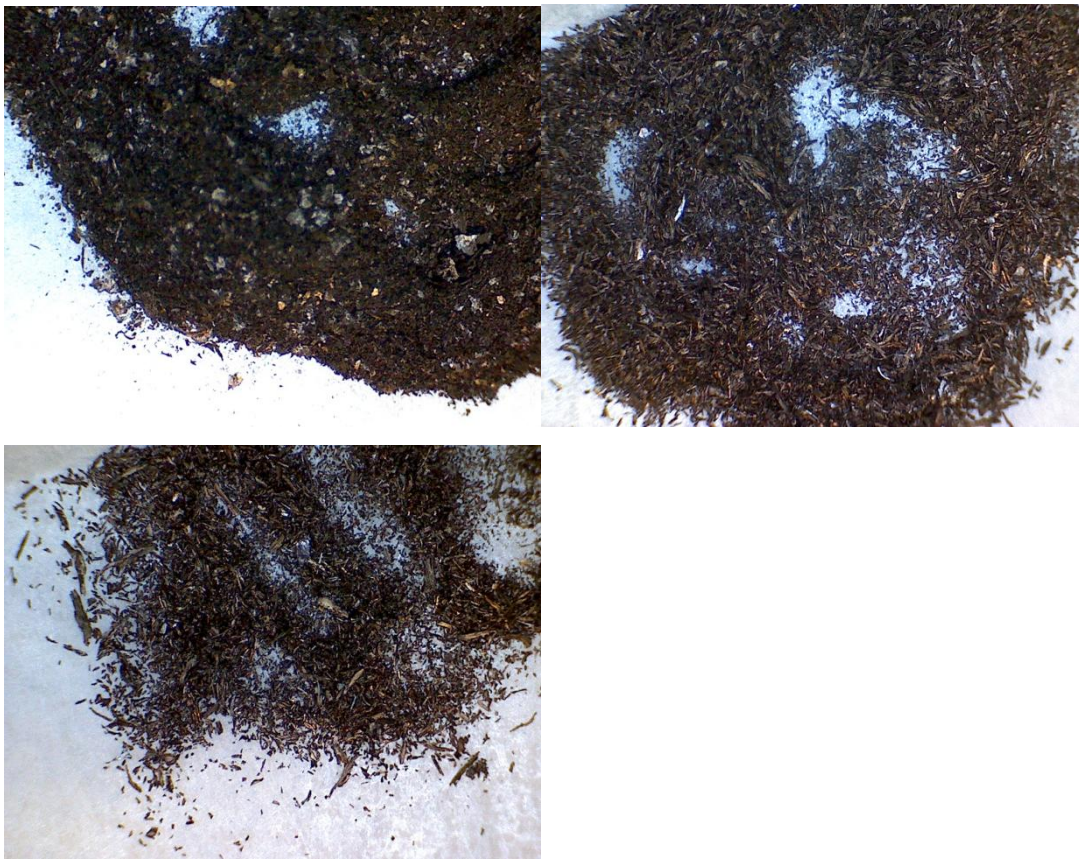

Figure 6.49. Photographs of $(UH_3)_{1-x}Zr_x$ samples (x = 0.11 (top left); 0.2 (top right); 0.3 (bottom)).

The synthesized hydrides of the $(UH_3)_{1-x}Zr_x$ type are shown in fig. 6.49. The sample with Zr concentration x = 0.11 consists of fine black powder with small metallic pieces of irregular shape. Sample with x = 0.2 form lamellas approximately 1 mm long. For x = 0.3, some of the lamellar particles can be up to 2-3 mm long. For x = 0.15 some large pieces among powder were found, which were used later for electrical resistivity measurements.

The $(UH_3)_{1-x}Zr_x$ (x =0; 0.11; 0.15; 0.2; 0.3) samples were crushed and subjected for structure characterization by X-ray powder diffraction. The diffraction patterns are presented in fig. 6.50.

As mentioned in the previous section, we observed a mixture of α- and β-UH_3 phases for the hydride prepared from pure U splat (x = 0). Irreversible changes in phase composition of our pure U hydride sample appear after approximately few months (fig. 6.31); confirming that α-UH_3 is unstable in ambient conditions. On the other hand, UO_2 peaks are more pronounced. The sample $(UH_3)_{0.89}Zr_{0.11}$ revealed only small increase of UO_2 peaks with time, but the ratio between α-UH_3 and β-UH_3 phases was not significantly changed. For samples with higher Zr concentrations no changes in phase composition was observed.

In contrast to Mo doped hydrides, XRD patterns of Zr doped hydrides show (fig. 6.50 and fig. 6.51) crystalline structure, which is very different from β-UH_3, and can be attributed to the α-UH_3 structure. The U sites in this structure correspond to the *bcc* lattice of γ-U, which is only very expanded (70% of volume expansion). The concentration of α-UH_3 phase increases with increasing of Zr concentration and the β-UH_3 phase is fast suppressed. For x = 0.15 only very small broad bumps of β-UH_3 can be seen from the XRD pattern (anyway it is nearly completely α-UH_3). For Zr concentrations over 20%, no peaks attributed to β-UH_3 can be observed. Small narrow peaks of spurious ZrC were observed of all hydrides with Zr (see fig. 6.51). As in the case of U-Zr splat samples, peaks broadening becomes more evident with increasing Zr concentration. The reasons could be seen in additional disorder by randomly distributed Zr atoms in samples. An important finding is that the α-UH_3 structure in the hydrides with higher Zr concentration is stable.

A quantitative analysis by using Rafaja model shows that XRD patterns can be reproduced by assuming nano-crystalline grains, but approximately 10 times larger than for $(UH_3)_{1-x}Mo_x$ (data listed in Table 7). The size distribution is simplified by two different characteristic sizes. The lattice parameters for all U-Zr hydrides do not vary much from the value 4.143 Å. The corresponding shortest inter-uranium distance is 3.58 Å which is above the Hill limit. So we can expect magnetic ordering for $(UH_3)_{1-x}Zr_x$ hydrides.

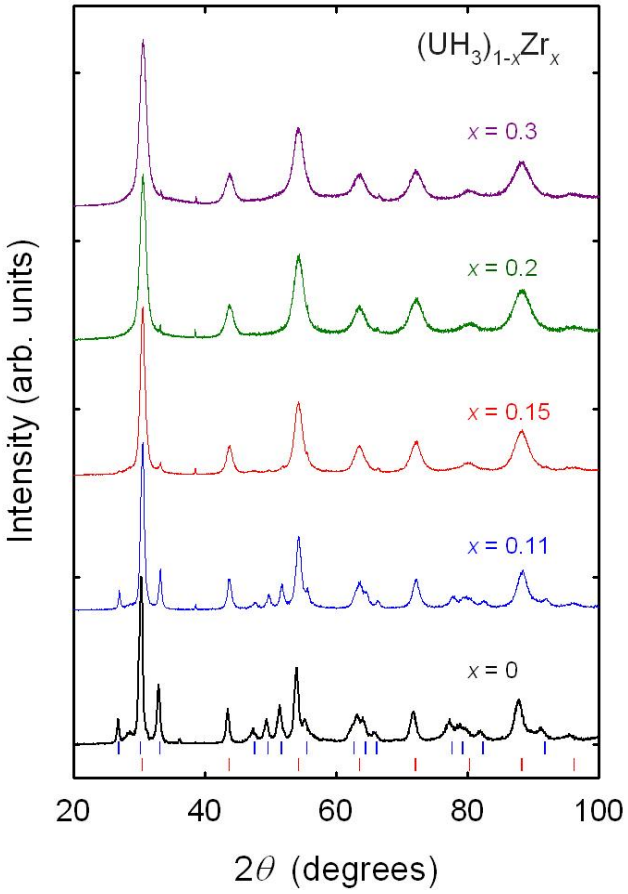

Figure 6.50. Variations of XRD pattern with varying the Zr concentration x. Pure UH_3 (x = 0) consists of both α-UH_3 (red ticks at the bottom) and β-UH_3 phase (blue ticks at the bottom). Increasing x leads to a fast suppression of the β-UH_3 phase. Tiny peaks at 33° and 38° belong to ZrC. Data obtained using the Cu-Kα radiation.

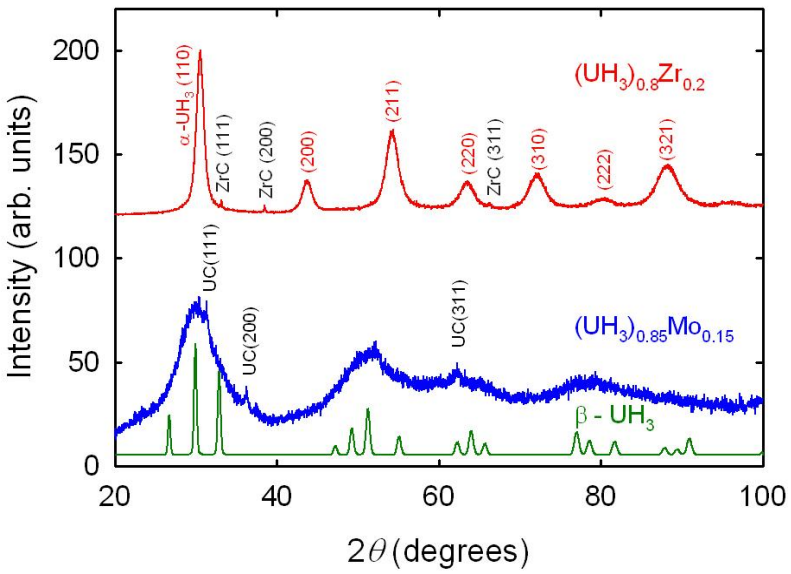

Figure 6.51. Comparison of XRD patterns for amorphous hydrides $(UH_3)_{1-x}Mo_x$ (β-UH_3 phase) and crystalline $(UH_3)_{1-x}Zr_x$ (α-UH_3 phase).

Sample	*a* (Å) (α-UH_3)	Grain 1 (nm)	Grain 2 (nm)	H/U
UH_3	4.161	61	50	
$(UH_3)_{0.89}Zr_{0.11}$	4.143	58	54	
$(UH_3)_{0.85}Zr_{0.15}$	4.143	23	8	2.8
$(UH_3)_{0.8}Zr_{0.2}$	4.142	13	1.7	2.8
$(UH_3)_{0.7}Zr_{0.3}$	4.142	14	1.7	2.9

Table 7. Summary of measured structure properties: lattice parameter, grain sizes and hydrogen concentration per formula unit for $(UH_3)_{1-x}Zr_x$ hydrides.

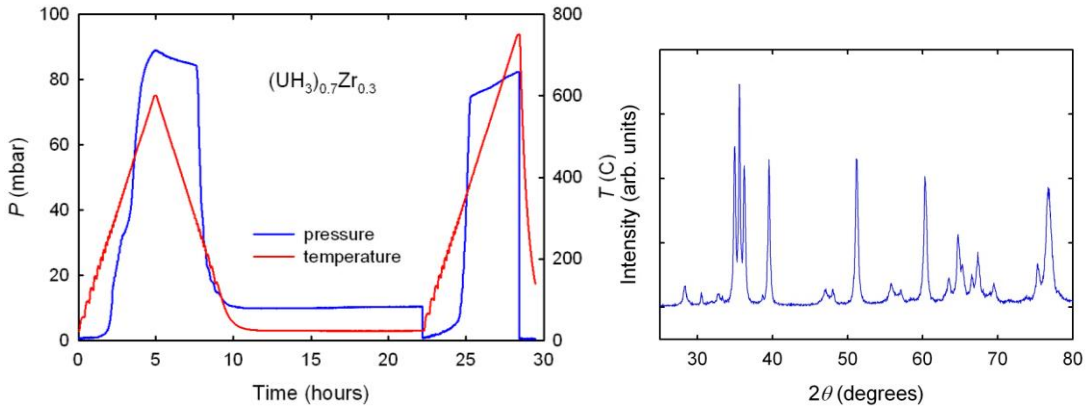

Figure 6.52. (left) Example of hydrogen desorption in 2 steps of heating with consequent reabsorption during cooling (after first step) for $(UH_3)_{0.7}Zr_{0.3}$ sample.

(right) XRD pattern after desorption of hydride indicate presence of α-U phase with no sign of γ-U phase.

Desorption in a closed evacuated volume was performed to determine the hydrogen concentration in hydrides by using the temperature ramping 2 K/min. All H is released (fig. 6.52) from hydrides already at 620 ^{o}C (893 K). Heating up to higher temperatures was also tested, which however did not yield any further H release. For hydrides with Mo all hydrogen is released after heating approximately to 470 ^{o}C (743 K), which is 150 ^{o}C lower than for hydrides with Zr. It means, probably, that the H bonding enthalpy in these two structures (α-UH_3 and β-UH_3) is different. Naturally, the difference can be due to different composition (Mo or Zr dopant) and as result different bonding energies with hydrogen. Hydride ZrH_2 is known for its high thermal stability (a maximum of the decomposition peak at 700 ^{o}C (973 K)) [105]. However, it is the invariable U:H ratio 1:3 which makes us believe that H primarily couples to U atoms in the α-UH_3 structure. Details of H distribution in random U-Zr *bcc* lattice remains currently unresolved.

We typically observed a release of hydrogen in two close steps, as earlier in the case of $(UH_3)_{1-x}Mo_x$ hydrides. The total amount of H_2 released corresponds to approximately 3 H atoms per 1 U atom. Cooling the reactor to the room temperature leads to a re-absorption of the gas, but much less than for $(UH_3)_{1-x}Mo_x$. Values of hydrogen concentration determined from desorption tests are given in Table 7. Deviations of values from the ideal UH_3 composition are within the error of technique which was used for determination. XRD pattern after desorption of hydrides indicate presence of α-U phase with no sign of γ-phase (fig. 6.52, right panel). ZrC and UO_2 impurities are also observed.

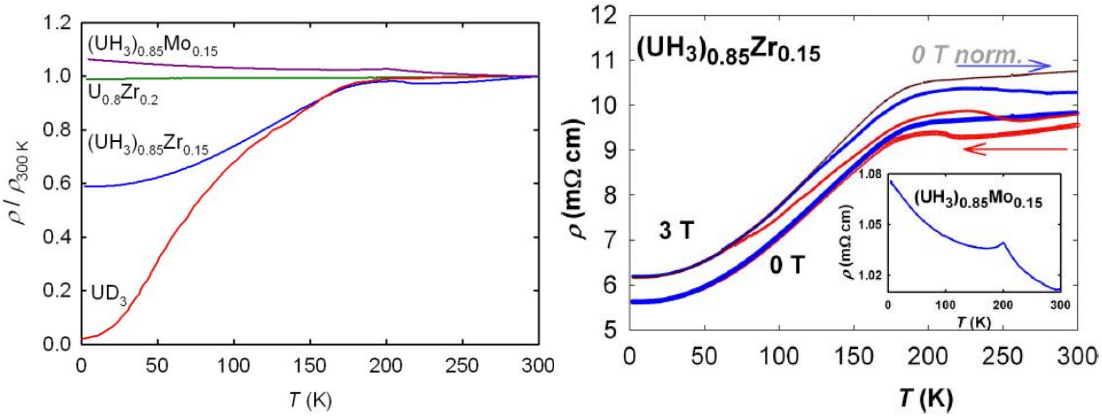

Figure 6.53. (left) Temperature dependence of electrical resistivity of $(UH_3)_{0.85}Zr_{0.15}$ compared with the $(UH_3)_{0.85}Mo_{0.15}$ hydride, $U_{0.8}Zr_{0.2}$ splat alloy and the data for UD_3 (analogy to β-UH_3) taken from Ref. 77. All resistivity curves are normalized to be equal to 1 at 300 K. (right) Temperature dependence of electrical resistivity of $(UH_3)_{0.85}Zr_{0.15}$ (in absolute values) measured when cooling down (red) and heating up (blue) in zero field (thick line) and in applied field $\mu_0 H$ = 3 T (thin line). The upper line represents the 0 T data with heating, renormalized to match the residual resistivity of the 3 T data. For comparison, resistivity data on $(UH_3)_{0.85}Mo_{0.15}$ are displayed in the inset.

After the structure investigation we perform measurements of electrical resistivity. One of the $(UH_3)_{0.85}Zr_{0.15}$ hydride pieces was used for measurements. All curves in fig. 6.53 (left) were normalized to 1 at 300 K. As was mention earlier, $(UH_3)_{0.85}Mo_{0.15}$ combines flat $\rho(T)$ with a weak negative slope with very high absolute values, about 1 mΩcm (see inset of fig. 6.53. (right)), with superimposed T_C anomaly in the form of a sharp but weak cusp, below which $\rho(T)$ resumes an increase with decreasing T . This suggests that a spin disorder contribution does not decrease below T_C, probably because the crystallographic disorder induces a strong magnetic disorder on the state characterized by bulk ferromagnetism. $(UH_3)_{0.85}Zr_{0.15}$ behaves differently. Figure 6.53 (right) demonstrates that resistivity drops below T_C with ρ_0 corresponding to 50% of the high T values. Cycling of temperature increases the resistivity value, which may be the impact of thermal expansion and spontaneous magnetostriction (will be described below), which open cracks in the brittle material, changing the effective geometrical factor. The anomaly related to T_C appears only as a knee and which is further broadened and shifted somewhat to higher temperatures

in the applied field $\mu_0 H$ = 3 T, applied when the sample was at T = 300 K. The data at magnetic field 3 T reveal a similar irreversibility due to additional cracks opening, whose character remains similar to the zero field data, as seen when comparing with the 0 T heating data, normalized to the residual resistivity of the 3 T data (upper curve in Fig. 6.53 (right)). Both data sets exhibit the quadratic T dependence of resistivity up to ≈140 K.

The temperature dependence of magnetization measured in various magnetic fields (see fig. 6.54) indicates ferromagnetic ordering with T_C values, which are very similar to β-UH_3 (despite different structure and U-U spacing) and to amorphous U-Mo hydrides, in the range between 160 and 175 K for $(UH_3)_{1-x}Zr_x$ samples. Such T_C values are lower than ones for $(UH_3)_{1-x}Mo_x$ hydrides. Magnetic moments are little bit lower than for $(UH_3)_{1-x}Mo_x$.

The feature at temperature 45 K, which was observed earlier for some of $(UH_3)_{1-x}Mo_x$ samples, was also observed for $(UH_3)_{1-x}Zr_x$. The feature is clearly seen for $(UH_3)_{0.8}Zr_{0.2}$ sample. The reason of this feature is not clear. We can only suggest that this effect is attributed to a high anisotropy, progressively increasing with decreasing T, which forces some of the moments, from the field direction towards easy magnetization directions. Alternatively one may consider that some antiferromagnetic components of exchange coupling (leading to non-collinear moments) develop at low temperatures, perhaps in relation with the variable U-U spacing introduced by the Mo doping. This anomaly also can be caused by some magnetic impurities with magnetic ordering temperature close to 45 K for example UO_2.

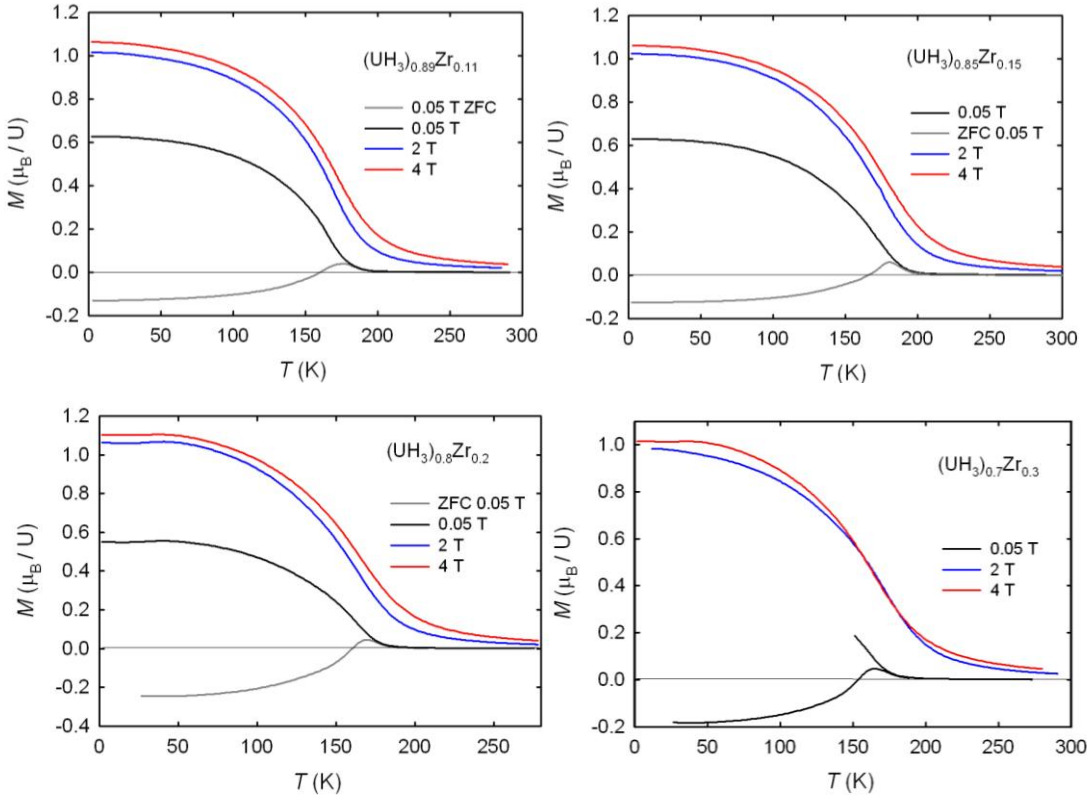

Figure 6.54. Temperature dependence of magnetization in $(UH_3)_{1-x}Zr_x$ hydrides measured in various magnetic fields (0.05 T; 2 T; 4 T) indicates ferromagnetic ordering with the Curie temperature 160-175 K.

The concentration dependence (Zr concentration) of the Curie temperature for the $(UH_3)_{1-x}Zr_x$ series (fig. 6.55) is remarkably similar to $(UH_3)_{1-x}Mo_x$, with a maximum for Mo concentrations in the range near x = 0.13-0.15. Considering the structure and chemical differences, the similarity is truly amazing.

The dilution of the active magnetic sublattice leads typically to a broadening of the transition, as seen in magnetization. For low Zr concentrations it is the two-phase nature which can also produce a broadening. The result is the relatively large error bars displayed on fig. 6.55. We can, however, conclude a relatively slow decrease of T_C for high concentrations, which is different than effects of the 5*f* dilution in regular band U-based ferromagnets, as e.g. U(Th,Lu)RhAl, in which the long-range order vanishes entirely for 15% Lu or 35% Th (the difference between the two is likely a volume effect related to much large Th atoms) [106].

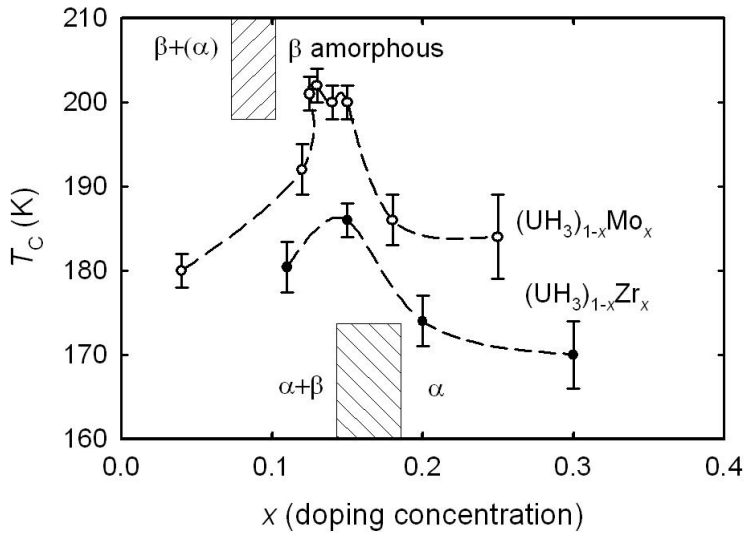

Figure 6.55. Concentration dependence of the Curie temperature for $(UH_3)_{1-x}Zr_x$ hydrides in comparison with $(UH_3)_{1-x}Mo_x$ hydrides. Transitional concentrations x (for $(UH_3)_{1-x}Mo_x$ between β+α and amorphous β; for $(UH_3)_{1-x}Zr_x$ between α+β and β phases) are shown by dashed rectangles.

Here a reader should be reminded that the sample with Zr concentration x = 0.11 contains both α-UH_3 and β-UH_3 phases (α-UH_3 is dominates). That can describe high value of T_C for this sample which is very close to the literature values for β-UH_3. T_C values (data listed in Table 8) for samples with Zr concentration x = 0.2 and x = 0.3 are lower, close to each other and can be attributed only to α-UH_3 phase.

From the temperature dependence of magnetization we also deduced values of the paramagnetic Curie temperature and the effective paramagnetic moment for our samples. The extracted values of μ_{eff} and Θ_p are given in the Table 8. Value of μ_{eff} lay in the range 2.13-2.22 μ_B/U for $(UH_3)_{1-x}Zr_x$, which is in line with the data given for $(UH_3)_{1-x}Mo_x$ samples and β-UH_3 [22]. Paramagnetic Curie temperature values are close to 180 K for α-UH_3 phase samples which is 10-25 K lower than the values given for $(UH_3)_{1-x}Mo_x$ samples. These values are still very close to that for β-UH_3. As magnetic properties are very close to each other for α-phase and β-phase of hydride it seems impossible to distinguish magnetism of these phases for mixed phase samples.

For a more accurate determination of the Curie temperature for $(UH_3)_{0.7}Zr_{0.3}$ sample we also measured the field dependences of magnetization (fig. 6.56) at various temperatures from 140 to 185 K for the Arrott plot analysis. As conventional Arrott plots are often curvilinear at such temperatures due to critical phenomena, we used the modified Arrott plots procedure, $M^{2.22}$ vs. $(\mu_0 H/M)^{0.79}$ [99], which gives a more linear dependence. This method gave T_C = 163 K for $(UH_3)_{0.7}Zr_{0.3}$, which is approximately 10 K lower than for β-UH_3 but still very close.

$(UH_3)_{1-x}Zr_x$	T_C (K)	μ_{eff} (μ_B/U)	Θ_p (K)	M_s (μ_B/U)	γ_e (mJ/molU K^2)	Θ_D (K)
β-UH_3	175	2.24 [22]	176 [22]	0.86 [70]	29[98], 33.9[77]	270[98]
$(UH_3)_{0.89}Zr_{0.11}$	180	2.18	177	1.03	31.4	195
$(UH_3)_{0.85}Zr_{0.15}$	186	2.24	187	0.90		
$(UH_3)_{0.8}Zr_{0.2}$	174	2.13	181	1.02	32.2	186
$(UH_3)_{0.7}Zr_{0.3}$	170	2.22	184	0.89	≈ 34	≈ 210

Table 8. Summary of magnetic and electronic properties of $(UH_3)_{1-x}Zr_x$ hydrides in comparison with β-UH_3 literature data.

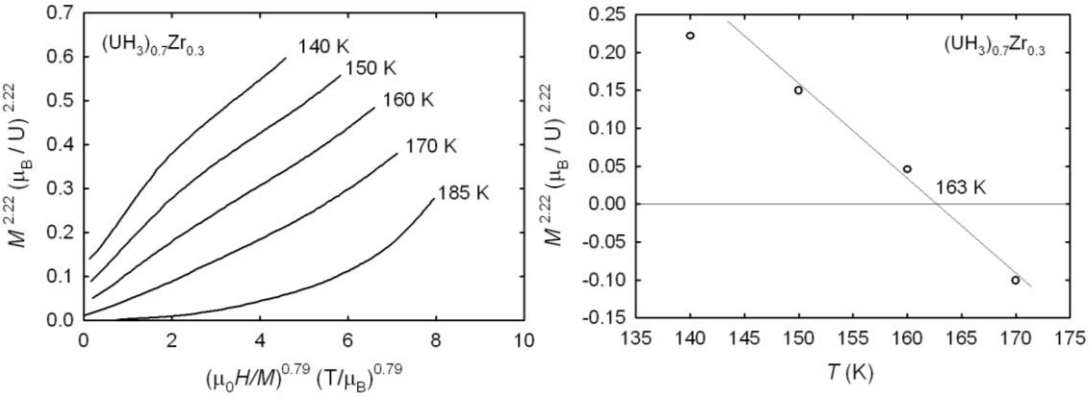

Figure 6.56. The modified Arrott plots ($M^{2.22}$ vs. $(\mu_0 H/M)^{0.79}$) for $(UH_3)_{0.7}Zr_{0.3}$ from which the Curie temperature was determined to be equal 163 K.

Fig. 6.57 displays hysteresis loops at selected temperatures. The behavior of magnetization field dependence is similar to that was observed for $(UH_3)_{1-x}Mo_x$ hydrides. The hysteresis loops are wide and the coercive field increases with decreasing *T*. At temperatures below 6 K the coercive field is reaches its maximum

values up to 4.7-5.9 T. Such values are even higher than for the $(UH_3)_{1-x}Mo_x$ series. The coercive field also increases with concentration of Zr. At temperatures below 3 K, the character of the hysteresis loops changes. Reproducible Barkhausen-type jumps (i.e. not single jump as in $(UH_3)_{1-x}Mo_x$) appear between 3.0-5.9 T. Jumps are not followed by another more smooth increase in still higher fields as it was in case of $(UH_3)_{1-x}Mo_x$ hydrides. Such a behavior can be associated with pinning of domain walls in highly disordered systems with high anisotropy. There exists extended evidence of similar behavior among such materials, labeled as HARD (High Anisotropy Random Distribution).

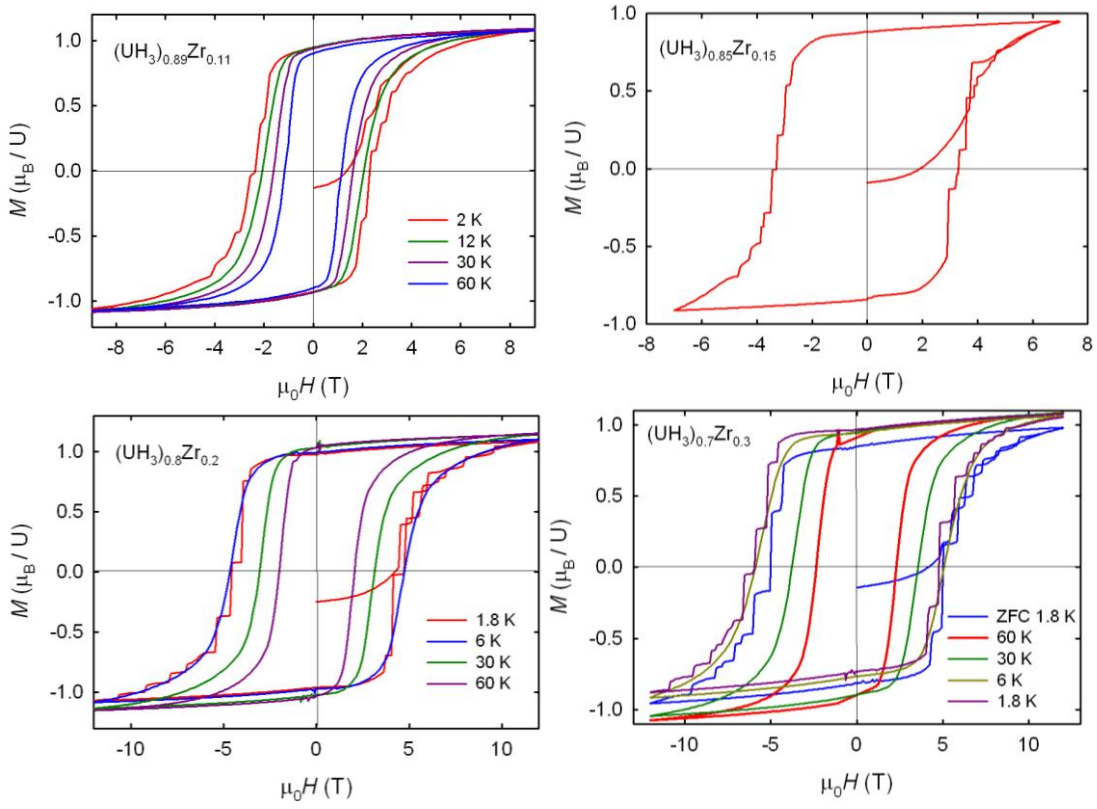

Figure 6.57. Field dependence of $(UH_3)_{1-x}Zr_x$ hydrides magnetization measured at various temperatures. Left bottom panel shows details of the hysteresis loops of $(UH_3)_{0.8}Zr_{0.2}$ in high magnetic field, illustrating the decrease of magnetization with decreasing *T*.

Slow saturation of *M*(*H*) dependences makes also the derived values of spontaneous moments less accurate than usual. From the field dependence (up to 14 T) at *T* = 1.8 K, an estimate of the saturated moment can be done assuming a

phenomenological relation $M(H)=M_s[1-a/H^2]+\chi_{hf}H$, where the second term is accounting for the influence of field on the size of individual moments, while the first accounts for the anisotropy. The values obtained shown in Table 8 are similar to β-UH_3 (with approx. 0.9 μ_B/U) and somewhat smaller than those which can be reached in $(UH_3)_{1-x}Mo_x$ (M_s = 1.09 μ_B/U in $(UH_3)_{0.85}Mo_{0.15}$). All these values are therefore quite similar and far below the ionic moments (≈ 3.2 μ_B for f^2 or f^3), which is in line with the strongly itinerant magnetism of the U hydrides. One has to keep in mind that both spin and orbital components of total moments can differ from the free-ion prediction while they tend to orient antiparallel to each other in U compounds.

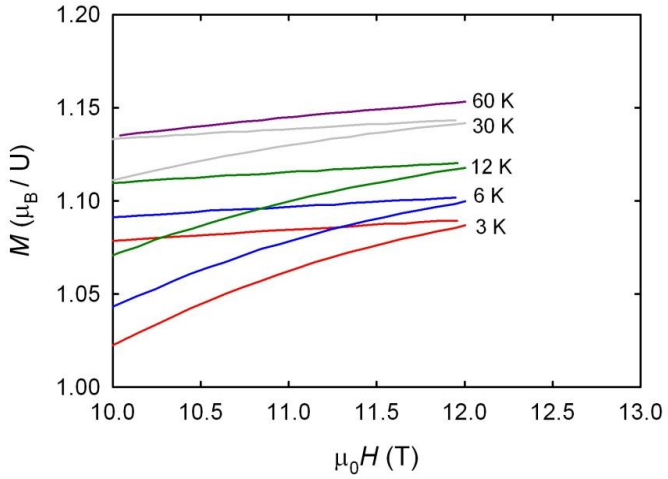

Figure 6.58. Details of the hysteresis loops of $(UH_3)_{0.8}Zr_{0.2}$ in high magnetic field, illustrating the decrease of magnetization with decreasing *T*.

The weak decrease of magnetization for the same sample with decreasing *T* can be observed on hysteresis loops (fig. 6.58), using the field sweeping rate 0.0045 T/s in the range -1 T to 1 T and 0.009 T/s outside this range. In particular, the loops do not reach the absolutely reversible behavior even in μ_0H = 12 T. At this stage we can only speculate about details of magnetization processes. The field range of fastest demagnetization (4-5 T) reflects most likely movements of domain walls. The domain wall pinning is responsible for magnetization jumps observable at the lowest temperatures (1.8 and 3 K). Their smearing at higher *T* reflects relatively easy thermally assisted depinning of domain walls. In any case, such pinning can happen in a situation of very narrow domain walls, i.e. for high magnetocrystalline anisotropy. The pinning mechanism may not be related to structure defects. As

shown e.g. for rare-earth compounds with transition metals, randomness on the transition-metal sublattice with relatively small magnetic moments yields a fundamental coercivity due to fluctuations of exchange interactions or anisotropy, which stabilize domain walls in given positions. The coercive field (fig. 6.59) decrease follows the $-aT^{1/2}$ dependence deduced by Egami model of thermally activated movements of domain walls [102]. Similar to the Egami model it deviates from this dependence and saturates at low temperatures. One should notice that the smooth demagnetization curve turns into large erratic steps, corresponding to re-magnetization avalanches. We use this word for stressing a kinetic effect, leading to a faster demagnetization even if T is lower when the avalanche is triggered comparing to somewhat higher temperatures with smooth thermally assisted motion.

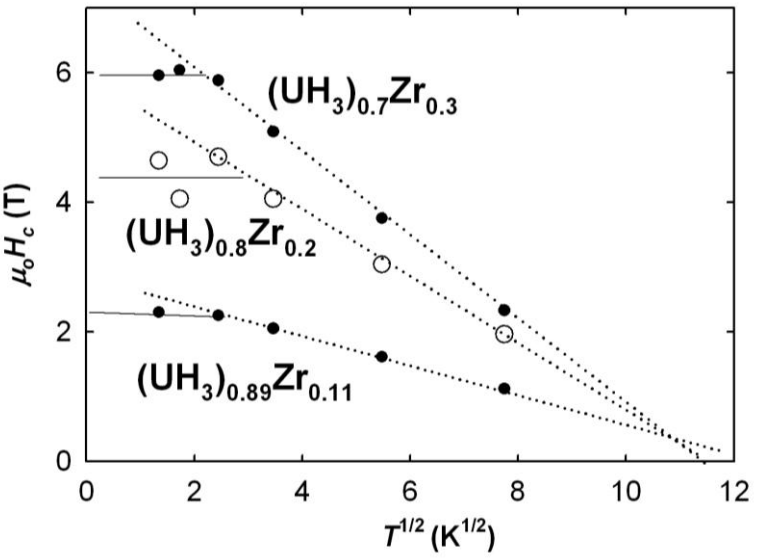

Figure 6.59. Values of the coercive field for the $(UH_3)_{1-x}Zr_x$ samples obtained from the hysteresis loops follow the scaling of the 1- $\eta T^{1/2}$ type in the high-T part.

Although the phenomenology is very similar e.g. to $SmCo_{1.4}Ni_{3.6}$ [107], in the U-Zr hydrides we consider the dilution of the U sublattice by Zr introducing "defects" in exchange interaction and/or anisotropy. The most essential prerequisite of the model, the large anisotropy, is inherent to 5*f* itinerant systems. The strong magnetic anisotropy is traditionally associated with crystal-field phenomena of localized 4*f* states in lanthanides. In light actinides, where the 5*f* states are part of metal bonding, and strong spin-orbit interaction induces large orbital moments, the anisotropy of different type is encountered, which is related to the directionality of

the 5*f*-5*f* bonding. This so-called two-ion anisotropy, the energy can be of the order of several hundred Kelvin, is particularly noticeable in low-symmetry structures [108], but can be expected even in cubic materials. The central idea is that when the involvement of the 5*f* into bonding is directional it leads to population of the 5*f* states with orbital moments perpendicular to the strong bonding directions. Working of such anisotropy mechanism was deduced from the moments directions even for weak ferromagnets with $d_{U\text{-}U}$ far below the Hill limit, as UNi_2 or U_2Fe_3Ge [109].

The magnetic hardness even increase with more Zr doping, reaching $\mu_o H_c$ = 6 T for $(UH_3)_{0.7}Zr_{0.3}$. The *T* dependence type remains the same. Using the relation $H_c(T)/H_c(0) = 1 - \eta T^{1/2}$ [107] we obtain the same value of η = 0.082 $K^{-1/2}$ for both Zr concentrations (*x* = 0.2; 0.3). As seen from fig. 6.59, the two-phase hydride with $(UH_3)_{0.89}Zr_{0.11}$ has the η-value smaller.

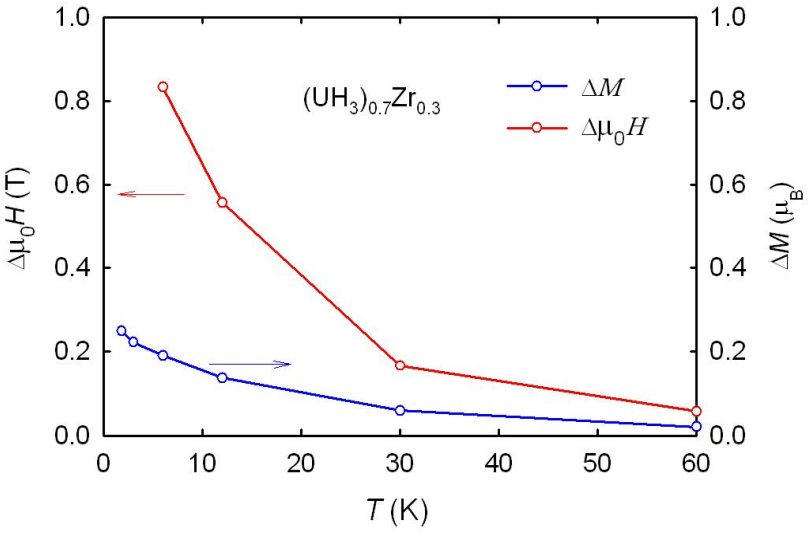

Figure 6.60. The temperature dependence of exchange bias effect for $(UH_3)_{0.7}Zr_{0.3}$ sample. Hysteresis loops are shifted with decrease of temperature in both horizontal ($\Delta\mu_0 H$) and vertical (ΔM) directions.

As also possible to see from fig. 6.57 and, magnetization hysteresis loops are not absolutely symmetric for *x* = 0.2; 0.3 and shifted alongside both magnetic field axis and magnetic moment axis. Such shifts increase with Zr content and reach a maximal values for $(UH_3)_{0.7}Zr_{0.3}$ (fig. 6.60).This behavior could be assigned to a sort of exchange bias effect. The exchange-bias effect in its pure form appears at an interface of ferro- and antiferromagnet, where one orientation of ferromagnet is preferred over another, and it comes from biasing due to mutual exchange interaction.

The antiferromagnet is not primarily affected by field but holds the ferromagnet by exchange interaction. Besides artificial structures (sandwiches) it was observed in numerous multiphase systems.

The performed XRD analysis did not reveal any foreign phases that could be antiferromagnetic, e.g. UO_2, within the resolution limits of the method. We also can suggest that UO_2 can be in amorphous form, which is not possible to see from the XRD experiment. We should mention that UO_2 phase was observed for initial splats from which were made U-Zr hydrides. If the material contains some small clusters of oxidized uranium, the exchange interaction through the interface between an antiferromagnetic UO_2 and ferromagnetic α-UH_3 could create exchange bias effect when a material was field cooled from room temperature down to 1.8 K (see fig. 6.57). "Not biased" hysteresis loop measured after zero field cooling (ZFC), which is symmetric, supports the hypothesis of presence of additional phase within the bulk material. In addition, all effects – horizontal and vertical shifts of the hysteresis loops gradually disappear (fig. 6.60) above approximately 30 K. This correlates with the temperature dependence of the magnetization $(UH_3)_{1-x}Zr_x$, which shows a shallow dip below approximately 30 K. In our case of $(UH_3)_{1-x}Zr_x$ the blocking temperature is virtually equal to the bulk Néel temperature of UO_2 is 30.8 K [110].

Vertical shift of hysteresis loop is related to the number of pinned spins [111], the larger the shift is the more spins is involved in the effect. 20% percents of the vertical hysteresis shift implies that there could be some amount of an antiferromagnetic phase. We also cannot exclude that antiferromagnetic interactions can be introduced by the Zr alloying, which are difficult to identify due to enormous coercivity. In such situation it is impossible to distinguish metamagnetic processes from remagnetization processes. Finally we may see a possible link with the weak decrease of magnetization observed in some cases below $\approx$ 50 K.

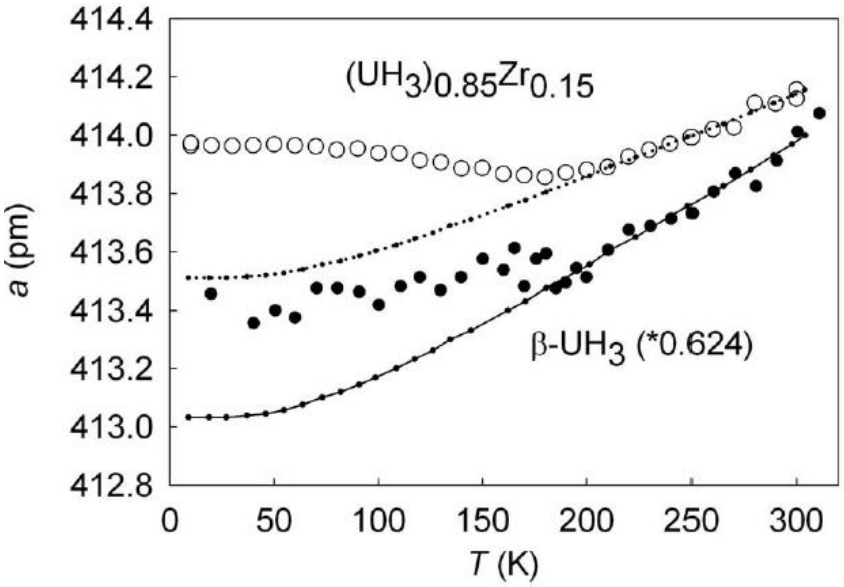

Figure 6.61. Temperature dependence of the lattice parameter of $(UH_3)_{0.85}Zr_{0.15}$ compared with β-UH_3 (data was multiplied on 0.624), with extrapolated dependence from the paramagnetic state.

For determination of spontaneous magnetostriction, the temperature dependence of the lattice parameter *a* was measured in the temperature range 10-300 K using X-ray diffraction. Results are presented in fig. 6.61 together with data published for β-UH_3 [70]. Our data set, which has much lower scatter, reveals the similar expanding tendency below $T \approx 200$ K, and leading to a pronounced invar effect, i.e. compensation of decreasing the lattice volume with decreasing *T* by an expansion due to a magnetic contribution. The latter has to be associated with spontaneous magnetostriction, i.e. the volume expansion due to magnetic ordering. The size of magnetostriction can be estimated after subtraction of the extrapolated regular lattice thermal expansion down to $T = 0$ K, which is followed in the paramagnetic state. Using a Debye type of lattice expansion, used in Ref. 70 (using the same effective Debye temperature 270 K for β-UH_3 and for $(UH_3)_{0.85}Zr_{0.15}$) we obtained the spontaneous volume magnetostriction $\omega_s = 3.2 \cdot 10^{-3}$. This value is even higher than that estimated for β-UH_3, $2.7 \cdot 10^{-3}$ [70], and represents a truly remarkable value among the 5*f* systems. It is interesting to compare the effect with the temperature dependence of magnetization.

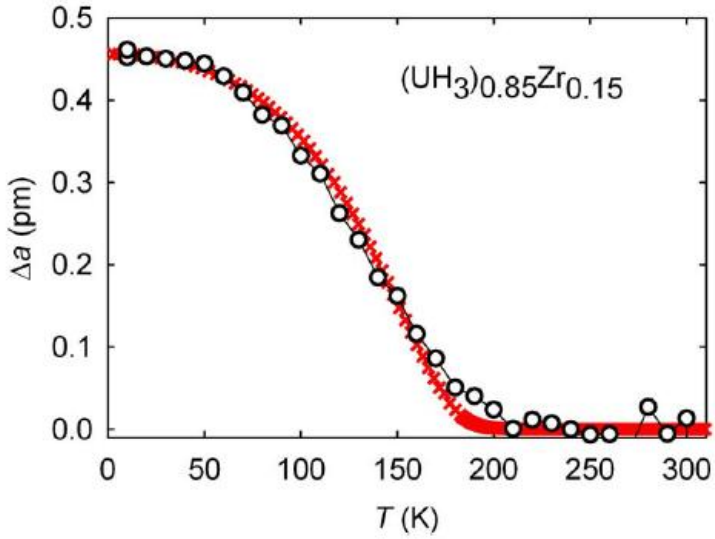

Figure 6.62. Temperature dependence of the lattice parameter *a* with the non-magnetic contribution subtracted (the background in fig. 6.61 (empty circles). The red crosses correspond to M_s^2, both normalized arbitrarily to fit into the figure.

Figure 6.62 displays the magnetic contribution, separated using the tentative background from fig. 6.61. Using the spontaneous magnetization M_s estimated as $M_{4T} - 2 \cdot M_{2T}$, we see that the volume effect follows well M_s^2, as expected for itinerant magnets. On the other hand, it gives a support to the background used. The data allow to determine also the coefficient of thermal expansion of $(UH_3)_{0.85}Zr_{0.15}$, α_v = $21 \cdot 10^{-6}$ K^{-1}.

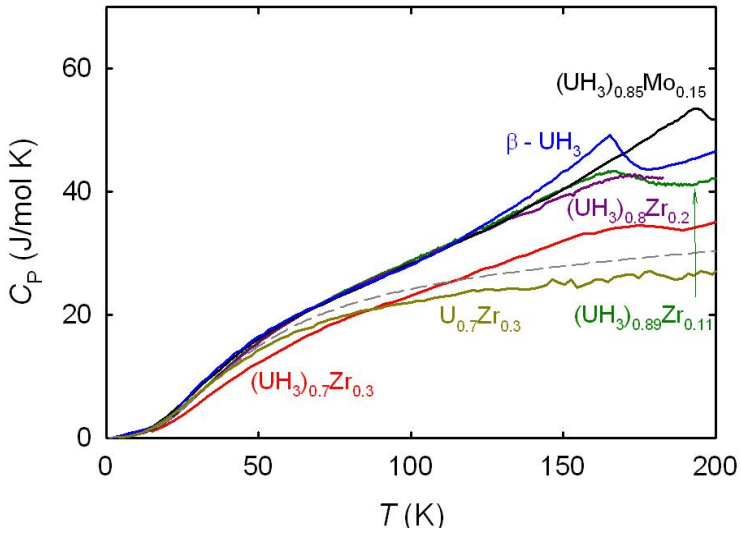

Figure 6.63. Temperature dependence of specific heat of $(UH_3)_{1-x}Zr_x$ hydrides compared with the data on β-UH_3 [71], $(UH_3)_{0.85}Mo_{0.15}$ and $U_{0.7}Zr_{0.3}$. The dashed

curve shows specific heat temperature dependence calculated by the Debye function (θ_D = 190 K) with addition of electronic contribution (γ_e = 32 mJ/mol K^2).

The temperature dependence of specific heat was not studied for all samples over the whole temperature range, which would include both the low-*T* and high-*T* behavior. For Curie temperatures almost 200 K the magnetic part of specific heat is only a small fraction of the lattice part, which together with experimental uncertainties (e.g. due to subtraction of specific heat of Apiezon, mediating the thermal contact) and rather smeared (due to inhomogeneity related to U dilution) anomaly at T_C (see fig. 6.63) brings us to situation, that very little can be concluded about magnetic specific heat itself.

Figure 6.63 shows $C_p(T)$ dependence for $(UH_3)_{1-x}Zr_x$ samples compared with $U_{0.7}Zr_{0.3}$ (U-30 at.% Zr) splat sample and β-UH_3, the last showing a sharp cusp related to T_C. For $(UH_3)_{1-x}Zr_x$ features related to T_C is much broader. The alloy $U_{0.7}Zr_{0.3}$ exhibits a Debye-type saturation in contrast with $(UH_3)_{1-x}Zr_x$ hydrides.

Metal hydrides have typically the lattice specific heat affected by Einstein vibration modes of the H atoms. As a result, a non-Debye character of $C_p(T)$ can be expected. Using values from low-temperature fit (θ_D = 190 K (without consideration of H atoms); γ_e = 32 mJ/mol K^2), we calculate the *T* dependence of specific heat based on the Debye function with addition of electronic contribution, which is shown by the dashed curve in fig. 6.63.

It can be seen that at low temperatures this dependence is in a good agreement with experimental data for hydrides, as well as for initial alloys ($U_{0.85}Zr_{0.15}$), up to ≈ 70 K, where the curve exhibits an inflection. The low-lying phonon modes (acoustic) are similar for the alloys and hydrides. The vibrations related to H atoms are characterized as high energy optical modes, revealed only at higher temperatures. After the optical modes are populated, one can reach the classical limit for specific heat $3R{\cdot}N$ (*N* is the number of atoms in formula unit; *R* is gas constant equal 8.31 J/mol K). The classical limit 24.9 J/mole K for $U_{0.7}Zr_{0.3}$ is practically achieved. The values 77.3 J/mol K for $(UH_3)_{0.7}Zr_{0.3}$ and 99.7 J/mol K for UH_3 will be likely reached only at much higher temperatures. The high energy of the optical modes is the reason why the experimental C_p values are below this limit still at T = 200 K.

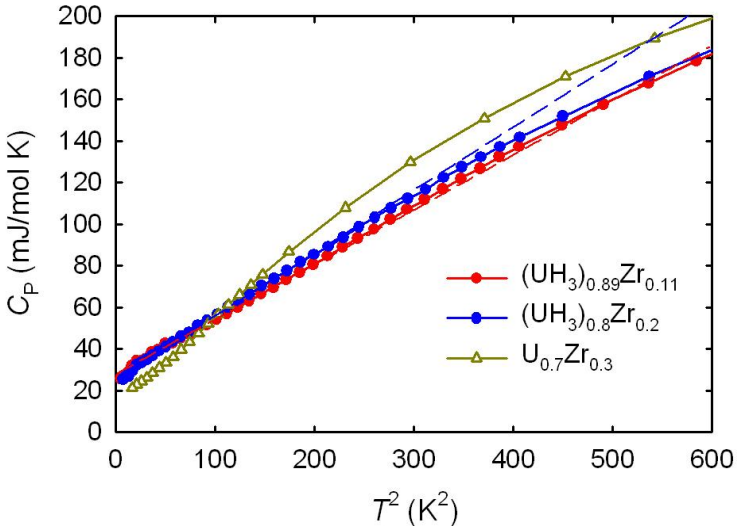

Figure 6.64. Temperature dependence of the specific heat of selected $(UH_3)_{1-x}Zr_x$ hydrides in the C_P/T vs. T^2 representation in comparison with $U_{0.7}Zr_{0.3}$ splat data. The fits were used to determine γ_e and θ_D values.

A linear fit ($C = \gamma T + \beta T^3$) of low temperature part of the temperature dependence of specific heat (C_P/T vs. T^2 representation; fig. 6.64) was used for determination of γ_e and θ_D values. Values of θ_D were determined from fit of low-temperature part of specific heat, where only U and Zr ions were considered without hydrogen. Values of Θ_D are in the range 186-210 K for $(UH_3)_{1-x}Zr_x$, which is lower than that given in Ref. 98 for β-UH_3 (270 K), but very close to the values for $(UH_3)_{1-x}Mo_x$. Ref. 77 gives value for UD_3 338 K including D atoms, which can be recalculated as 213 K without considering of D atoms. In that case our values are in good agreement with Ref. 77. If we include in consideration hydrogen atoms for $(UH_3)_{1-x}Zr_x$ samples, it will gives values of Θ_D in the range 280-310 K.

The γ_e -coefficient of low-temperature specific heat weakly increases with increasing Zr concentration, from 31.4 mJ/mol U K^2 for $(UH_3)_{0.89}Zr_{0.11}$ to approximately 34 mJ/mol U K^2 for $(UH_3)_{0.7}Zr_{0.3.}$ These values are very close to β-UH_3 values given in literature (29 mJ/mol K^2 [98]) and β-UD_3 (33.9 mJ/mol K^2 [77]) and to the values observed for amorphous $(UH_3)_{1-x}Mo_x$ hydrides (mostly β-UH_3 phase. This underlines an important (but not well understood) fact, that α- and β-UH_3 are almost identical not only as to magnetism, but also from the point of view of density of electronic states at the Fermi level.

6.2.3 Discussion of hydrides

As we already seen, the cubic structure of β-UH_3 can accept some doping. Similar examples can be found also in literature. Hydrogenation of U_6Fe yielding U_6FeH_{17} hydride corresponding to $(UH_{\approx 2.8})_{0.86}Fe_{0.14}$ [112]. The resulting Curie temperature 173 K and magnetic moment 0.79 μ_B practically coincides with that of β-UH_3. Similar T_C = 185 K and magnetic moment 1.2 μ_B was reported for U_6CoH_{18} formed in the same β-UH_3 structure [113].

In our case, U-Mo hydrides with amorphous β-UH_3 structure and U-Zr hydrides with α-UH_3 structure have similar ordering temperatures 170-202 K and U moments around 1 μ_B as well as the Sommerfeld coefficient ≈ 30 mJ/mol K^2.

Such situation looks strange, due to a large difference in atomic radii between Fe (1.26 Å) with Co (1.25 Å) and Zr (1.60 Å) with Mo (1.46 Å). That brings up the question about the reason for such uniformity in material properties, while the band 5*f* states in light actinides are very sensitive to all variables.

Some suggestions are provided by the electronic structure calculations presented in Ref. 114 , which indicate that H in a compound with strongly electropositive elements like U behaves electronegatively with increasing of H occupancy. This leads to the depletion of the U-7*s* states, while the U-6*d* states lose about 50% of occupancy. As result, the 5*f* states, remaining below the Fermi energy, have less opportunity to hybridize with non-*f* states. In such situation, the Hill limit of 340 pm, which was empirically determined assuming a number of intermetallics with hybridized 5*f* states, has to be "renormalized" and the critical U-U spacing needed for magnetic ground state must be much smaller.

Hysteresis loops of two types hydrides are apparently different. For $(UH_3)_{1-x}Zr_x$ we observe more rectangular hysteresis loops with higher coercive force than for $(UH_3)_{1-x}Mo_x$. $(UH_3)_{1-x}Mo_x$ exhibit only one large jump in demagnetisation, while $(UH_3)_{1-x}Zr_x$ exhibits many smaller Barkhausen-type jumps. The difference in demagnetisation behaviour at low temperatures could be in crystal structure.

We can only suggest that in crystalline structure of $(UH_3)_{1-x}Zr_x$ magnetic moments are more collinearly arranged, i.e. have higher crystalline anisotropy. As a result, domains have narrow walls and can be easily pinned on grain boundaries and

structure defects. Defects of structure can be caused by randomly distributed Zr atoms. That can also explain the increase of coercive force with Zr concentration.

We can not apply such approach to amorphous structures ($(UH_3)_{1-x}Mo_x$), where magnetic moments are randomly oriented and anisotropy is very small. It takes smaller magnetic fields to demagnetize the whole sample.

Conclusions and future outlook

1. The U-Mo and U-Zr alloys were successfully synthesized in the γ-U phase with a cubic *bcc* A2-type structure using splat-cooling technique. Single phase γ-U samples was obtained already at concentration of Mo ≥ 11 at.%, which is less than obtained earlier by other techniques. For U-Zr samples, pure γ-U was stabilized at concentrations of Zr = 30 at.% Zr. Minimization of dopants is important for determination of low temperature electronic properties of hypothetic "pure" allotropic phases, which do not exist at low temperatures.

2. Low-temperature electronic properties for U-Mo and U-Zr splats stabilized in γ-U were investigated. Magnetic measurements revealed Pauli paramagnetic behavior with susceptibility on the level of $5 \cdot 10^{-9}$ m^3/mol for all U-Mo alloys studied. The magnetic susceptibility is affected besides spin polarization also by orbital polarization and spin-orbit coupling, so the susceptibility value does not have to reflect directly the density of electronic states at the Fermi level.

The temperature dependence of specific heat of the U-Mo and U-Zr splat samples shows a regular behavior with the Sommerfeld coefficient of electronic specific heat γ_e enhanced from 11.0 mJ/mol K^2 for pure U splat (α-U phase) up to γ_e = 16.0 mJ/mol K^2 (i.e. 18.8 mJ/mol U K^2) for U-15at.% Mo and 11.8 mJ/mol K^2 (i.e. 16.9 mJ/mol U K^2) for U-30 at.% Zr, which evidences an increase of the density of states at the Fermi level for γ-U, which can be attributed to enhanced U-U spacing. The decrease of the Debye temperature in the γ-phase indicates the softening of the lattice.

Temperature dependence of electrical resistivity $\rho(T)$ exhibits significant changes in behavior for α-U and γ-U phase samples. Pure-U splat exhibits typical temperature dependence with weakly negative $d^2\rho/dT^2$, which is known for massive U metal, only the residual resistivity is somewhat higher, reflecting the higher disorder. Similar to specific heat, no fingerprints of the CDW transitions could be detected. The residual resistivity ρ_0 is dramatically enhanced for the γ-U phase samples, reaching values 5-10 times higher than for α-U. It can be attributed to scattering on random impurity atoms (dopants). Instead of ρ decreasing with

decreasing T, common in metals, a weak increase ($d\rho/dT < 0$) with saturation in the low-T limit is observed for the γ-U alloys. The mechanism of such behavior can be a weak localization, which appears under conditions of strong disorder, and which is partly suppressed by electron-phonon scattering.

3. U-Mo and U-Zr splats become superconducting at low temperatures. The superconductivity of α-U and γ-U phases is different. Pure U splat (α-U) has a T_c = 1.24 K with critical field 0.3 T and critical slope 0.35 T/K. γ-U alloys have critical temperatures up to 2.1 K, critical field 5-6 T and the critical slope about 4 T/K, i.e. much higher than for α-U. The superconductivity of γ-U can be considered as a bulk effect and can be described by the BCS theory in a weak coupling regime. In contrast with this type of superconductivity it is evident that α-U superconductivity is not a real bulk effect (as evidenced also by the weak anomaly in specific heat, contrasting with the large anomaly corresponding to the BCS prediction in the γ-U phases).

Comparing Mo and Zr doping, Mo is definitely giving more pronounced superconductivity than Zr, as it gives higher T_c values and sharper peaks at specific heat temperature dependence at T_c.

4. U-Mo and U-Zr alloys absorb hydrogen at high pressures ($p \geq 4.5$ bar) and form hydrides with stoichiometry analogous to UH_3. Hydrides are stable and do not ignite on air, which allowed investigation of electronic and magnetic properties.

Structure of the hydrides with Mo is almost amorphous. Very broad XRD peaks can be interpreted as very small (1 nm) grains of the β-UH_3 phase. Samples with Zr forms $(UH_3)_{1-x}Zr_x$ hydrides with crystalline structure, which can be attributed to the mixture of α-UH_3 phase and β-UH_3 phase for low Zr content. For higher Zr concentrations we obtain a single phase α-UH_3 without any β-UH_3 admixture. It should be noticed that α-UH_3 has never been so far stabilized in a pure form, and it was known only from a mixture with a large amount of β-UH_3. Its physical properties remained therefore uncertain.

5. All $(UH_3)_{1-x}Mo_x$ hydrides have ferromagnetic ground state. Despite the amorphization, which usually leads to suppression of magnetism, $(UH_3)_{1-x}Mo_x$ hydrides have noticeably enhanced Curie temperatures, reaching over 200 K for some Mo concentrations, and U magnetic moment $M_s \approx 1.1\ \mu_B$ in comparison with β-UH_3 (175 K; 0.86 μ_B). This is probably the first U-based ferromagnet with such a high Curie temperature.

Hydrides with Zr (α-UH_3 phase) are also ferromagnetic and have $T_C \approx 180$ K which is lower than for hydrides with Mo but close to T_C values of β-UH_3. T_C exhibits a maximum for approx. the same concentration as for Mo alloying. Despite rather different crystal structure and inter-U spacing, the electronic properties of α-UH_3 phase are very similar to β-UH_3.

The coercive field of $(UH_3)_{1-x}Mo_x$ and $(UH_3)_{1-x}Zr_x$ hydrides reaches very high values al low temperatures, and values $\mu_0 H_c \approx$ 4-6 T were found below $T = 3$ K.. Abrupt Barkhausen-type jumps can be observed during the demagnetization process. Such a behavior is associated with pinning of domain walls in highly disordered systems with high anisotropy. The high magnetic anisotropy is related to large orbital moments in bonding 5*f* states.

6. This work should continue by further investigations. Our plan includes investigation of the U-Zr splats microstructure by EBSD. Microstructure of $(UH_3)_{1-x}Mo_x$ and $(UH_3)_{1-x}Zr_x$ hydrides will be investigated by high resolution TEM.

It is also interesting to work on the surface science of splat samples related to kinetics of hydrogenation and oxidation processes.

Transport properties such as Hall Effect and thermal conductivity should be studied for monolithic samples. Magnetization study of hydrides samples at high pressure is also envisaged to indicate how much are the ab-initio calculations, performed for different volumes, relevant.

A great potential for future studies is the tuning of the composition of UH_3-type hydrides in the amorphous phase. In particular, once the amorphous state is guaranteed by the Mo alloying, the material is likely accepting other dopants, too, without the tendency for phase segregation. We tested already that such situation is realized in the double doping by Mo and Zr and by Mo and Fe.

Bibliography

[1] D. Graf, R. Stillwell, T.P. Murphy, J.-H. Park, M. Kano, E.C. Palm, P. Schlottmann, J. Bourg, K.N. Collar, J.C. Cooley, J.C. Lashley, J. Willit, and S.W. Tozer, *Phys. Rev. B* 80 (2009) 2441101(R).

[2] V.P. Sinha, P.V. Hegde, G.J. Prasad, G.K. Dey, H.S. Kamath, *J. Alloys & Comp.* 506 (2010) 253.

[3] A.M. Boring and L.J. Smith in: *Challenges In Plutonium Science*, Necia Grant Cooper (Ed.), Los Alamos Science, No. 26, 2000, pp. 90 – 127.

[4] H.H. Hill, in: *Plutonium 1970 and Other Actinides*, W.N. Miner (Ed.), Nucl. Met., vol. 17, The Metallurgical Society, AIME, New York, 1970, p. 2.

[5] L. Havela, J. Hrebik, J. Sternberk, A. Menovsky, A. Zentko, *Phys. Status Solidi* 59 (1980) k165.

[6] V. Sechovsky, L. Havela, in: *Handbook of Magnetic Materials*, K.H.J. Buschow (Ed.), vol. 11, Elsevier, Amsterdam, 1998, p. 1.

[7] T.P. Orlando, E.J. Mc Niff Jr., S. Foner and M.R. Beasley, *Phys. Rev. B* 19 (1979) 4545.

[8] N.R. Werthamer, E. Helfand, C. Hohenberg, *Phys. Rev.* 147 (1966) 295.

[9] V. Sechovsky, L. Havela, in: *Ferromagnetic materials*, E.P. Wohlfarth and K.H.J. Buschow (Eds.) vol. 4, Elsevier, Amsterdam, 1988, p.309.

[10] H.H. Hill, and B. Matthias, *Phys. Rev.* 168 (1968) 464.

[11] L.E. DeLong, G.W. Crabtree, L.N. Hall, H. Kierstead, H. Aoki, S.K. Dhar, K.A. Gschneidner Jr., A. Junod, *Physica* 135B (1985) 81.

[12] E. Yamamoto, Y. Haga, A. Nakamura, N. Kimura, Y. Inada, H. Sugawara, H. Sato and Y. Onuki, *Physica* B230-232 (1997) 394.

[13] J.W. Chen, R.R. Hake, S.E. Lambert, M.B. Maple, C. Rossel, M.S. Torikachvili and K.N. Yang, *J. Appl. Phys.* 57 (1985) 3090.

[14] J.C. Lashley, B.E. Lang, J. Boerio-Goates, B.F. Woodfield, G.M. Schmiedeshoff, E.C. Gay, C.C. McPheeters, D.J. Thoma, W.L. Hults, J.C. Cooley, R.J. Hanrahan, Jr., and J.L. Smith, *Phys. Rev. B* 63 (2001) 224510.

[15] E. Bucher, J.P. Maita, G.W. Hull, R.C. Fulton, and A.S. Cooper, *Phys. Rev. B* 11 (1975) 440.

[16] M.B. Maple, J.W. Chen, S.E. Lambert, Z. Fisk, J.L. Smith, H.R. Ott, J.S. Brooks and M. J. Naughton, *Phys. Rev. Lett.* 54 (1985) 477.

[17] R.A. Fisher, S. Kim, B.F. Woodfield, N.E. Phillips, L. Taillefer, K. Hasselbach, J. Flouquet, A.L. Giorgi, and J.L. Smith, *Phys. Rev. Lett*. 62 (1989) 332.

[18] Y.G. Naidyuk, O.E. Kvitnitskaya, A.G.M. Jansen, C. Geibel, A.A. Menovsky and P. Wyder, *Fiz. Nizk. Temp.* (*Low Temp. Phys.*) V27, N6 (2001) 668.

[19] D. Aoki, A. Huxley, E. Ressouche, D. Braithwaite, J. Flouquet, J-P. Brison, E. Lhotel, and C. Paulsen, *Nature* 413 (2001) 613.

[20] I.H. Hagmusa, K. Prokeš, Y. Echizen, T. Takabatake, T. Fujita, J.C.P Klaasse, E. Brück, V. Sechovský, F.R. de Boer, *Physica B* 281–282 (2000) 223.

[21] S.S. Saxena, P. Agarwal, K. Ahilan, F.M. Grosche, R.K.W. Haselwimmer, M.J. Steiner, E. Pugh, I.R. Walker, S.R. Julian, P. Monthoux, G.G. Lonzarich, A. Huxley, I. Sheikin, D. Braithwaite and J. Flouquet, *Nature* 406 (2000) 587.

[22] I. Grenthe, J. Drozdzynski, T. Fujino, E.C. Buck, T.E. Albrecht-Schmitt, S.F. Wolf, in: *The Chemistry of the actinide and transactinide elements*, L.R. Morss, N.M. Edelstein and J. Fuger (Eds.), Springer, Dordrecht, 2006, p. 253.

[23] J.C. Lashley, B.E. Lang, J. Boerio-Goates, B.F. Woodfield, G.M. Schmiedeshoff, E.C. Gay, C.C. McPheeters, D.J. Thoma, W.L. Hults, J.C. Cooley, R.J. Hanrahan, Jr., and J.L. Smith, *Phys. Rev. B* 63 (2001) 224510.

[24] L.H. Lander, E.S. Fisher, S.D. Bader, *Advances in Physics* 43 (1994) 1.

[25] P. Chiotti, H.H. Klepfer, R.W. White, *Trans. Amer. Soc. Metals* 51 (1959) 772.

[26] L. Havela, P Javorsky, A.B. Shick, J. Kolorenc, E. Colineau, J. Rebizant, F. Wastin, J.C. Griveau, L. Jolly, G. Texier, F. Delaunay, and N. Baclet, *Phys. Rev. B* 82 (2010) 155140.

[27] E. King and J.A. Lee, *Cryogenics* 3 (1963) 177.

[28] B.S. Chandrasekhar, J.K. Hulm, J. *Phys. Chem. Solids* 7 (1958) 259.

[29] B.S. Chandrasekhar, J.M. Bardeen, *J. Phys. Chem. Solids* 21 (1961) 206.

[30] T.G. Berlincourt, *J. Phys. Chem. Solids* 11 (1959) 12.

[31] Y. Imry, *Introduction to Mesoscopic Physics*, Oxford University Press, Oxford, 2002.

[32] J.H. Mooij, *Phys. Status Solidi* A 17 (1973) 521.

[33] B.B. Goodman, J. Hillairet, J.J. Veyssié, L. Weil, *Proceedings of the VIIth International Conference on Low Temperature Physics*, University of Toronto Press (1961), p. 350.

[34] J.G. Huber, P.H. Ansari, *Physica* 135B (1985) 441.

[35] R.D. Barnard, *Proc. Phys. Soc.* 78 (1961) 722.

[36] G.L. Hofman, M.K. Meyer, A.E. Ray, *Proceedings of International Reduced Enrichment for Research and Test Reactors Conference*, 18-20 October 1998, Sao Paulo, Brazil.

[37] A. Ewh, E. Perez, D.D. Keiser Jr., Y.H. Sohn, *J. Phase Equilibria and Diffusion* 31 (2010) 216.

[38] M.K. Meyer, G.L. Hofman, S.L. Hayes, C.R. Clark, T.C. Wiencek, J.L. Snelgrove, R.V. Strain, K.-H. Kim, *J. Nuclear Mater.* 304 (2002) 221.

[39] J.J. Burke, D.A. Colling, A.E. Gorum, J. Greenspan (Eds.), in: *Physical Metallurgy of Uranium alloys*, Proceedings of the Third Army Materials Technology Conference Book, Hill Publishing Company (1976).

[40] L. Brewer, R.H. Lamoreaux, R. Ferro, R. Marazza, K. Girgis, in: *Atomic Energy Review*, L. Brewer (Ed.), vol. 7, IAEA:Vienna, Special issue (1980) p. 336.

[41] D.T. Hawkins, R. Hultgren, *Constitution of Binary Alloys*, 8th ed., vol. 8, American Society for Metals, Metals Park, Ohio, 1973.

[42] R. Hultgren, P.D. Desai, D.T. Hawkins, M. Gleiser, K.K. Kelley, *Selected Values of the Thermodynamic Properties of Binary Alloys*, American Society for Metals, Metals Park, Ohio, 1973.

[43] C.T. Lee, J.H. Park, T.K. Kim, U.J. Lee, B.S. Lee, and D.S. Sohn, *J. Nucl. Mater.* 373 (2008) 275.

[44] A.A. Bauer, Report No. BMI-1350, Battelle Memorial Institute, UC-25 metallurgy and ceramics, TID-4500, 15th Ed., 1959, p. 1.

[45] A.A. Bauer, S. Kass, and K.M. Goldman, *Proceeding of the Second United Nations International Conference on the Peaceful Uses of Atomic Energy* , vol. 5 (1958) 602.

[46] H.E. Fairman, and A. Kelly in: *ASM Metals Handbook,* ASM International, Ohio, 2004, p. 918.

[47] F.A. Rough, Report No. BMI-1030, *An Evaluation of Data on Uranium-Zirconium Alloys*, Battelle Memorial Institute, 1955.

[48] R.F. Hills, B.R. Butcher and B.W. Howlett, *J. Nucl Mater* 16 (1965) 25.

[49] A.C. Bagchi, G.J. Prasad, K.B. Khan, R.P. Singh, *Transactions of the Indian Institute of Metals* 67 (2014) 123.

[50] R.J. Van Thyne, D.J. McPherson, *Trans. Amer. Soc. Metals* 49 (1957) 598.

[51]T. B. Massalski, H. Okamoto, P. R. Subramanian, L. Kacprzak (Eds.), *Binary Alloy Phase Diagrams–Second edition,* ASM International, Materials Park, Ohio, USA, vol. 3, 1990.

[52] H.L. Yakel in: *Proceedings of the Physical Metallurgy of Uranium Alloys Conference Sponsored by the AEC,* Army Material and Mechanical Research Center, 12-14 February, Vail, Colorado, USA, 1974.

[53] Mme J. Lehmann, R.F. Hills, *J. Nuclear Mater.* 2 (1960) 261.

[54] K. Tangri, G.I. Williams, *J. Nuclear Mater.* 4 (1961) 226.

[55] K.H. Kim, D.B. Lee, C.K. Kim, G.E. Hofman, K.W. Paik, *J. Nucl. Mat.* 245 (1997) 179.

[56] A.V. Vatulin, A.V. Morozov, V.B. Suprun, Yu.I. Petrov, Yu.I. Trifonov, *Met. Sci. Heat Treat.* 46 (2004) 484.

[57] F.B.V. Oliveira, E.F.U. Carvalho, H.G. Riella, Proceedings of 2009 International Nuclear Atlantic Conference (INAC 2009), Rio de Janeiro, RJ, Brazil, September. 27–October, 2009.

[58] E. Dabush, J. Sariel, I. Dahan, G. Kimmel, *JCPDS-Int. Centre Diffraction Data Adv. X-ray Anal.* 45 (2002) 146.

[59] G.I. Terekhov, R.Kh. Tagirova, O.S. Ivanov, *Transformation of gamma-Solid Solutions in U-Nb and U-Zr Alloys* in Fiziko-Khimiya splavov i tugoplavkih soedineniy s toriem i uranom, O. S. Ivanov (Ed.), Moscow: Nauka, 1968, p. 37-41.

[60] Y. Fukai, *The Metal-Hydrogen System*, Springer Series in Materials Science, vol. 21, Springer, Berlin, 1993.

[61] D.G. Westlake, *J. Less-Common Met.* 75 (1980) 177.

[62] D.G. Westlake, *J. Less-Common Met.* 90 (1983) 251.

[63] D.G. Westlake, *J. Less-Common Met.* 91 (1983) 1.

[64] D.P. Shoemaker and C.B. Shoemaker, *J. Less-Common Met.* 68 (1979) 43.

[65] Ch.D. Taylor, T. Lookman, and R.S. Lillard, *Acta materialia* 58 (2010) 1045.

[66] R.N.R. Mulford, F.H. Ellinger, W.H. Zachariasen, *J. Am. Chem. Soc.* 76 (1954) 297–298.

[67] W. Spalthoff, *Z. Phys. Chem., N.F.*, 29 (1961) 258.

[68] A.C. Lawson, J.A. Goldstone, J.G. Huber, A.L. Giorgi, J.W. Conant, A. Severing, B. Cort and R.A. Robinson, *J. Appl. Phys.* 69 (1991) 5112.

[69] A.C. Switendick, *J. Less-Common Met.* 88 (1982) 257.

[70] A.V. Andreev, S.M. Zadvorkin, M.I. Bartashevich, T. Goto, J. Kamarad, Z. Arnold and H. Drulis, *J. Alloys Comp.* 267 (1998) 32.

[71] R. Troc and W. Suski, *J. Alloys Comp.* 219 (1995) 1.

[72] H.E. Flotow, H.R. Lohr, B.M. Abraham and D.W. Osborne, *J. Am. Chem. Soc.* 81 (1959) 3529.

[73] B.M. Abraham, D.W. Osborne, H.E. Flotow and R.B. Marcus, *Z Am. Chem. Soc.* 82 (1960) 1064.

[74] W. Trzebiatowski, A. Sliwa and B. Stalinski, *Roczn. Chem.* 26 (1952) 110.

[75] W.E. Henry, *Phys. Rev.* 109 (1958) 1976.

[76] J.E. Gordon, H. Montgomery, R.J. Noer, S. Pickett, and R. Tobon, *Phys. Rev.* 152 (1966) 432.

[77] J.W. Ward, L.E. Cox, J.L. Smith, G.R. Stewart and J.H. Wood, *J. Phys.* 40 (1979) C4-15.

[78] H.E. Flotow and D.W. Osborne, *Phys. Rev.* 164 (1967) 755.

[79] T. Gouder, R. Eloirdi, F. Wastin, E. Colineau, J. Rebizant, D. Kolberg, and F. Huber, *Phys. Rev. B* 70 (2004) 235108.

[80] T. Gouder, A. Seibert, J. Rebizant, F. Huber and L. Havela, *Mater. Res. Soc. Symp. Proc.* 986 (2007) 17.

[81] L. Havela, K. Miliyanchuk and A. Kolomiets, *Int. J. Mat. Res.* 100 (2009) 1182.

[82] S.C. Parida, S. Dash, Z. Singh, R. Prasad, V. Venugopal, *J. Phys. and Chem. Solids* 62 (2001) 585.

[83] R.F. Hills, B.W. Howlett, B.R. Butcher, *J. Less-Common Metals* 5 (1963) 369.

[84] M.B. Brodsky, N.J. Griffin, M.D. Odie, *J. Appl. Phys.* 8 (1969) 895.

[85] K. Kadowaki and S. B. Woods, *Solid State Commun.* 58 (1986) 507.

[86] N. Toyota, A. Inoue, K. Matsuzaki, T. Fukase, and T. Masumoto, *J. Phys. Soc. Japan* 53 (1984) 924.

[87] A. Slebarski, J. Goraus, J. Deniszczyk, L. Skoczen, *J. Phys.: Condens. Matter* 18 (2006) 10319.

[88] P.W. Anderson, K.A. Muttalib, T.V. Ramakrishnan, *Phys. Rev. B* 28 (1983) 117.

[89] T.P. Orlando, E.J. McNiff Jr., S. Foner, M.R. Beasley, *Phys. Rev. B* 19 (1979) 4545.

[90] J.C. Lashley, A. Lawson, R.J. McQueeney, G.H. Lander, *Phys. Rev. B* 72 (2005) 054416.

[91] L.E. DeLong, J.G. Huber, K.N. Yang, M.B. Maple, *Phys. Rev. Lett.* 51 (1983) 312.

[92] D.J. Lam, D.O. Van Osterburg, D.W. Pracht, *J. Appl. Phys.* 35 (1964) 976.

[93] N. Baclet, M. Dormeval, L. Havela, J.M. Fournier, C. Valot, F. Wastin, T. Gouder, E. Colineau, C.T. Walker, S. Bremier, C. Apostolidis, G.H. Lander, *Phys. Rev. B* 75 (2007) 035101.

[94] D. Rafaja, V. Klemm, G. Schreiber, M. Knapp and R. Kuzel, *J. Appl. Cryst.* 37 (2004) 613.

[95] R.M. Leal Neto, C.J. Rocha, E. Urano de Carvalho, H.G. Riella, M. Durazzo, *Journal of Nuclear Materials* 445 (2014) 218.

[96] E.E. Pasqualini, J.H. Garcia, M. Lopez, E. Cabanillas, P. Adelfang, *6th International Topical Meeting on Research Reactor Fuel Management (RRFM 2002)*, European Nuclear Society, Ghent, Belgium, April 21-25, 2002, p. 183-187.

[97] L. Havela, K. Miliyanchuk, D. Rafaja, T. Gouder, and F. Wastin, J. Alloys Comp. 408–412 (2006) 1320.

[98] J.C. Fernandes, M.A. Continentino and A.P. Guimaraes, *Solid State Communications* 55 (1985) 1011.

[99] P.H. Frings, J.J.M. Franse and P.E. Brommer, *J. Phys. C: Solid State* 18 (1985) 1955.

[100] H. Oesterreicher, F.T. Parker and M. Misroch, *J. Magn. Magn. Mater.* 15-18 (1980) 1485.

[101] S. Mašková, A.M. Adamska, L. Havela, N.-T.H. Kim-Ngan, J. Przewoźnik, S. Daniš, K. Kothapalli, A.V. Kolomiets, S. Heathman, H. Nakotte and H. Bordallo, *J. Alloys Comp.* 522 (2012) 130.

[102] T. Egami, *Phys.Stat.Sol. A* 19 (1973) 747.

[103] T. Egami, *Phys.Stat.Sol. A* 20 (1973)157.

[104] I.Y. Glagolenko, K.P. Carney, S. Kern, E.A. Goremychkin, T.J. Udovic, J.R.D. Copley, and J.C. Cook, *Appl. Phys. A* 74 (Suppl.) (2002) S1397.

[105] F. von Zeppelin, M. Hirscher, H. Stanzick and J. Banhart, *Composites Science and Technology* 63 16 (2003) 2293.

[106] P. Javorský, L. Havela, F. Wastin, P. Boulet, J. Rebizant, *Phys.Rev. B* 69 (2004) 054412.

[107] H. Oesterreicher, F.T. Parker, M. Misroch, *Phys. Rev. B* 18 (1978) 480.

[108] L. Havela, V. Sechovský, F.R. de Boer, E. Brück and H. Nakotte, *Physica B* 177 (1992) 159.

[109] M.S. Henriques, D.I. Gorbunov, J.C. Waerenborgh, L. Havela, A.B. Shick, M. Diviš, A.V. Andreev, A P Gonçalves, *J. Phys.: Condens. Matter* 25 (2013) 066010.

[110] P. Santini, S. Carretta, G. Amoretti, R. Caciuffo, N. Magnani, and G.H. Lander, *Rev. Mod. Phys.* 81 (2009) 807.

[111] H. Ohldag, T.J. Regan, J. Stöhr, A. Scholl, F. Nolting, J. Lüning, C. Stamm, S. Anders and R.L. White, *Phys. Rev. Lett.* 87 (2001) 7201.

[112] H. Drulis, F.G. Vagizov, M. Drulis, and T. Mydlarz, *Phys. Rev. B* 52 (1995) 9500.

[113] A.V. Andreev, M.I. Bartashevich, A.V. Deryagin, L. Havela and V. Sechovsky, *Phys. Stat. Sol. A* 98 (1986) K47.

[114] I. Tkach, M. Paukov, D. Drozdenko, M. Cieslar, B. Vondráčková, Z. Matěj, A.V. Andreev , I. Turek, M. Diviš and L. Havela, *Phys.Rev. B* 91 (2015) 115116.